Bioinspired Hydrogel Formulations for Bone Regeneration- Fabrication, Characterization, and *In Vivo* Efficacy Evaluation in Mice and Rabbits

by

Akhil Patel

Bachelor of Pharmacy, Gujarat Technological University, 2012.

M.S. in Pharmaceutical Sciences, University of Pittsburgh, 2015.

Submitted to the Graduate Faculty of

School of Pharmacy in partial fulfillment

of the requirements for the degree of

Doctor of Philosophy

University of Pittsburgh

2019

UNIVERSITY OF PITTSBURGH

School of Pharmacy

This dissertation was presented

by

Akhil Patel

It was defended on October 17th, 2019

And approved by

Lisa Rohan, Ph.D., Professor

Department of Pharmaceutical Sciences, School of Pharmacy, University of Pittsburgh

Song Li, M.D., Ph.D., Professor

Center for Pharamcogenetics, Department of Pharmaceutical Sciences,

School of Pharmacy, University of Pittsburgh

Elia Beniash, Ph.D., Professor,

Center for Craniofacial Regeneration, Department of Oral Biology,

School of Dental Medicine, University of Pittsburgh

Adam Feinberg, Ph.D., Professor,

Department of Materials Science & Engineering and Biomedical Engineering,

Carnegie Mellon University.

Dissertation Advisor: **Shilpa Sant**, Ph.D., Associate Professor,

Department of Pharmaceutical Sciences, School of Pharmacy,

Department of Bioengineering, McGowan Institute of Regenerative Medicine, UPMC

Hillman Cancer Research Center, University of Pittsburgh.

Bioinspired Hydrogel Formulations for Bone Regeneration- Fabrication, Characterization, and *In Vivo* Efficacy Evaluation in Mice and Rabbits

Akhil Patel, MS

Constant increase in aging population, bone diseases incidence, and traumatic/ accidental injuries have led to millions of orthopedic surgeries worldwide. In the USA, 280K hip, 700K vertebral, and 250K wrist fractures are treated every year. Most clinical interventions, like autografts and allografts, face challenges of rejection, significant clinical morbidity, prolonged hospitalization, delayed rehabilitation, and surgical complications. Relatively new approaches employ growth factors such as bone morphogenetic proteins (BMPs) to exert potent bone regenerative activity; however, they are limited due to serious side effects such as uncontrolled bone growth, prohibitive costs, and stability issues in the clinical setting.

In the process of natural bone development, collagen acts as an organic template to guide mineral deposition in the bone extracellular matrix (ECM) and apatite minerals act as inorganic phase, both of which interact at molecular level forming hierarchical nanocomposites. However, most of the currently explored materials are just physical blends of organic and inorganic phases. Therefore, these materials show limited potential to recapitulate bioactivity to regenerate bone without added growth factors.

This dissertation focuses on our progress towards the development of bioinspired hydrogel scaffolds using self-assembly of oppositely charged polysaccharides to regenerate critical-sized bone defects without the use of growth factors. We summarized the results from our preclinical studies to assess its efficacy using mice and rabbits.

First, we optimized process parameters such as concentration and temperature to facilitate interfacial polyionic complexation (IPC) between cationic (chitosan (CHT)) and one of the three

anionic polysaccharides, namely, gellan gum (GG), alginate (ALG), and kappa-carrageenan (KCA). This resulted in three variants of hydrogel scaffolds: CHT-GG, CHT-ALG, and CHT-KCA. We characterized these three variants of hydrogel scaffolds for their collagen-mimetic multi-scale hierarchy. We further demonstrated the versatility of hydrogel scaffolds to load small molecule or metal nanoparticles. Further, we developed automated method to produce, collect and orient IPC fibers to make into a bilayer scaffold.

We then assessed ability of hydrogel scaffolds to sequester bone-like minerals from simulated body fluid *in vitro.* All three variants of hydrogel scaffolds promoted biomimetic mineralization *in vitro* both on the surface and inside the scaffolds.

We further assessed the efficacy of all three variants of hydrogel scaffolds, processed as films, in non-load bearing, critical-sized (5 mm diameter) mouse calvaria defects. Non-mineralized CHT-KCA showed significantly higher calvaria regeneration and defect closure compared to the empty defect control group; however, the defect was still far from closure. More interestingly, implantation of *in vitro* mineralized CHT-KCA further enhanced bone regeneration significantly compared to the empty defect. Additionally, preservation of minerals by lyophilization of the mineralized scaffold condition prior to implantation significantly increased bone regeneration as compared to (hydrated) mineralized CHT-KCA.

We further tested efficacy of CHT-KCA in semi-load bearing ulna defect. Here, we first processed hydrogel scaffolds as 1.5 cm long cylindrical scaffolds, which were implanted in a critical-sized rabbit ulna defect. Cylindrical hydrogel scaffolds showed an onset of bone regeneration as early as 4 weeks. Moreover, mineralized CHT-KCA significantly enhanced bone regeneration and improved functional mechanical properties of the regenerated bone compared to

empty defect after 12 weeks. Histological assessment revealed complete bone healing of the mineralized CHT-KCA through endochondral ossification.

Collectively, these studies suggest that hydrogel scaffolds can be considered as a versatile platform technology and they can be processed in any shape and sizes; pre-fabricated in the lyophilized, hydrated or even injectable form. Hydrogel scaffolds can conform to and maintain the shape of the defect. Hydrogel scaffolds demonstrated great potential to regenerate bone in mice calvaria defect and rabbit ulna defect.

TABLE OF CONTENTS

-------------------------------------Intentionally left blank---

LIST OF FIGURES

ACKNOWLEDGEMENTS

I would like to thank University of Pittsburgh, School of Pharmacy, for giving me the opportunity to study here. I have developed a sense of belongingness with the SOP family and I am looking forward to staying connected.

I sincerely thank my advisor Dr. Shilpa Sant for constantly motivating me to bring the best out of me and trusting me with the most challenging studies in the lab. I have learnt so much working with Shilpa. Her 'never give up' attitude for science is inspirational for me. I constantly thrive to instill this attitude in me to achieve my goals. Your teachings will remain with me for my lifetime. I am very proud to get my PhD training with you. I could not have asked for a better mentor who can wear all different hats as necessary for my growth, be it supporting me in my down time or challenging me in my comfort time. I would also like to thank Dr. Vinayak Sant for always welcoming me with my roadblocks and advising me with best solutions. His vast practical experience has rescued me several times when I was hopelessly stuck with scientific problems. I have enjoyed Vinayak's company outside the lab at adventure sports and fun activities. I admire his simplicity and sense of humor.

I would like to express my gratitude to my committee members, Dr. Song Li, Dr. Lisa Rohan, Dr. Elia Beniash, and Dr. Adam Feinberg. You all have nurtured my research acumen and motivated me to a seasoned scientist. I will always look up to you as my role models. Thank you for providing your domain expertise and anytime access to all of your scientific instruments in the lab.

I would like to thank my current and past colleagues without whom this journey would not be possible. I have enjoyed working with Dr. Yingfei Xue as an elder brother and

compassionate colleague. You have always set a great benchmark in the lab motivating other graduate students including me to follow it. Your guidance during my comprehensive exam or exams during the coursework made my life so much easier. I admire your objectiveness and laser-sharp focus. I would also like to thank Dr. Manjulata Singh for providing warmth of an elder sister to many including myself in the lab. Your meticulous scientific skills and ability to work with large-scale experiments have always inspired me to push my limits. I would also like to thank Dr. Catalina Ardia, I have only worked with you for my recent six months, but I have learnt a lot from you. I am so lucky to have colleagues like you in the lab during my training. I enjoyed working with Aishwarya Vasudevan, Shilpaa Mukundan, Jean Liu, Yuzhe Chen, Rebecca Hartley, Harini Venkatakrishnan, Tatyana Yatsanko, Vibishan Balasubramanian, Sricharani Balmuri, Piyusha Sane, Supraja Ranganathan, Vishal Rakshe, Jack Gong, Urmi Chheda, Yohann Pitale, Prithvirajan durairajan, Mrunal Sakharkar, Sandhya Venkatakrishnan, Dr. Kishor Sarkar, Vishi Agrawal, Jamir Wilson, Janet Canady, Nithya Narayanan, Kendra, and Mayuri Dutta.

I would like to greatly appreciate the immense support from Dr. Maggie Folan, Dr. Sam Poloyac, Dr. Smith, and Dean Koborth.

I would like to thank our collaborator, Dr. Samer Zaky, Dr. Charles Sfeir, Dr. Alejandro Almarza, Dr. Hongshuai Li, Karen Schoedel, Dr. Sachin Velankar, Dr. Donna Stolz, Dr. Alan Watson, Mr. Jonathan Frank, Dr. Marra Sullivan, and Dr. Simon Watkins. I am very thankful to Center for Craniofacial Regeneration for accommodating me as one of their own students and patiently answering me for my urgent micro-CT data analysis requests. I owe my utmost gratitude to Dr. Samer Zaky who mentored me for all the surgeries and taught me every tiny detail patiently despite his busy schedule. Major part of my rodent studies would not be possible without you. I

have enjoyed working alongside you and am so proud to learn some of the most advanced orthopedic scientific skills from you.

I would also like to thank Dr. Cecilia Yates for providing guidance throughout my PhD training.

A major part of my dissertation is comprised of electron microscopy which was done at Center for Biological Imaging. I would like to express my gratitude to Dr. Donna Stolz and her lab members, especially, Mr. Jonathan Frank and Dr. Marra Sullivan.

I sincerely thank Dr. Robert Gibbs for access to confocal microscope. I would like to thank Lori Altenbaugh for all the administrative help throughout my studies.

My sincere thanks to all the faculty, staff and fellow graduate students from the School of Pharmacy. I have made countless memories during my time here with you.

This dissertation is dedicated to my mom, Ms. Chandrikaben Patel; my dad, Dr. Pravinchandra Patel; my grandparents, Mr. Hemchanddas Patel and Ms. Pushpaben Patel; my brother Jignesh and late uncle Mr. Chandrakant Patel as well as countless other extended family members for their constant encouragement and for teaching me values and the art of living. I am the reflection of your teachings from the day I arrived in this world.

I am thankful to my funding from Department of Pharmaceutical Sciences for my Graduate Student Fellowship. Mouse and rabbit studies presented in this dissertation were possible due to pilot funding from Center for Medical Innovation, Swanson School of Engineering, University of Pittsburgh.

I would also like to thank Kelly Hoffman, Senior Veterinary Technician and Division of Laboratory Animal Resources for their service with rabbit housing and surgeries. Authors also

thank Antony Green and Paul Knizner for their service for histology. Last but not the least, I would like to thank the mice and rabbits who sacrificed their lives for the advancement of science.

1 INTRODUCTION

1.1 BONE LOSS CLINICAL MANAGEMENT

Trauma due to sports injuries and road accidents lead to loss of bone beyond body capacity to heal. Bone also is lost to cancer. Bone cancer in children accounts for 5% of all cancers in children according to the center for disease control and prevention (CDC). After blood, bone tissues are the second most commonly transplanted material[1]. Moreover, osteoporosis leads to frequent bone fractures amounting to more than 8.9 million fractures per year.[2] Out of the total bone fractures, 5-10% fail to heal due to delayed union or non-union.[3] Additionally, hip and knee replacements are also on the rise costing $25 billion in the USA alone.[4] Similarly, spinal degeneration, deformity, trauma or infection leads to removal of the damaged bone, intervertebral disk or vertebral lamina are the most common ones.[5] Removal of such structures which are critical to mechanical stability of human skeleton require immediate surgical intervention.

Current standard clinical treatment or management of bone loss is determined depending on the site of bone loss. For example, strategies for craniofacial bone loss are different than spinal fusion or long bone defects. However, all the all of these strategies are focused on a common aim to replace the lost bone with either regenerated bone or a replacement implant which functions same as native bone. Bone grafting, from the same patient (autograft) or from a suitable cadaveric donor (allografts), have also been used to correct the bone loss due to cancer or trauma, the cost of which is reported to be 2.5 billion annually with more than 600,000 cases.[6] Although used widely and often referred as gold standard,[7] autografts are not without shortcomings. Autografts require long surgery as the patient needs to be operated at two sites: the healthy tissue (mostly iliac crest

or pelvis) for harvesting the injury area and the implantation area. This increases complications in 8-10% of the patients for donor site infections or morbidity. [8, 9]. Despite complications, autograft and allografts were used 92% of the total bone grafts.[10]

Synthetic bone grafts are clinically approved and are employed with the primary purpose of providing mechanical support to the damaged bone tissue. The majority of synthetic grafts are bio-inert with some of ceramics materials being bioactive or bio-absorbable which can integrate with healing bone[11]. Until 2000, most of the synthetic bone graft procedures were limited to the use of metal implants or fixation systems such as screws, plates, or rods.[12] Metal implants are used in cases where mechanical support is needed, for example long bones of femur or tibia or vertebral fractures. Additionally, the decision of whether a non-degradable or degradable implant should be used is dependent on the its intended use to meet specific clinical success criteria. For example, fracture fixation plates and screws in lower proximity long bones are fixed using bolts which are often not required to integrate with the native bone and therefore, require removal surgeries. Whereas hip or joint replacement screws as well as rods used in spinal fusion surgeries are needed to integrate with the surrounding bone and therefore resorbable implants are mostly used.[13] Metal implants often lead to fibrotic tissue formation due to delayed bone healing in the area.[14-16] Surface treatment and surface coating of the metal grafts or use of degradable polymeric screws and plates are used as strategies to achieve ideal function which is reviewed in detail by Agarwal and Garcia.[17] In the last decade, metal fixation approaches got a makeover to include osteoinductive materials with them which could promote bone healing, especially in the case of spinal interventions such as spinal fracture or fusion.[18] Duarte *et al.* depicted temporal progression of the biomaterials used in spinal fusion which is reprinted in **Figure 1**.[19]

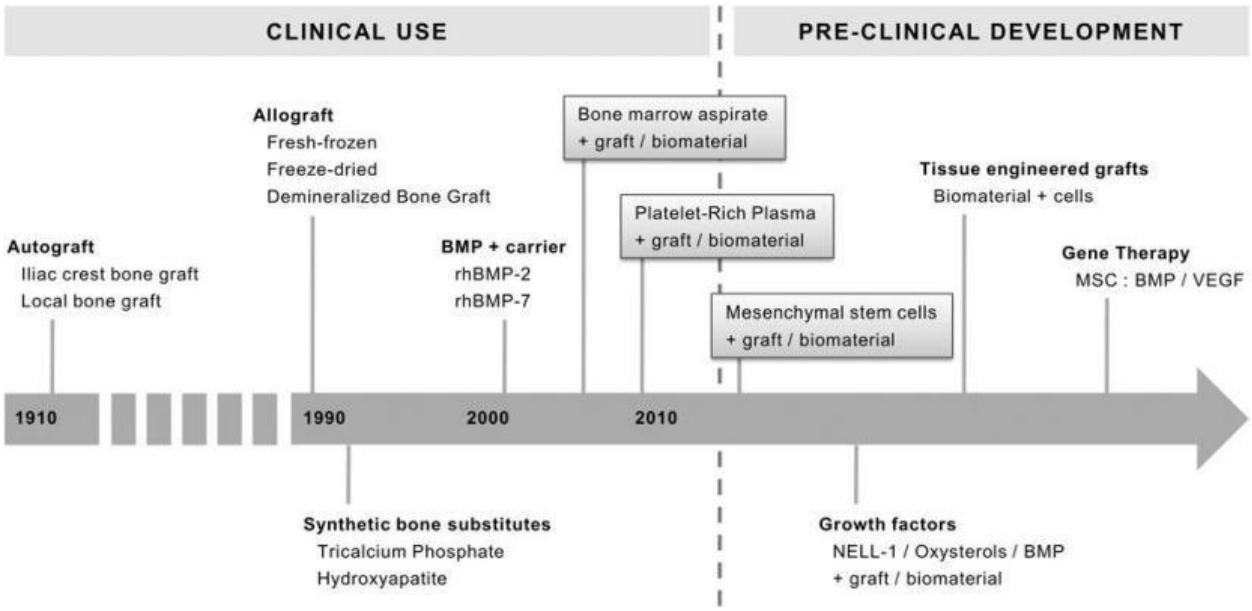

Figure 1: Temporal progression of biomaterials and bioactive agents used for spinal fusion. [19]

(Reprinted with permission)

1.2 SUBSTITUTE BONE GRAFTS

Substitute bone graft of various forms, such as solids in custom shapes and injectable semi-solids are gaining interest especially due to their potent osteogenic activity which removes the need of two surgery sites in case of autografts. Substitute bone grafts can be classified into three major classes based on the source of osteogenecity. 1) defined growth factors-based bone grafts, 2) undefined growth factor mix-based bone grafts, and 3) Inorganic-organic biomaterial composite bone grafts. These categories are discussed in detail below.

1.2.1 Defined growth factor-based bone grafts

Bone healing and remodeling are regulated by hormones and locally released growth factors which are released by cells at the injury site. Major growth factors released in the bone injury area include Bone morphogenic proteins (BMPs), vascular endothelial growth factor (VEGF), transforming growth factor- β (TGF-β), platelet-derived growth factor (PDGF), fibroblast growth factor (FGF), and insulin-like growth factor (IGF). [20]

BMPs were first discovered by Marshall Urist in 1965. BMPs have been proven as potent inducer of bone regeneration in numerous *in vitro* and *in vivo* studies. BMPs were first approved by the food and drug administration (FDA) in 2001 as recombinant human BMP7 (rhBMP7) for long bone nonunion. It was in 2002 when rhBMP2 was approved for spinal fusion application after which the orthopedic field dedicated enormous efforts to improve the combination products with rhBMP2 and its carrier. For example, one of the most popular bone graft substitute products-INFUSE (Medtronic Inc.) comprises of collagen sponge and a vial of rhBMP2, ready to reconstitute. This collagen-rhBMP2 gel is added to a metal fixture and implanted for spinal fusion. Due to its unparallel efficacy and still relatively less FDA approvals of alternative appraohces, BMPs have been used for off-label indications by orthopedic surgeons.[21, 22] This has increased reports of adverse effects such as continuation of bone remodeling even after the desired bone growth is achieved and could eventually result in uncontrolled bone growth. Since BMPs are highly soluble, if used alone without any carrier material, they disperse instantly after implantation, thereby, either increasing the risk of side effect or failing to induce bone growth due to its degradation by proteases within minutes.[23, 24] In order to overcome these side effects, many preclinical studies have reported novel carrier materials. HA has shown great affinity for BMP2 whereas inclusion of β-tricalcium phosphate (β-TCP) has shown to prevent the compression of

collagen sponge, thereby preventing a burst release of BMP2 from the collagen sponge. Moreover, many successful attempts are reported to engineer controlled release of BMP2. For example, Han *et al.* designed a collagen scaffold material with rhBMP2 so as to make the release of BMP2 dependent on the degradation of collagen scaffold in rats.[25]

High cost of BMP2 is another driver for innovation. Most current BMP2 products approved for clinical use produce BMP2 from transfected mammalian cells. Some recent studies have demonstrated a cheaper alternative to produce rhBMP from *Escherichia coli* which showed similar efficacy to rhBMP produced in mammalian cells. Moreover, other growth factors like VEGF is not only known for angiogenesis but also in ossification and bone turnover and have been tested *in vivo* using novel delivery methods.[26, 27]

Additionally, it should be noted that, rhBMP2 (INFUSE) and rhBMP7 (OP-1) are contraindicated to be used at the site of a resected tumor, patients with the history of malignancy or an ongoing malignancy. Therefore, alternative approaches to growth factor-based approaches are particularly highly demanded at least for the growth factor contraindicated patients.

1.2.2 Undefined growth factor mix-based bone grafts

Undefined mix of growth factors derived from autogenic or allogenic origin have inherent advantage of multiple growth factors in tolerable doses as they are produced indigenously.

1.2.2.1 Platelet derived plasma

Platelet concentrates such as platelet-rich plasma (PRP) is mostly derived from the same patient therefore, it avoids issues of immunogenesis and disease transmission.[28, 29] PRP is defined as a small volume of plasma obtained by centrifugation of blood and has a platelet

concentration above the baseline level of patient's whole blood. Platelets aid in cell proliferation, differentiation, chemotaxis, angiogenesis, which are important functions during early bone healing.[29, 30] Marx *et al.* first introduced the osteogenic effects of PRP to enhance bone mineral density and promote bone regeneration in combination with autologous mandibular bone grafts.[31] Research in this area has progressed to optimized platelet count. The baseline platelet count in whole blood is found to be in the range of 150000 to 350000 μL with 200000 as average. Three to five-fold greater platelet count than the baseline platelet count is considered as common benchmark for the PRP therapy.[32]

Despite its great autologous potential, activation of platelets leading to coagulation before application is a largely acknowledged challenge. Such activation could be triggered by either endogenous factors in the blood present at the injury site or exogenous factors such as type I collagen, calcium chloride, or thrombin. Many anticoagulants such as heparin, citrate, and ethylene di-amine tetra-acetic acid (EDTA) are used as anticoagulants for PRP therapy. Efforts are underway to find optimum formulations and partner compounds that can prevent its early coagulation.

1.2.2.2 Demineralized bone matrix

Demineralized bone matrix (DBM), also known as bone putty graft, is obtained by extracting away the mineral phase from particulate human cadaveric bone using dilute hydrochloric acid. This leaves organic constituents including growth factors and collagen type I which are lyophilized and packaged for commercial use. DBM possesses both osteoconductive and osteoinductive properties. DBM releases BMPs at the implant site which attracts and recruits mesenchymal stem cells and osteoblasts.[33, 34] Most DBM products also add additional

excipients to particulate cadaveric bone to attain paste or putty formulation to make it surgeon-friendly as it can be easily molded to the injury site.

Clinical reports on the use of DBM for spinal fusion indicate similar efficacy of DBM and gold standard autologous grafts. Clinical outcomes of DBM are reviewed in depth.[33, 35, 36] It should be noted that all three reviews highlighted the need for additional mechanistic studies to precisely define target indication and the category of patient population that would benefit the most from DBM.

1.2.3 Inorganic-organic biomaterial composite bone grafts

The need for better bone graft alternatives with safer and predictable biological activity led to clinical approval of various bone substitutes such as ceramics and polymer-based hydroxyapatite (HA), β-TCP. They were found to enhance bone healing due to their osteoconductive properties incorporated by similarity in chemical composition with the bone tissue.[37]

In the scope of this dissertation, we have focused on natural polymer-based composites which include collagen, gelatin, polysaccharides, and bacteria-sourced composites. Synthetic composites have not become as popular due to cost and biocompatibility issues.[38] On the other hand, natural polymers are biocompatible and express inherent cell recognition property which enhances cell attachment and differentiation.[39]

1.2.3.1 Collagen-based composite grafts

Collagen type-I and calcium phosphate mineral composite resemble the composition of bone matrix and therefore, these grafts have dominated bone graft market. Collagen provides chemical and physical flexibility. For example, it can be chemically modified to introduce more

cross-links or grafting biological molecules in its structure to achieve tissue-specific requirements.[40, 41] Similarly, it has been advantageous to be formulated and used in bone tissue engineering in multiple physical forms such as powder/particles,[42] gel/solution,[43, 44] films/membranes,[45, 46] fibers/sponges.[47-49] Moreover, it can readily form blends and composites with other materials or minerals. These are either injected or implanted locally at the bone injury site. Most collagen-HA composites are fabricated using *in situ* precipitation techniques[50] Such scaffolds show multi-scale porosity (50-100μm and 1-5 μm) due to multi-scale freezing which significantly improves the mechanical properties of pure collagen scaffolds.

Collagen composite gels are considered most friendly for cells due to high water content. Huang *et al.* reported such collagen-chitosan-HA gel which formed stable gel at body temperature resembling porous microstructure of natural bone ECM. However, the gel only showed osteoinductivity when it was used along with rhBMP2. Similarly, Sotome *et al* reported calcium ion-based crosslinking HA-collagen-alginate-rhBMP2 gel which showed bone regeneration within 5 weeks with evidence of gel deformation and bone ingrowth into the material.[51]

Collagen membranes or films are used in guided tissue regeneration and wound healing in dental applications because of excellent resorbability in oral cavity, thereby avoiding the need for a follow-up surgery.[52] There are limited studies testing collagen-mineral composite membranes for bone regeneration. In a preliminary study, Lee *et al.* compared collagen-silica membrane with collagen membranes in 5 mm calvarial defect in albino rats and reported osteoblast differentiation in three weeks.[53] Commercially available Bio-Gide® is an example collagen membrane composed of a compact layer and a porous layer and widely used for dental procedure which degrades within 21 days by macrophages.[54]

Porous collagen sponges provide 3D architecture opening opportunities for bioactive composite formation. For example, a Bioglass® particle-collagen composite showed osteoconductive properties *in vitro,* although particles and collagen sponge did not show osteoconductive properties separately.[55] The synergistic effect was attributed to bioactive silicic acid layer formation on collagen which could bind to calcium and cell proteins. In a more successful strategy, HA-collagen microcomposite were prepared using freeze-dry method which showed complete bone bridging in critical sized mouse calvarial defect.[56]

Despite its excellent biocompatible and biosorption properties, use of collagen is limited due to poor mechanical properties, welling, water solubility, immunogenicity, processing difficulties such as easy denaturation, and potential to transmit pathogens due to its bovine or porcine source.[38, 57]

Collagraft™ (Collagen corp. USA) is one such graft approved by FDA in 1993 which is composed of bovine collagen mixed with patient bone marrow, HA, and β–TCP. [54]

1.2.3.2 Gelatin-based composite bone grafts

Gelatin can be considered as upgraded version of collagen as it is obtained by partial hydrolysis of collagen. It comprises of water-soluble proteins and alleviates cost issues and immunogenicity as well as pathogen transmission issues due to its denaturation. Gelatin/nano-HA composites are made with electrospraying to achieve porous structure similar to bone-ECM.[58] However, they often show poor mechanical properties. To enhance mechanical properties, gellan gum [59] or polycaprolactone (PCL) [60] are combined prior to electrospinning to increase elasticity or ultimate strength. However, typical electrospinning apparatus forms 2D fibrous structures resulting in a film instead of 3D architecture similar to bone-ECM. Therefore, Liu *et al.*

designed a 3D nanofiber-gelatin-apatite composite scaffolds using thermally induced phase separation and porogen leaching and compared it with commercially available Gelfoam® (Pfizer Inc.) and found that their composite showed superior biocompatible and mechanically stability.[61] In addition to implantable gelatin-based composites, injectable gelatin microsphere gelatin-apatite composites have also been tested as delivery vehicle for growth factors.[62]

1.2.3.3 Other natural polymer composite bone grafts

Bacteria-derived polymers such as polyhydroxyalkalnoates (PHA, derived from gram-positive and gram-negative bacteria) are highly biocompatible and bioactive. Poly (3-hydroxybutyric acid) (P3HB) which is a member of the PHA polymer class, promotes bone regeneration due to its piezoelectric properties.[63, 64] Moreover, its degradation produces 3-hydroxybutyric acid which increases calcium influx in the cell preventing its apoptosis. Although *in vivo* studies testing the efficacy of HA-PHA composites are limited, *in vitro* studies showed considerable differentiation and higher ALP activity in HA-PHA composites compared to PHA.[65, 66]

Silk fibroin and bacterial cellulose are known for their tensile strength. Therefore, their composites with HA provides the strongest tensile strength stability among all the natural polymers explored for bone tissue engineering applications. Both silk fibroin and bacterial cellulose readily promotes nucleation of biomimetic apatite on the surface,[67, 68] however, their *in vivo* osteogenic potential is largely unknown.

1.2.3.4 Polysaccharide-based composite bone grafts

Polysaccharides control mineral deposition in marine creatures and crustaceous animals. Chitosan,[69, 70] alginate, [71] gellan gum, [72, 73] carrageenan[74], glycosaminoglycans

(GAGs), heparan sulfate, etc. either alone or in combination with other polysaccharides and calcium phosphate minerals have shown mineralization potential for regeneration with or without added growth factors. The bioactivity of polysaccharides make them an excellent class of natural polymers to provide an organic template for mineral deposition[75].

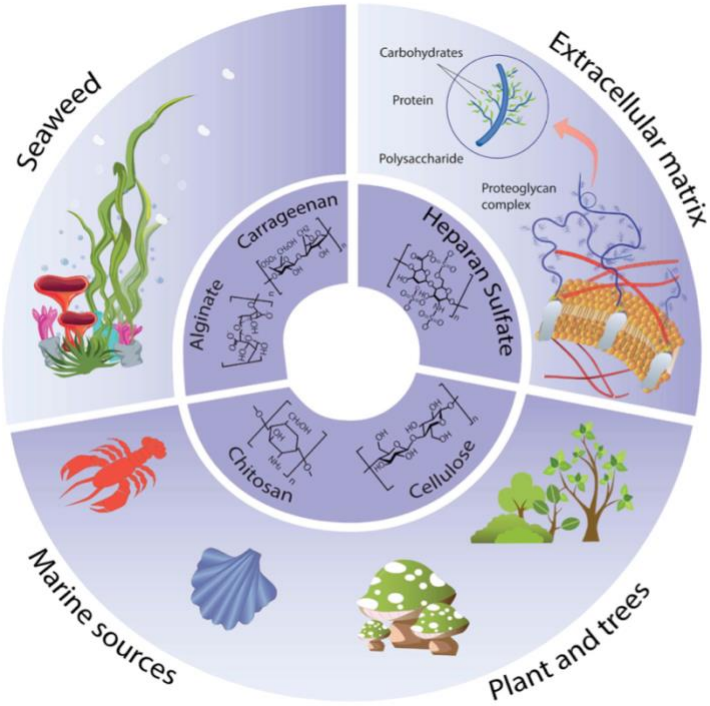

Figure 2 : Polysaccharides classification based on their natural source.[76] (Reprinted with permission)

Polysaccharides are highly biocompatible and biodegradable as they are derived from animal tissue ECM or plants such as marine algae in the form of alginate, carrageenan, fucoidan and, ulvan as shown in **Figure 2** originally from Dinoro *et al.*[76] Natural source of polysaccharides makes the cleavage of bonds possible with enzymes native to the body, thereby degrading them over time.

Polysaccharides readily form composites with calcium phosphate minerals which are widely explored for bone tissue engineering applications. For example, Song et al. compared

collagen membrane with chitosan-fibroin-HA membranes in a study in 54 rat calvaria (n=18) and found no significant difference in bone regeneration between the collagen group and polysaccharide group for their osteogenic ability.[77] However, another rat cranial defect study using chitosan with β-TCP, calcium oxide and zinc oxide microparticles showed enhanced rate of bone regeneration matching with the rate of degradation of the composite scaffold.[78]

Sulfated polysaccharides such as GAGs, heparin sulfate, carrageenan, chondroitin sulfate are increasing recognized for their natural bioactivity to aid in cartilage and bone formation for last 5-7 years.[76, 79, 80] Specifically, they have shown ability to bind to important growth factors such as BMP2 by facilitating the interaction between their sulfate group and amine stretch of BMP2.[81] Sulfated polysaccharide-based approaches are recently reviewed in detail by Dinoro *et al.*[76] Natural sulfated polysaccharides as well as chemically sulfated polysaccharides have been studied for their potential as osteogenic components in substitute bone grafts, however, preclinical animal studies testing sulfated polysaccharides are limited.

1.3 HYDROGELS USED FOR BONE REGENERATION

Hydrogels formation depends on cross-linking of polymer chains dispersed in an aqueous medium. Mechanisms for crosslinking are depicted by Zhang *et al.* as shown in **Figure 3.** Nonchemical crosslinking methods such as thermo condensation, self-assembly, ionic gelation, electrostatic interaction methods often offer reversible gelling advantage whereas chemical crosslinking allows tunability over the hydrogel properties.[82] Thermal condensation mechanism is common in many natural polysaccharide chains which get entangled in response to the change of temperature forming a packed polymer backbones (**Figure 3A**).[83, 84] Self-assembly of

macromolecules and proteins is facilitated through van der Waals forces, hydrogen bonds, and hydrophobic interaction (**Figure 3B**). The self-assembly of proteins such as collagen is dependent on peculiar arrangement of amino acids in collagen molecules which eventually form fibrous hydrogel in aqueous environment.[85, 86] Taking cues from collagen, O'leary *et al.* reported self-assembled structures at multiple length-scales[87] and Hartgerink *et al.* reported the function of such peptides to mineralize in similar way to that of collagen.[88] Another widely employed physical crosslinking mechanism employs chelation using ion or electrostatic interactions for macromolecules. For example, alginate which exists as negatively charged polysaccharide, derived from brown algae, can chelate with Ca^{2+} or other cations to form packed chains locking ions in between (**Figure 3C**).[89] Although many natural polysaccharides such as alginate, gellan gum, and hyaluronate are negatively charged due to carboxylic acid in their polymer backbone, chitosan and gelatin possess positive charge due to amine group. However, the variation in electrostatic charge density of these naturally sourced polymers can present challenges for precise quality control over hydrogel fabrication.[90] These oppositely charged polymers form entangled complexes (**Figure 3D**) resulting in hydrogels on mixing.[91] Chemical cross-linking methods are ideal when accurate spatiotemporal arrangement of chains and irreversible gelation are predominantly required properties. Typically, chemically active part in the macromolecular polymer structure covalently binds to other chains due to chemical or photo-stimuli to form hydrogels (**Figure 3E**). This is attained through condensation reactions between hydroxyl groups and carboxylic groups, radical polymerization, aldehyde complementation, and irradiation using high energy.[92] A more recent method of click chemistry has gained popularity due to its compatibility with cells and bioactive agents. A simple improvement to shorten the time taken compared to conventional chemical crosslinking for crosslinking has generated opportunities for

cell loading approaches. For example, bioconjugation of cells and hydrogels could be possible through click chemistry reactions such as thiol-vinyl sulfone and thiol-maleimide Michael addition, azide-alkyne cycloaddition, and thiolene photocoupling reactions. [93]

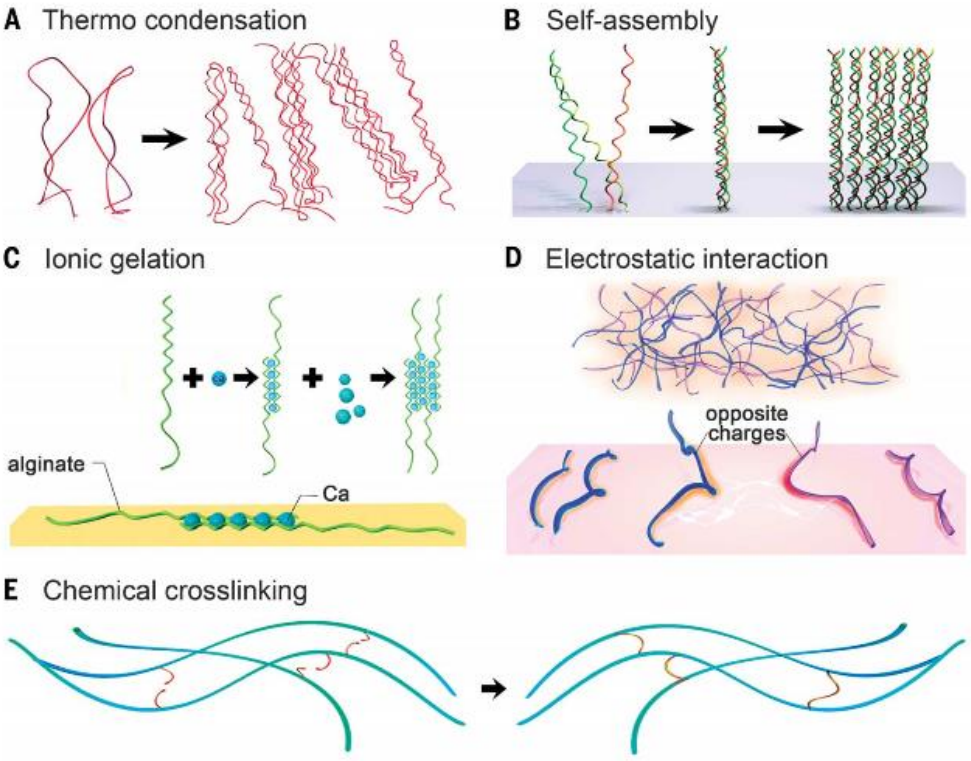

Figure 3: Cross-linking of hydrogels.(A) Thermally induced entanglement of polymer chains, (B) molecular self-assembly, (C) ionic gelation, (D) electrostatic interaction, (E) chemical cross-linking.[82]

(Reprinted with permission from AAAS)

Although these crosslinking methods produce hydrogels with varying degree of control and flexibility, more recent studies employ combinatorial approach to incorporate best from all options. For example, Annabi *et al.* demonstrated a combination of crosslinking approaches by first promoting self-assembly of graphene oxide particles with photoreactive methacryloyl-substituted tropoelastin through hydrogen bonding hydrophobic interactions, and then UV photocrosslinking to obtain highly elastic biocompatible hybrid hydrogels.[94] Zhang *et al.* has

recently reviewed progress in the hydrogel field towards tough or self-healing hydrogels as well as shape-assisted hydrogels which exhibit excellent control over the mechanical and physicochemical properties of the hydrogels due to advancement of nanofabrication technologies.[82]

Based on the physical structure of the hydrogels they are classified in three major categories: 1) hydrogel microbeads and nanoparticles 2) bulk hydrogels 3) fibrous hydrogels. Each category is discussed in detail below.

1.3.1 Hydrogel microbeads and nanoparticles

Small size of microbeads and nanoparticles are beneficial to achieve higher loading of drugs and stem cells due to its greater surface to volume ratio, thereby increasing mass transfer capacity as delivery systems for bone regeneration.[95] Moreover, smaller-sized microbeads can achieve high resolution cell organization than conventional microbeads. For example, Moshaverinia *et al.* reported alginate microbeads to encapsulate and deliver dental-derived MSCs using calcium chloride for ionic crosslinking. The micro-CT images showed efficient ectopic bone formation inside and around microbeads in mice after 8 weeks after implantation.[96]

Newer microfluidic based methods for microbead preparation methods offer greater control over the size of microbeads compared conventional methods such as emulsification, electrostatic droplet extrusion, air jetting, and in-situ polymerization. For example, non-equilibrium microfluidic method could achieve hydrogel beads of about 100 μm by using water/oil interface with hydrogel precursors which shrunk and condense rapidly when introduced to oil.[97, 98]

Hydrogel nanoparticles are also referred as nanogels. Nanogels are commonly synthesized through emulsion polymerization methods such as inverse emulsion polymerization and distillation-precipitation polymerization. For example, Vinogradov *et al.* reported a nanogel made of poly(ethylene oxide) (PEO) and polyethyleneimine (PEI), (PEO-cl-PEI). Here, anionic amphiphilic molecules or oligonucleotides interacted with PEO-cl-PEI to form poly ion-complexes which led to the precipitation of the dispersed gel particles. Interestingly, the hydrogel complexes could still form stable aqueous dispersions due to the stabilizing effect of the PEO chains.[99] Moreover, cholesterol-bearing pullulan (CHP) nanogels have also exhibited capability to deliver multiple proteins and enzymes. For example, acrylate group modified CHP nanogels successfully promoted higher bone regeneration in rats within four weeks by delivering human fibroblast growth factor 18 (FGF18) and rhBMP2. [100, 101]

1.3.2 Bulk hydrogels and controlled release

Injectable and implantable hydrogels are used as isotropic bulk biomaterials to shield the cells or growth factors from enzymatic degradation due to hydrophilic microenvironment.[96] Moreover, locally delivered therapeutics without carrier hydrogel may translocate to other sites inducing inflammation or adipogenic induction.[102] For example, in an interesting study, α2β1 integrin-specific peptide (GFOGER) functionalized PEG hydrogel was loaded with BMP2 and implanted in murine radial defect. It promoted significantly better osteoinduction at low dose of BMP2 compared to free BMP2 after eight weeks. This could be possible by sustaining activity of BMP2 through encapsulation in the hydrogel.[103] Moreover, ideal osteoinductive hydrogel should release bioactive moieties in a spatiotemporally controlled fashion to allow recruitment,

assembly, and differentiation of the native cells to ensure continuous and mature bone formation.[104, 105]

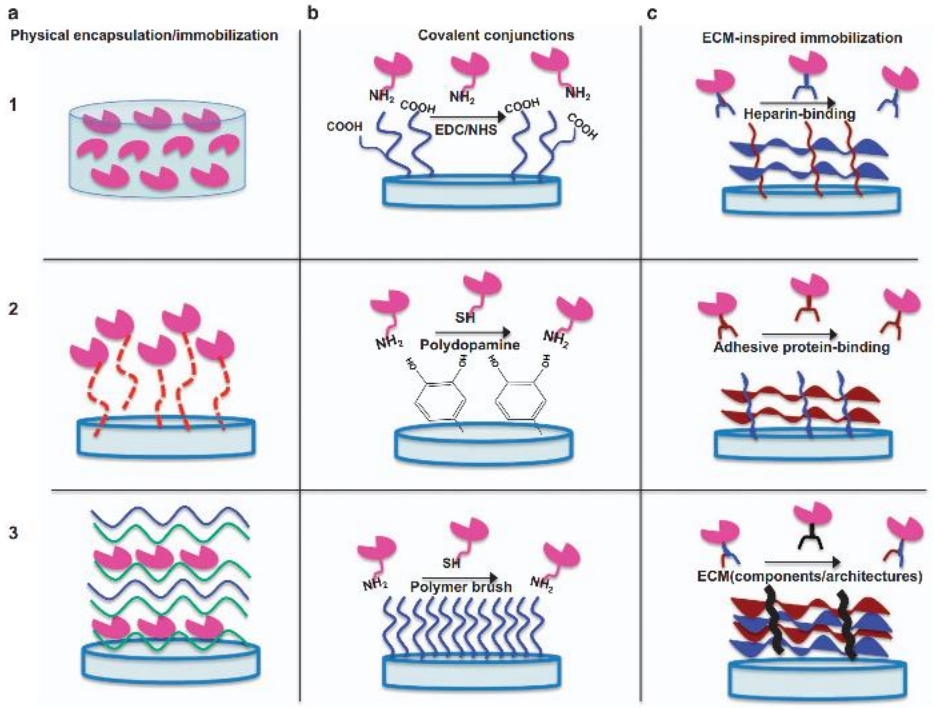

Figure 4 Approaches for immobilization of growth factors to biomaterials a) physical encapsulation, b) covalent conjections, and c) ECM-inspired.**[105]** (Reprinted with permission)

Multiple growth factor release could also be achieved through a combination of multiple encapsulation methods. For example, Barati *et al.* designed a self-assembled nanogel to release BMP2 and VEGF by using patterned constructs with human mesenchymal stem cells (hMSCs) and endothelial colony-forming cells (ECFCs) encapsulated in the hydrogel matrix.[106] Their *in vitro* their differentiation studies showed markers for mineralization and vascularization in correlation with the *in vitro* spatiotemporal release data.

Wang *et al.* recently reviewed strategies for controlled growth factor release from the hydrogel via physical, covalent, or ECM inspired immobilization methods (**Figure 4**) for growth factor loading in hydrogels for various tissue regeneration applications including bone regeneration.[105]

1.3.3 Hydrogel fibers

Contact guidance for encapsulated cells or native cells at the bone injury site is crucial initial step for the success of orthopedic biomaterials.[107] Hydrogel fiber diameter is commonly reported in the range of nanometers to micrometers which are in the ideal range for the cell adhesion and spreading.[108, 109] The structural properties of hydrogel fibers depend on fabrication approaches as well as crosslinking methods. Most popular fiber fabrication approaches include electrospinning,[107] wet spinning,[97] interfacial polyionic complexation (IPC),[91, 110] hydrodynamic spinning,[111] and 3D printing.[112] Most of these fibrous hydrogels require crosslinking assisted by thermal or UV stimulation or enzymes.[113]

Micro- and macro-arrangement of hydrogel fibers is widely recognized to provide biomimetic topography and contact guidance to the cells. Moreover, surface functionalization of the hydrogel fibers with naturally binding arginine-glycine-aspartic acid (RGD) peptide, can provide high affinity and control over cell assembly to attain ideal tissue microarchitecture.[111] However, most of the available literature on bone tissue engineering hydrogels focuses on mixture of long chain polymers with calcium phosphate mixture with poor control over its multi-scale architecture. These mineral-hydrogel composites still show osteogenic activity to a limited extent if used without growth factors. For example, Yao *et al.* showed that Poly(γ–glutamic acid) (γ–PGA) and β–TCP electrospun hydrogel fibers promoted new bone regeneration in rat calvarial defect after eight weeks, although by only a margin of 10% newly formed bone region compared to empty defect.[114] Another hydrogel fiber study showed osteogenic activity of PLA/PGA electrospun along with calcium phosphate cement (CPC) in rat cranial defect model better than empty or CPC condition and similar to rhBMP2 condition after 24 weeks of implantation.[115]

Similarity of composite with rhBMP2 condition was attributed to the possibility of inactivation of rhBMP2 or its strong binding with CPC.

Although numerous hydrogel fiber studies have attempted to regenerate bone in combination with other osteogenic agents, hydrogel fibers showing characteristic bottom-up self-assembly and hierarchy similar to collagen have not been reported. IPC technology provides unique opportunity to incorporate such bottom-up self-assembly to incorporate biomimetic fibrous architecture similar to bone-ECM.

1.3.3.1 Interfacial polyionic complexation

IPC phenomenon was first reported in 1998 as hydrogels that can be produced in various shapes including fibers using chitosan and gellan gum.[116] These IPC fibers showed characteristic nervation or veining surface which distinguished them from other fiber types.[117]

(a) Mechanism

The fiber formation process starts with a contact between two oppositely charged polyelectrolyte solutions which results in formation of a continuous interface. This viscous interface acts as a barrier for the two solutions to mix freely which is a crucial prerequisite for IPC process. Next, the interface is pulled upwards using pipet or tweezers, thereby disrupting continuous interface, leading to scattered domains of complexation which act as nuclear fiber. Further growth and bundling of the nuclear fibers results in a thick IPC fiber.[110] Proposed mechanism is depicted in a diagram (reprinted in **Figure 5**) by Wan *et al.* in a thorough review about IPC processes and applications. The underlying principle of interfacial complexation has been reported to depend on 1) the viscosity, which is proportional to polysaccharide concentration and 2) the fiber drawing speed or fiber drawing force at the interface of oppositely charged

polysaccharides.[118] It is necessary to keep optimum viscosity or pre-gel viscosity (right before it gels) of the polyionic solutions to facilitate interfacial fiber formation. Ideally, viscosity should be such that it will not allow premature diffusion of polyelectrolyte chains and on the other hand, it should not be too viscous to prevent replenishment with fresh polyelectrolyte as soon as the interfacial fibrous membrane is formed and pulled out as a fiber. Such optimum viscosity is important for continuous formation of fibers.[118, 119] Indeed, Wan *et al.* demonstrated that the fiber formation using a combination of CHT (0.5% w/v) and ALG (2% w/v) resulted in fibers with beads or blobs at regular interval along the fiber as the rate of interaction of the solutions and fiber drawing speed did not match.[120] Moreover, Wang *et al.* pointed out electrostatic and hydrophobic interactions as the underlying driving forces for fiber formation using isothermal titration microcalorimetry.[121]

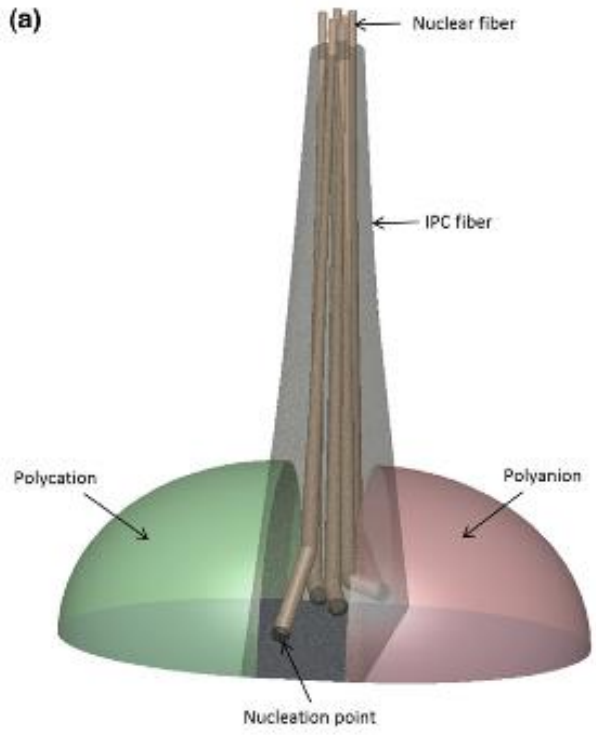

Figure 5: Possible mechanism of IPC fiber formation

[110] (Reprinted with permission)

(b) Fabrication methods and tissue engineering applications

As long as the conditions amenable for fiber formation are maintained, spinning processes can be employed to achieve large scale continuous fiber collection.[122, 123] Particularly, Ohkawa *et al.* designed a set-up to inject one of the polyelectrolyte solution into a the other oppositely charged polysaccharide solution in a bath resulting in fiber formation. This fiber is continuously collected by spinning wheel and dried as depicted in **Figure 6**. IPC fibers are also used to encapsulate various biologics such as cells, proteins, peptides, growth factors.[124-126] Aqueous environment provides excellent stability to the encapsulants as compared to conventional non-aqueous methods such as emulsion and solvent extraction. Moreover, cell encapsulation using IPC has two major advantages: 1) it allows excellent mass transfer and 2) IPC offers a single step process which prevents formation of necrotic core observed in cells encapsulated using microspheres[127] and reduces risk of contamination or phenotypic changes during the processing.

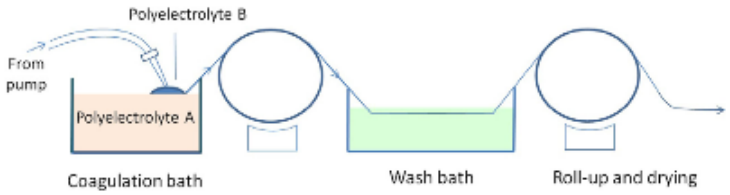

Figure 6 Continuous flow spinning of IPC fibers Coagulation bath, wash bath, and roll-up and drying steps depicted in the schematic.[110, 122] (Reprinted with permission)

Moreover, the electrostatic nature of the interaction can be exploited for sustained release if the encapsulant is electrostatically charged. The affinity between the polyelectrolyte and encapsulant would determine the strength of the interaction, and thus it would affect the sustained release. For example, Liao *et al.* released two molecules: 1) platelet derived growth factor (PDGF)

and 2) avidin. They both have same amount of charges but varying molecular weight. The lower molecular weight PDGF showed sustained release compared to avidin as PDGF formed stronger electrostatic interaction with fibers due to its higher charge density.[128]

Moreover, microfluidic methods are also employed to fabricate single fibers as well as scaffolds with multiple layers.[91] We have reported a microfluidic-based IPC fibrous scaffold fabrication method with a premixed graphene in chitosan and gellan gum interacted with interfacial contact as shown in **Figure 7.**

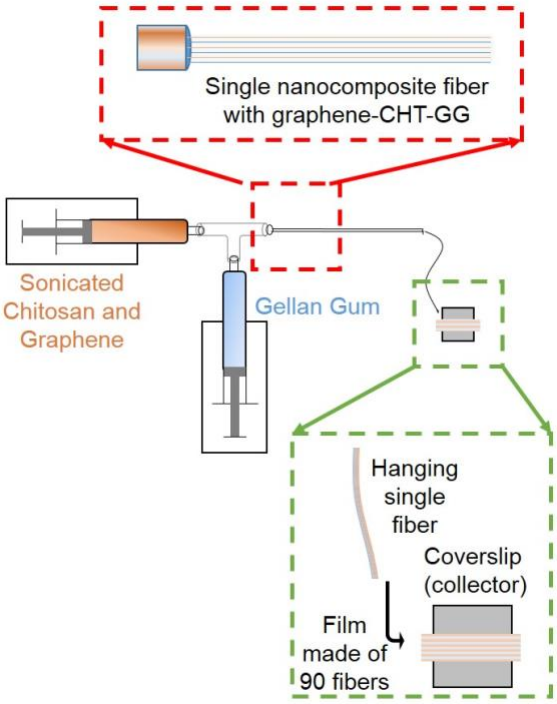

Figure 7 : Interfacial interaction using microfluidic approach. A schematic representation of microfluidic method to fabricate IPC fibrous composites comprising of graphene-chitosan-gellan gum (graphene-CHT-GG))[91] (Reprinted with permission)

In the last decade, IPC fibers has shown versatile application by simple electrostatic self-assembly with multiple electrolytes in the same fiber, known as multicomponent IPC (MIPC),[129] as well as easy physical entrapment of nanoparticles[91] and cells.[130] [131]

Highly biocompatible properties and collagen-mimetic bottom-up hierarchy of IPC show great potential for bone tissue engineering. However, IPC fibers have not been evaluated for bone regeneration applications even though many polysaccharides used in IPC literature are widely acknowledged as candidate materials for bone tissue engineering.

1.4 NATURAL BONE STRUCTURE AND BONE REPAIR

1.4.1 Bone structure

Bone is formed by deposition of inorganic minerals in an organic matrix, forming inorganic-organic nanocomposites. 80% of the bone in the body is compact and the remaining 20% is spongy. Bone is composed of minerals, proteins, and water as shown in **Figure** 8.

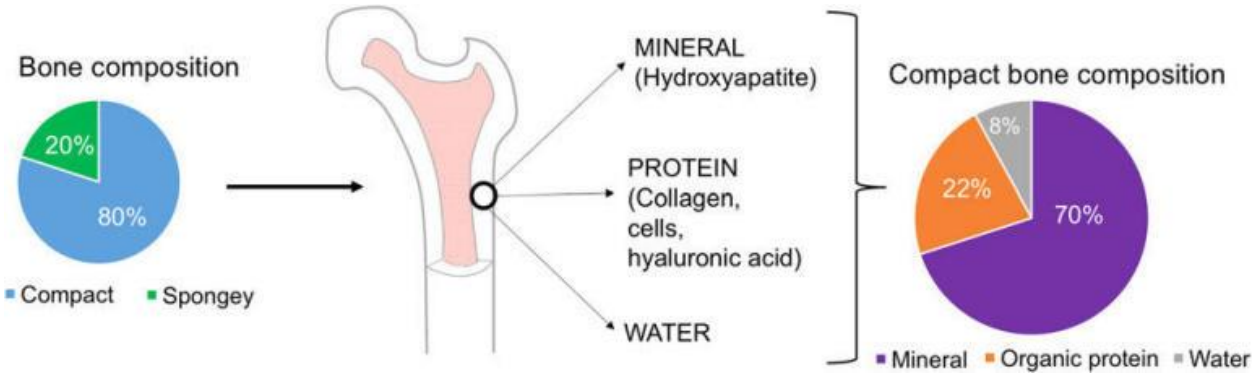

Figure 8 : Composition of bone. Schematic showing composition of bone between compact (cortical) and spongy (cancellous). Cortical bone is evaluated further and broken into its constituents; 70% mineral, 22% organic protein, 8% water.[132] (Reprinted with permission)

Mineral deposition is a series of complex yet precisely controlled events. It is controlled largely by the organic component which includes cells, collagen and other proteins, from which cells constitute a very small fraction and collagen comprises 85-90% of other extracellular organic

matrices[133]. Self-assembled nano-scale building blocks and their hierarchical organization confer unique strength, flexibility and facilitates functional feasibility to the tissue[134]. Although the mechanisms of mineralization are not fully understood, mineral sequestration, nucleation and its growth have been found to constitute three key steps in the process [133, 135, 136].

Collagen acts as an organic template to guide mineral deposition along with other physical and chemical interactions [133, 137]. Collagen has a structural hierarchy with uniformly distanced staggered (hole-region) and eclipsed/overlapping regions which give it characteristic dark and light bands. At nano-scale, such structure exhibits periodicity in banding pattern (distanced at 64-70nm) which controls mineral deposition[133]. The mineral deposition follows structural and physicochemical influences exerted from the collagen structure and ends up forming periodic patterns of mineral deposition. Such mineralized collagen fibril form collagen fiber which further forms lamella and osteon macrostructures as shown in **Figure 9.**

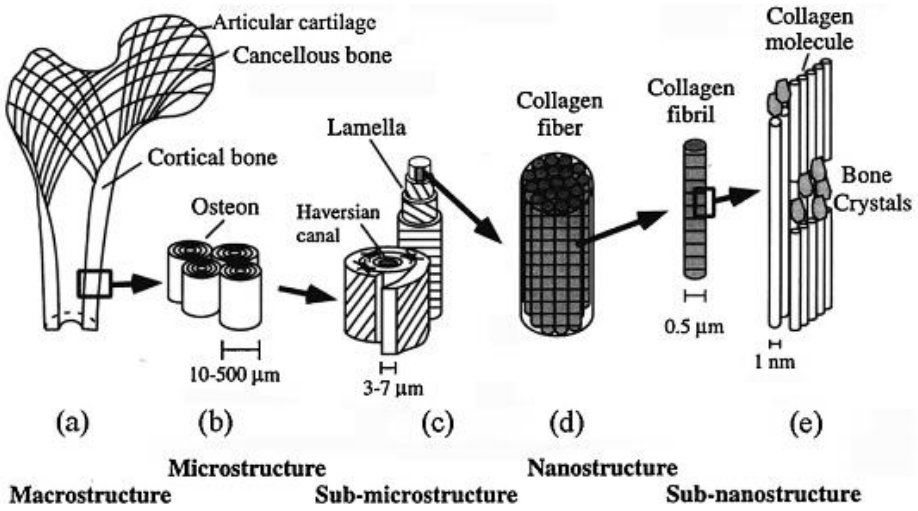

Figure 9 : Hierarchical structural organization of bone. (a) cortical and cancellous bone; (b) osteons with Haversian systems; (c) lamellae; (d) collagen fiber assemblies of collagen.[138] (Reprinted with permission)

Hole-regions in collagen fibrils and functional groups (such as carboxylate, sulfate, etc.) in the extracellular matrix control mineralization through generation of nucleation sites.[133] Features of collagen matrix-mineral interaction can be recapitulated using synthetic and natural polymers.

1.4.2 Bone minerals

Bone minerals are made of calcium phosphates with apatite-like structure containing carbonate.[139] Bone minerals consist of a significant amount (3–8 % w/w) of carbonate ion substitution with hydroxide (OH^-) ions. Calcium phosphate (CaP) apatites can be represented with the same formula $Ca5(PO4)3X$ where X can be for example an OH^- ion (hydroxyapatite) or a CO_3^{2-} ion (carbonated apatite). The apatite structure is tolerant of such ionic substitutions. Moreover, these apatites are formed in the presence of a variety of trace metals and ions from the bloodstream, therefore, CaP apatites with HPO_4 ion, CO_3^{2-} ion, Al, Pb, citrate ions are often reported through bone mineral analysis.[140] These substitutions slightly change the structure of apatites and often alter physical properties, such as solubility, brittleness, strain, thermal stability, and optical properties like birefringence.[139]

1.4.3 Bone growth

Bone is known to repair/regenerate itself following fractures or in case of minor bone loss. Bone healing can be observed at three length-scales: organ, tissue and cells. Organ-level changes can be detected by radiology whereas tissue and cellular level changes require microscopy with different resolution capacity.

1.4.4 Mechanisms of bone growth

The healing of bone is comprised of two types of bone regeneration: intramembranous ossification and endochondral ossification. Irrespective of the mechanism, bone regeneration process overlaps in its underlying mechanisms, for example, involvement of mesenchymal stem cells (MSCs) is integral to both the mechanisms.[141] It is the spatiotemporal availability of cellular, biochemical, and structural cues in the bone defect area that determines the type of mechanism. Intramembranous ossicification is involved in bone formation for irregularly shaped bones such as cranial bone whereas endochondral ossification is involved in long bones (bones that are longer than their diameter) such as femur. For simplification of discussion we classify the bones in the body as craniofacial and long bones.

1.4.4.1 Craniofacial bone

Intramembranous ossification starts with MSCs cluster recruited at the injury site mostly during the first week of injury. The MSCs cluster, under favorable cellular conditions, start differentiation into osteoblasts and begin deposition of collagen type I which further promote mineralization and growth of bone. Bone growth through this mechanism often appear initially as non-union bone spicules. This is commonly observed mechanism for non-load bearing bone in the skull.[142, 143]

1.4.4.2 Long bone

Endochondral ossification starts with chondrocyte hypertrophy on the surface of the native bone which secrete collagen type I. As chondrocytes mature, they stop secretion of collagen and begin secretion of alkaline phosphatase. Simultaneously, MSCs which are mostly sourced from

periosteal layer populate the injury area after initial blood clotting and inflammation in the injury area and differentiate into osteoblasts. As the osteoblast activity increases, the matrix hardens with mineralization which is further remodeled by osteoclasts in the area to make way for central medullary cavity for bone marrow. This type of bone growth is characterized by formation of new bone on the surface of native bone. This way, bone gets further elongated until bridged via deposition of new endochondral bone deposition on regenerated bone. This mechanism is common to load-bearing long bones such as femur, tibia-fibula and semi-load bearing long bones such as radius-ulna of upper limb.

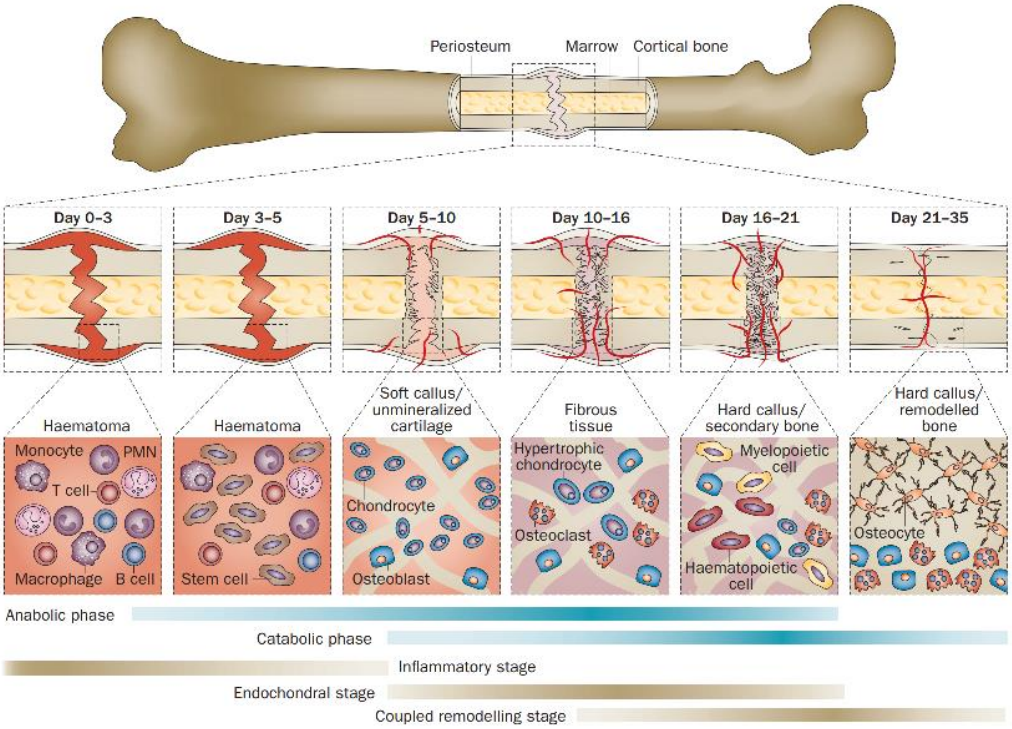

Figure 10 : Long bone (femur) repair stages Metabolic stages (blue bars) of fracture healing overlap with biological stages (brown bars). The primary cell types found at each stage are denoted. The time scale denoted here is equivalent to a mouse closed femur fracture fixed with an intramedullary rod.[142] (Reprinted with permission)

Bone repair in long bones can be listed as five stages which are reviewed in detail by Einhorn and Gerstenfeld and depicted in a schematic shown in **Figure 10**.[142] The anabolic phase increases the tissue volume via recruitment and differentiation of stem cells from skeletal and vascular tissue. Cartilaginous callous formation is observed next to the fracture line. As chondrocytes begin differentiation, the ECM of cartilages starts mineralization and chondrocyte apoptosis marks the end of anabolic phase.[144, 145] With some overlap in timeline, catabolic phase begins which is characterized as the remodeling of callus tissue formation through resorption of cartilage by osteoclasts and formation of nascent vascular bone tissue by osteoblasts. These metabolic phases can be classified as consequent biological phase of initial inflammation phase for first week, followed by endochondral stage, often referred as reparative phase (2-3 weeks) and remodeling stage (3-12 weeks), respectively. Out of the three phases, inflammation phase takes the shortest duration and often forms granulation tissue which is crucial to determine the course of the rest of bone repair phases.

Deschaseaux *et al.* have reviewed hierarchical scheme of molecular mechanisms underlying the formation of osteoblastic progenitors and mature osteoblasts from MSCs in a great detail for long bone regeneration.[143] Additionally, Bueno and Glowacki reported a comprehensive list of advantages and limitations of all available options for bone grafts as shown in **Figure 11.**

Table 1 | Summary of advantages and limitations of approaches available for bone tissue engineering

Approach	Advantages	Limitations
Scaffolds		
Biodegradable	Maintain mechanical stability while being replaced with new bone; remodeling bone fills entire site	Byproducts of degradation can be harmful; degradation rate must be synchronized with new bone growth to preserve mechanical stability
Permanent	Immediate mechanical stability	Nidus for infection; immunological response; material fatigue or erosion
Preformed	Mechanical stability; control over structural properties	Does not conform to shape
Injectable	Conforms to shape; minimally invasive	Limited porosity; limited mechanical strength
Traditional fabrication techniques (e.g. textile processing)	Cost-effective	Limited control over structural properties
CAD/CAM fabrication techniques (e.g. rapid prototyping)	Advanced control over structural properties	Complex fabrication
Demineralized bone matrix	Biocompatible; osteoinductive; off-the-shelf; inexpensive	Concerns about immunogenicity and infection; variable efficacy
Natural polymers	Biocompatible	Limited mechanical strength
Synthetic polymers	Tunable structural, mechanical, and degradation properties	Concerns about biocompatibility and immunogenecity
Ceramics	Biocompatible; good drug delivery; FDA-approved for use in bone regeneration	Brittle; limited to non-weight-bearing sites; injectable formulations present low porosity
Bioactive glasses	Bone binding; osteoconductive	Brittle
Composites	Take advantage of the parent materials' qualities, while mitigating their limitations	Complex fabrication
Bioactive factors		
Growth factors	Enhance cellular activities such as proliferation, migration, bone formation, and angiogenesis	Complicated delivery; leakage; expensive
Platelet rich plasma	Autologous; inexpensive	Mixed reports on efficacy; complex logistics to prepare
Enamel matrix derivative	Available for periodontal use	Available products are porcine
Gene therapy		
Ex vivo transfection	Cell-specific	Complex; inefficient; compromised cell survival
Adenovirus gene transfer	Efficient transfection	Immunogenicity; uncontrolled gene expression outside defect site; disturbance of host's genome
Non-viral delivery	Economical; simple; non-immunogenic; effective	Inefficient; transient expression; low cell specificity
Bone grafts		
Autograft	Immunocompatible; osteoconductive	Need for harvesting surgery; graft site morbidity
Allograft	Off-the-shelf; osteoconductive	Concerns about disease transmission and immunogenecity; variable efficacy
Cell-based approaches		
Autologous marrow	Immunocompatible; readily available	Does not provide mechanical stability
Autologous MSCs/scaffold constructs	Immunocompatible cells; mechanical stability	Limited numbers of cells; limited clinical data available
Allogeneic cells	Some currently available products do not require FDA-approval	Limited clinical data available

Abbreviations: CAD/CAM, computer-aided design and manufacturing; MSCs, marrow stromal cells.

Figure 11: Summary of bone grafts- their advantages and disadvantagesA brief summary of advantages and disadvantage of all available options for bone grafts.[146] (Reprinted with permission)

1.5 HYPOTHSIS AND SPECIFIC AIMS

Main aim of this research is focused on bioinspired design of materials to promote bone regeneration without the use of added growth factors. We hypothesize that oppositely charged polysaccharides will self-assemble due to interfacial polyionic complexation (IPC) forming collagen-inspired hydrogel fibers which will promote mineral sequestration due to electrostatic charges and the multi-scale hierarchical structures will facilitate bone-mimetic mineral deposition. We propose that these mineralized scaffolds will enhance bone regeneration *in vivo*.

To test this hypothesis, three aims are proposed:

Aim 1 will develop and optimize fabrication process of IPC fibers and hydrogel scaffolds prepared by their anisotropic collection. The fibrous hydrogel scaffolds were further characterized for various material properties. This aim is further divided into three sub-aims.

Sub aim 1.1: Determination of critical fabrication process parameters such as concentrations, viscosity, and speed of pumps used for interfacial mixing of polysaccharides to fabricate fibrous hydrogel scaffold.

Sub aim 1.2: Development of automated method of fabrication for fabrication and anisotropic collection of fibrous hydrogel scaffolds

Sub aim 1.3: Encapsulation of small molecule and nanoparticles in the fibrous hydrogel scaffold.

Aim 2 will characterize *in vitro* mineralization bioactivity of the fibrous hydrogel scaffolds and their *in vivo* efficacy in non-load-bearing critical-sized mouse calvaria defect model. The

bioactivity of non-mineralized and mineralized fibrous hydrogel scaffolds was further tested *in vitro* using mouse pre-osteoblast cells. This aim is further divided into three sub aims.

Sub aim 2.1: Characterization of *in vitro* mineralization bioactivity of fibrous hydrogel scaffolds for mineral morphology and chemical type of the deposited minerals after incubation in simulated body fluid (SBF).

Sub aim 2.2: Bone regeneration efficacy of non-mineralized and mineralized hydrogel scaffolds in non-load-bearing critical-sized mouse calvaria defect.

Sub aim 2.3: Evaluation of *in vitro* bone regeneration bioactivity of fibrous hydrogel scaffolds using mouse pre-osteoblast cells through osteogenic mRNA and protein characterization.

Aim 3 will develop fibrous hydrogel scaffolds into cylindrical fibrous hydrogel scaffolds and evaluate their efficacy to regenerate bone in semi-load bearing rabbit ulna defect model. This aim is further divided into two sub aims.

Sub aim 3.1: Development and material characterization of cylindrical fibrous hydrogel scaffolds.

Sub aim 3.2: Evaluation of *in vivo* efficacy of cylindrical fibrous hydrogel scaffolds in semi-load-bearing critical-sized rabbit ulna defect model.

Successful completion of these aims will present IPC fibrous hydrogel scaffolds as a versatile platform technology, potentially for multiple tissue engineering applications in future. Moreover, it will establish fibrous hydrogel scaffolds as bioactive osteogenic substitute bone grafts for non-load-bearing and semi-load-bearing defects without added growth factors.

2 SELF-ASSEMBLY OF MULTI-SCALE ANISOTROPIC HYDROGELS THROUGH INTERFACIAL POLYIONIC COMPLEXATION

[Patel A, Sant V, Velankar S, Dutta M, Balasubramanyam V, Sane P, Agrawal V, Wilson J, Rohan L, Sant S.] *Submitted*

2.1 BACKGROUND

Polysaccharides have been widely used as biomaterials intended for a variety of tissue engineering and drug delivery applications.[72, 147-151] Most polysaccharides inherently possess hydrophilic polymer chains and electrostatic charges, which have been exploited for fabrication of ionically crosslinked hydrogels using ions such as calcium, magnesium, sodium, etc.[152-154] or other oppositely charged polymers.[110] Such properties provide an excellent flexibility to load cells, small molecules or proteins into the hydrogel[150]; however they offer limited structural complexity observed at multiple length-scales in the biological tissues.[82] Such structural cues together with contact guidance are crucial to achieve desirable cellular response from the encapsulated cells coming in direct contact with the biomaterial scaffolds. Multi-scale hierarchy and fibrous architecture are two of the bioinspired features that are most challenging to incorporate into the hydrogel structure. Traditional bulk hydrogels are also known to possess poor mechanical strength unless additional strategies such as chemical or physical crosslinking or hybridization with nanomaterials such as carbon nanotubes or graphene are employed.[82, 91, 155] Photo-crosslinking has been one of the most popular approaches; however, irradiation used during photo-

crosslinking generates free radicals, which often raises the concerns about the release of chemical photo-initiator into the tissue at a later time and phenotype stability of the encapsulated cells.[156]

In the last two decades, several studies have leveraged electrostatic interaction of charged polysaccharides for hydrogel fabrication.[82, 91, 157] This not only obviated the use of toxic chemical crosslinking agents but also formulated mechanically stronger hydrogels using flexible fabrication methods such as interfacial polyionic complexation (IPC).[158] Polysaccharides, being large molecules, were easy to adapt for IPC related methods to produce single fibers or fibrous bulk hydrogels.[159, 160] In fact, IPC fiber formation could be achieved simply by using a pair of tweezers or a pipet tip.[161, 162] However, due to the complexity of collective effect of process parameters such as temperature, concentration, viscosity, speed of interfacial mixing, and requirement of manual handling, majority of research community has focused on bulk mixing approaches or formation of isotropic bulk-fibrous complexes. Advancement of microfluidic technology has helped petri plate-based bench-scale IPC method leading to flexible production of IPC single fibers.[131, 163] A simple rotating slide holder,[164] wet spinning,[158] rolling pulley setup similar to nylon fiber fabrication,[98] and other variations of such apparatus have been used to further collect the fibers into fibrous biomaterials.[110, 119, 165] Although these methods have demonstrated advancement of technology for tissue engineering applications such as prevascularized tissue constructs, cell encapsulation, 3D cell culture, the adaptability of these methods to fabricate multi-layered, anisotropic, and hierarchical scaffolds on multiple length scales is still limited.

We have recently reported a semi-automatic microfluidic approach to fabricate IPC-based nanocomposite scaffolds using oppositely charged chitosan and gellan gum encapsulating graphene nanomaterials.[91] In this study, our goal was to develop a versatile fabrication platform

for IPC-based scaffolds with varying fibrous architectures (parallel vs. perpendicular) and ability to encapsulate small molecules and nanoparticles. To achieve this goal, we first optimized polymer-related parameters to facilitate continuous fiber formation using IPC, and further developed a fully automated and flexible hydrogel fabrication platform technology to assemble anisotropic hydrogels with multi-scale hierarchy. We used chitosan as a common cationic polysaccharide paired with three different anionic polysaccharides to test the flexibility of fabrication platform as well as to study the effect of each anionic polysaccharide on the properties of the resulting fibrous hydrogel scaffolds. Fiber collectors reported so far have utilized pulling of the fiber from the interface of oppositely charged solutions; however, we report a continuous fiber production method by continuously feeding oppositely charged polysaccharide solutions into interfacial mixing chamber. Moreover, we developed automated collector with two coordinated motors as a new platform technology to reduce user dependent variation and enhance robustness of the fabrication process. We further demonstrate versatility of this platform to fabricate hydrogels with different fibrous alignments as well as develop scaffolds with nanoparticle- and small molecule-loaded IPC fibers. Characterization of these hydrogels showed multi-scale hierarchical structure, mechanical strength in megaPascal range, high cytocompatibility, and capability to load nanoparticles and soluble small molecules.

2.2 MATERIALS AND METHODS

2.2.1 Materials

Gellan gum (GG) (G1910), alginic acid (ALG) (A0682), chitosan (CHT) (C3646), acetic acid (695092), and Fluorescein isothiocyanate isomer I (FITC) (F7250) were all purchased from Sigma-Aldrich Co. (St. Louis, MO). Kappa carrageenan (KCA) (C41070) was obtained from Research Products International (Mt. Prospect, IL). Precursor to prepare cerium oxide nanoparticles, $Ce(NO3)3{\cdot}6H2O$) was obtained from Acros Organics, Thermo Fisher Scientific (Waltham, MA). Cell culture supplies including minimum essential medium alpha (MEM-α) and Dulbecco's phosphate-buffered saline (DPBS) were purchased from Mediatech Inc. (Manassas, VA) or Corning Inc. (Corning, NY) unless otherwise specified. Fetal bovine serum (FBS) was purchased from Atlanta biologicals Inc. (Flowery branch, GA).

2.2.2 Polysaccharide solutions preparation and Zeta potential measurement:

CHT (1% w/v) solution was prepared in aqueous acetic acid solution (1% w/v). ALG, GG, and KCA (1% w/v) were prepared in distilled water. The zeta potential of these polysaccharide solutions was recorded using Malvern Zetasizer 3000 (Malvern, Worcestershire, UK).

2.2.3 Rheological measurement for viscosity of polysaccharide solutions

Viscosity of each of the polysaccharide solutions was determined using CPE42 spindle on Brookfiled Viscometer DVIII LV (Brookfield Engineering Laboratory Inc., Middleboro, MA). Data was collected and processed using Rheocalc software (Brookfield Engineering Laboratory Inc., Middleboro, MA). Polysaccharide solutions of varying concentrations were placed in the sample cup and were allowed to equilibrate to 60°C for 5 min followed by a measurement program in which shear rate was increased from 19 to 95 sec^{-1} with 6 measurements each with 30 seconds interval.

2.2.4 Self-assembly and characterization of single fiber formation

2.2.4.1 Bulk mixing of oppositely charged polysaccharides and light microscopy

In a well of a flat bottom 24-well plate, CHT (1% w/v, 100 μL) and equal amount of either ALG, GG, or KCA (1% w/v) were mixed at 50 rpm on a Thermomixer R (Eppendorf North America, Hauppauge, NY) at 60°C for 1 min. Bulk mixing resulted in turbidity suggesting formation of complexes.

Zeiss PrimoVert microscope was used to capture light microscopy images of clear or turbid complexes or transparent fibrous hydrogels. Images were exported using Zen software (Zen 2012; Carl Zeiss Microscopy, Oberkochen, Germany).

2.2.4.2 Interfacial mixing of oppositely charged polysaccharides and turbidity (absorbance) studies

A hundred microliter of each of the solutions were added from opposite sides of the culture well such that they were could not mix immediately but rather mix at the middle of the well to form a membranous interface. Using volume displacement pipets, the crosslinked interface was pulled up and dispensed back 5 times in each well while temperature was maintained at 60ºC. Complex formation resulted in turbidity, which was determined using absorbance measurement at 630 nm (SpectraMax M5e, Molecular Devices, San Jose, CA).

Light microscopy of the complexes was done as described under bulk mixing studies.

2.2.4.3 Vertical syringe pump method to print CHT channels in KCA solution

Programmable syringe pump (BS300, Braintree Scientific INC., Braintree, MA) was set upright with a 10 mL syringe (REF302995, Becton, Dickinson and Company, Franklin Lakes, NJ) filled with either of 1.5%, 1.25% or 1% w/v CHT attached to a 18G needle (REF305185, Becton, Dickinson and Company, Franklin Lakes, NJ). A glass petri plate filled with KCA (1% w/v) was set on a hot plate at 60°C such that the needle touched the bottom of the petri plate. The infusion rate of syringe pump was set at 50 mL/h as the petri plate was moved in a linear direction diagonal to the petri plate. After printing CHT channels parallel to each other inside KCA solution in petri plate, a glass rod was moved across the direction perpendicular to the printed CHT channels.

2.2.5 Assembly of anisotropic fibrous hydrogel scaffolds with multi-scale hierarchy

2.2.5.1 Set up of programmed syringe pumps with interfacial mixing chamber

Two of the programmable syringe pumps (BS300, Braintree Scientific INC., Braintree, MA) were set at 50mL/h using 10mL syringes connected using Luer-lock three-way valve. The opening of the valve was connected to an 18G needle (REF305185, Becton, Dickinson and Company, Franklin Lakes, NJ). Syringes (10 mL, 14.5 mm diameter) were jacketed with temperature jackets (BS-SYR-H, Braintree Scientific INC., Braintree, MA) set at 60°C.

2.2.5.2 Optimization of fiber collection methods

Manual collection of fibers

Fibers were manually collected using two 2 cm x 2 cm plastic cover slips mounted over a glass slide at the tip of the needle. The plastic cover slips helped detach the dried hydrogels and cut it in precise shape and dimensions. The final anisotropic fibrous hydrogels were made of two layers, each consisting of 45 fibers aligned parallel to each other. This resulted in three types of hydrogels based on the oppositely charged polysaccharides pairs used as raw materials: CHT-GG, CHT-ALG, and CHT-KCA.

Automated collection of fibers

A metal gear motor (12V, RB-POL-283) was obtained from RobotShop Inc., Mirabel, Canada. The shaft was mounted with a circular acrylic plate clamped with a glass slide with cover slip rotating at a speed matching with fiber formation. The gear motor was mounted on a

programmable horizontal moving stage (XSLIDE®, Velmex Inc., Bloomfield, NY) and set at a speed to collect fibers parallel to each other without leaving gap in between the neighboring fibers. Gear motor and the programmable horizontal moving stage were set inside Isotemp™ incubator (Thermo Fisher Scientific, Waltham, MA) to maintain the temperature at 60°C. Gear motor speed was adjusted to match with the rate of fiber formation. Programmable stage was set at different speed ranging from 25 to 100 μm/sec at optimized speed of pump (50 mL/h) to determine the optimum stage speed for collection and close arrangement of hydrogels next to each other without gaps in between them. Hydrated hydrogel scaffold thickness was measured using electronic digital caliper (Marathon, Toronto, Canada).

Image analysis

Light microscopy images were captured at 20X magnification and were analyzed using FIJI (FIJI Is Just ImageJ, NIH) to quantify fiber alignment. OrientationJ plugin was used to carry out visual directional analysis and color survey. A color survey image and an orientation histogram were generated for each image based on the structure tensor for every pixel in the image using mathematical models.[166] This was repeated for at least three images per sample and three samples for each of the manual and automated collected hydrogels. User error was plotted from the standard deviation of orientation histogram values for each user. A histogram was plotted with an overlay of two conditions using GraphPad Prism 7 (GraphPad Software, La Jolla, CA). Fiber diameter was calculated by setting the scale using scale bar and measuring diameter of at least 10 fibrils per image for three images per group.

2.2.6 Encapsulation of small molecules and nanoparticles inside the fibrous hydrogels

5% w/v of our previously reported cerium oxide nanoparticles (CNP)[167] in the shape of sphere and rod were separately added to (1% w/v) CHT solutions and the mixture was homogenized at 10% amplitude for 10 min using Sonic Dismembrator (Model 500; Thermo Fisher Scientific, Waltham, MA). CNP-reinforced hydrogels with rod and sphere shape are referred as sphere-CNP-CHT-GG and rod-CNP-CHT-GG hydrogels. FITC solutions were prepared as 0.25 μg/mL in CHT or ALG (1% w/v) solutions.

2.2.7 Characterization of fibrous scaffolds

2.2.7.1 Scanning electron microscopy (SEM)

SEM was carried out on both individual hydrogel fibers and anisotropic fibrous hydrogels. Single hydrogel fibers were air dried and hydrogels were lyophilized, followed by sputter coating of gold-palladium (5 nm in thickness) using Cressington 108 auto sputter coater (Cressignton Scientific Instruments, UK). SEM micrographs were obtained using JEOL 9335 Field Emission SEM (JEOL, Japan) at an accelerated voltage of 3kV and a working distance of 8 mm.

2.2.7.2 Mechanical studies

Tensile mechanical testing was performed on CHT-GG, CHT-ALG, CHT-KCA, sphere- or rod-CNP-CHT-GG hydrogels using the eXpert 7601 Table Top Universal Testing System from ADMET with a 1kN load cell and GV-1T manual vise grips. The MTESTQuattro software was used for servo control and data acquisition. All the hydrogels were tested in the hydrated state.

Hydration was carried out by incubating the dried fibrous scaffolds in 1x PBS (10 mL) for 24h in a shaker operating at 50 rpm. The hydrated hydrogels were mounted between the grips of the mechanical tester using a paper window to avoid slippage from the grips.

Uniaxial tensile testing was performed as previously reported.[91] Uniaxial tension was applied to the hydrated hydrogels at a constant rate of 10 mm/min until sample failure. The stress was recorded in MPa and plotted against the strain which was recorded as the percentage extension from the initial position of the grips. The Young's modulus (E_m, MPa) was calculated from the linear region between 10% and 50% elongation for all three materials, which was chosen based on the overlap between the linearity of all three materials, and the ultimate tensile strength (UTS, MPa) was defined as the maximum value of stress encountered during the test. Overall percentage elongation was calculated as the extension at which complete failure of the sample occurred, based on observation of the fracture pattern of the sample. The toughness (the work of extension) of each sample was calculated as the area under the stress-strain curve and expressed in J/m^3.

2.2.8 MC3T3 mouse pre-osteoblast culture

The MC3T3 cells were cultured in Minimum Essential Medium *alpha* (MEM-α) supplemented with heat inactivated FBS (10% v/v) and antibiotics (Penicillin and Streptomycin, 1% v/v). The cells were cultured in T75 or T125 flasks in a humidified incubator at 37°C and 5% CO2. Fresh media was replaced every 2 days and cells were split 1:3 at 70% confluence.

2.2.9 Cell seeding on scaffolds

Cells were seeded on hydrogels as described previously.[91] Briefly, fibrous hydrogels with an area of 0.25 cm^2 were sterilized followed by seeding at a density of 90,000 cells/ hydrogel in 24-well plate. Each hydrogel was transferred into a new well after 1-day incubation to remove non-adherent cells. MC3T3 cells were cultured in growth media for 14 days for alamarBlue® assay.

2.2.10 Cytocompatibility study

Cytocompatibility study was performed using metabolic activity assessment as described previously.[91] Briefly, alamarBlue® assay (Thermo Fisher Scientific, Waltham, MA) was employed to assess metabolic activity of MC3T3 cells seeded on hydrogels over 14 days. alamarBlue® solution (10% v/v) was prepared in complete growth media and incubated (500 μL) with cell-seeded fibrous hydrogel hydrogels for 4h at 37°C. The fluorescence intensity was measured at excitation/emission wavelength of 530/590 nm using the microplate reader (SpectraMax M5e, Molecular Devices, San Jose, CA). The wells without cells containing only alamarBlue® solution in media were used as process controls for background fluorescence correction.

2.2.11 Immunofluorescent staining

Cell-seeded hydrogels were fixed using 4% paraformaldehyde for 20 min and washed three times with DPBS followed by the permeabilization with DPBS containing 0.1% Triton X-100 and

blocking in DPBS containing 0.1% Triton X-100 and 5% BSA for 1 h at room temperature. The cell nuclei were stained with Hoechst 33342 (Thermo Fisher Scientific, Waltham, MA). Actin was stained using ActinGreen 488 ReadyProbes Reagent (R37112, Molecular Probes, Eugene, OR).

2.2.12 Confocal microscopy

Confocal images were acquired using inverted confocal laser scanning microscope (Olympus Fluoview 1000; Olympus Corporation, Tokyo, Japan) using 633 nm wavelength lasers. Objective lens of 20X was used for the z-stack images with 10 μM thickness of each z-slice. Data are presented as maximum intensity projection of the z-stack.

2.3 RESULTS AND DISCUSSION

2.3.1 Bulk mixing of oppositely charged polysaccharides failed to facilitate continuous fiber formation

In this study, we chose CHT as a cationic polysaccharide to complex with three different anionic polysaccharides, namely, ALG, GG and KCA. These anionic polysaccharides were chosen based on the magnitude of their zeta potential compared to CHT and the charge-imparting group.

As shown in **Table 1,** ALG and KCA showed zeta potential similar to CHT whereas GG showed less than half the magnitude of zeta potential as CHT.

Polysaccharide	Zeta potential (mV) (charge density)
Chitosan (CHT)	82 (± 4.78)
Alginate (ALG)	-78.3 (± 6.47)
Gellan gum (GG)	-36.4 (± 7.22)
Kappa Carrageenan (KCA)	-79.5 (± 4.21)

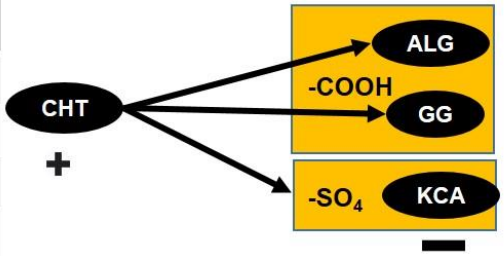

Figure 12: Zeta potential values of aqueous solutions of polysaccharides (left) and schematic presentation of pairs of polysaccharides

Moreover, as shown in the schematic in **Figure 12,** ALG and GG share carboxylate as the same charge imparting group, whereas KCA possesses sulfate as the charge imparting group.

Next, the rheological behavior was assessed for different concentrations of CHT and the three negatively charged polysaccharides, ALG, GG and KCA at 60°C to avoid gelation at lower temperatures. CHT (**Figure 13A1**) and ALG (**Figure 13A2**) solutions showed the least effect of shear rate on its viscosity at various concentrations. The GG solutions (0.5, 0.75, 1, 1.25%, **Figure 13A3**) showed similar behavior as ALG except 1.5% w/v GG demonstrated shear-thinning behavior with increasing shear rates. Interestingly, higher concentrations of KCA (1.25 and 1.5 % w/v) (**Figure 13A4**) also showed shear thinning behavior with increasing shear rates. Thus, for all

three negatively charged polysaccharides, concentrations at or below 1% w/v behaved similarly and showed viscosities in the range of 5-15 cP.

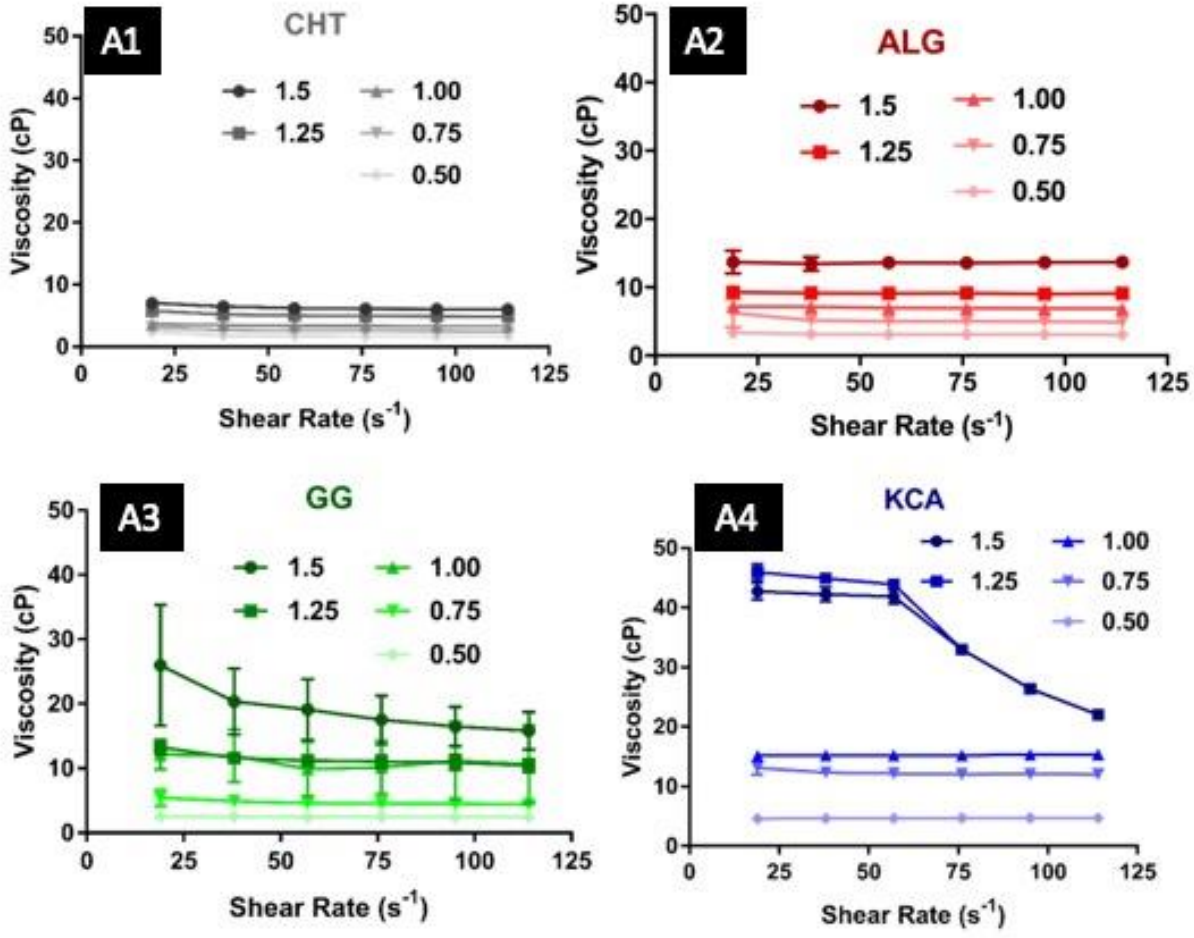

Figure 13: Effect of concentration on viscosity of polysaccharides Effect of varying concentrations of CHT (**A1**) ALG (**A2**), GG (**A3**) and KCA (**A4**) on the viscosity at various shear rates (n=3 per concentration). Concentration showed significant difference in two-way ANOVA analysis for all four polysaccharides. Shear rates showed significant difference only for CHT and KCA solutions;

We further studied the electrostatic complexation between positively charged CHT and one of the three negatively charged polysaccharides. The selected polysaccharides in the pair were mixed together in a well of 24-well flat-bottom plate at 50 rpm on a XY shaking hot plate at 60°C. The complexes formed due to electrostatic cross-linking showed two major morphological forms:

non-fibrous coacervates (**Figure 14A**) or fibrous structures (**Figure 14B**). Overall, these bulk mixing results could be explained as shown in schematic in **Figure 14C** as one of the solutions encapsulated inside the electrostatically cross-linked membranous interface. In some cases, rupture of such a capsule may have resulted exposing the capsule-membrane as cross-linked insoluble fibrous complexes.

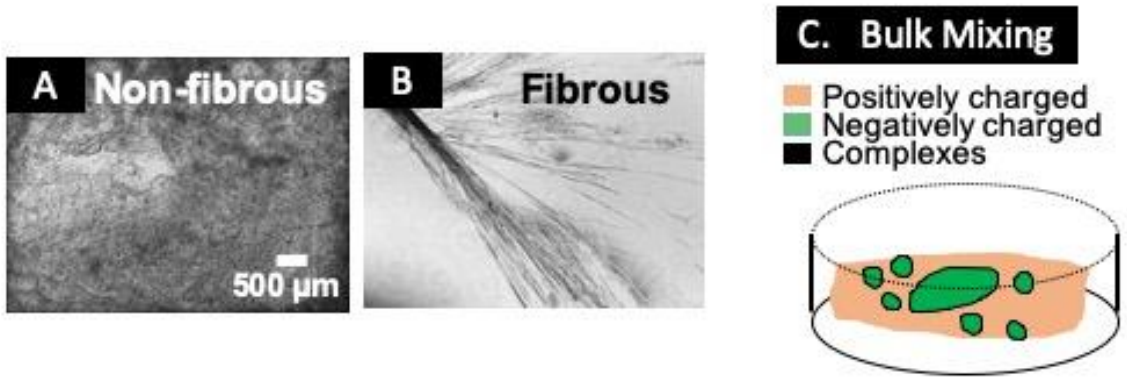

Figure 14: Non-fibrous and fibrous complexes as a result of bulk mixing of oppositely charged polysaccharides.A and B: representative light microscopic images of cross-linked fibrous and non-fibrous complexes resulted after bulk mixing of oppositely charged polysaccharide solutions. **C** depicts bulk mixing of oppositely charged polysaccharide solutions on a XY plate shaker leading to encapsulation of one of the solutions inside the electrostatically cross-linked membranous interface.

In a similar approach, Mendes *et al.* developed hydrogels with electrostatic interactions using negatively charged xanthan gum and positively charged CHT oligomers.[168] They studied effect of order of addition of both solutions on electrostatically crosslinked capsule formation. When a viscous solution was added over the less viscous one, it resulted in capsule formation at room temperature. In another study, Verma *et al.* fabricated nanofibrous hydrogel by sonicating the encapsulated interfacial capsules made of positively charged CHT and negatively charged polygalacturonic acid.[159] In our bulk mixing studies, the polysaccharide solutions were added from two opposite sides of the well instead of adding one solution over the other. Moreover, we

performed these studies at a higher temperature (60 °C) to decouple the effect of temperature from concentration and viscosity unlike Mendes *et al.* who conducted the studies at room temperature. Altogether, bulk mixing exhibited electrostatic crosslinking, however, it could not result in consistent fibrous complex formation across the three pairs.

2.3.2 Interfacial interaction of oppositely charged polysaccharide solutions promoted micron-scale fiber formation composed of sub-micron fibrils

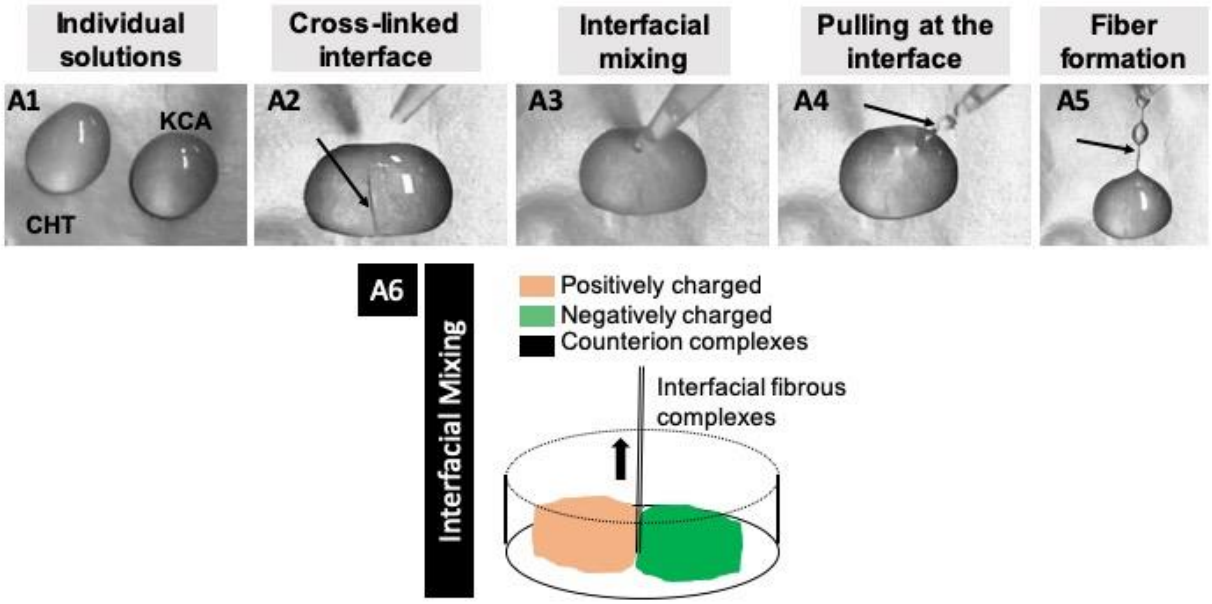

Figure 15: Interfacial fiber formation using a pipet tip. Droplets of CHT and KCA **(A1)** were brought in contact with each other to form electrostatically cross-linked interface **(A2)**. Pipet was used to mix gently at the interface **(A3)** and small amount was pulled away at the interface **(A4)** resulting in an interfacial fiber **(A5). A6** shows schematic representation of interfacial mixing of oppositely charged polysaccharide solutions resulting in formation of fibrous complexes.

Since bulk mixing studies could not facilitate consistent fibrous complex formation between the two oppositely charged polysaccharides, we employed volume displacement pipettes to test the interfacial interaction between the oppositely charged polysaccharides. With a simple

experimental setup, a droplet of CHT and KCA was brought in contact with each other on a piece of parafilm (**Figure 15A1**). The interface (**black arrow, Figure 15A2**) was electrostatically crosslinked on contact between the oppositely charged CHT and KCA. The interface was gently mixed by withdrawing small volume at the interface and releasing it back (**Figure 15A3**). Further, the interface was pulled away from the droplets (**Figure 15A4**), which resulted in formation of interfacial hydrogel fiber (**Figure 15A5**). Schematic presentation of the interfacial interaction Similar findings have been reported where the fibrous complexes were formed between oppositely charged polysaccharides due to the interfacial polyelectrolyte complexation.[169] Further, SEM images of micron-scale single fiber (**Figure 16A, 16B, and 16C**) showed highly aligned submicron-scale fibrils similar to our previous study which employed CHT and methacrylate GG.[131] Moreover, CHT-ALG fiber showed smaller diameter (9.26 ± 1.33 μm) compared to CHT-GG fiber (28.12 ± 2.34 μm) which was smaller than CHT-KCA fiber (44.70 ± 1.17 μm). Further quantification of individual fibril diameter revealed significantly smaller CHT-KCA fibril (0.85 ± 0.42 μm) compared to CHT-ALG (01.14 ± 0.47 μm) and CHT-GG (1.38 ± 0.45 μm) (**Figure 16D**). The difference in mean fibril diameter for all three pairs was in a range of 0.85-1.34 μm, which could arguably be insignificant for cell-fiber interaction.

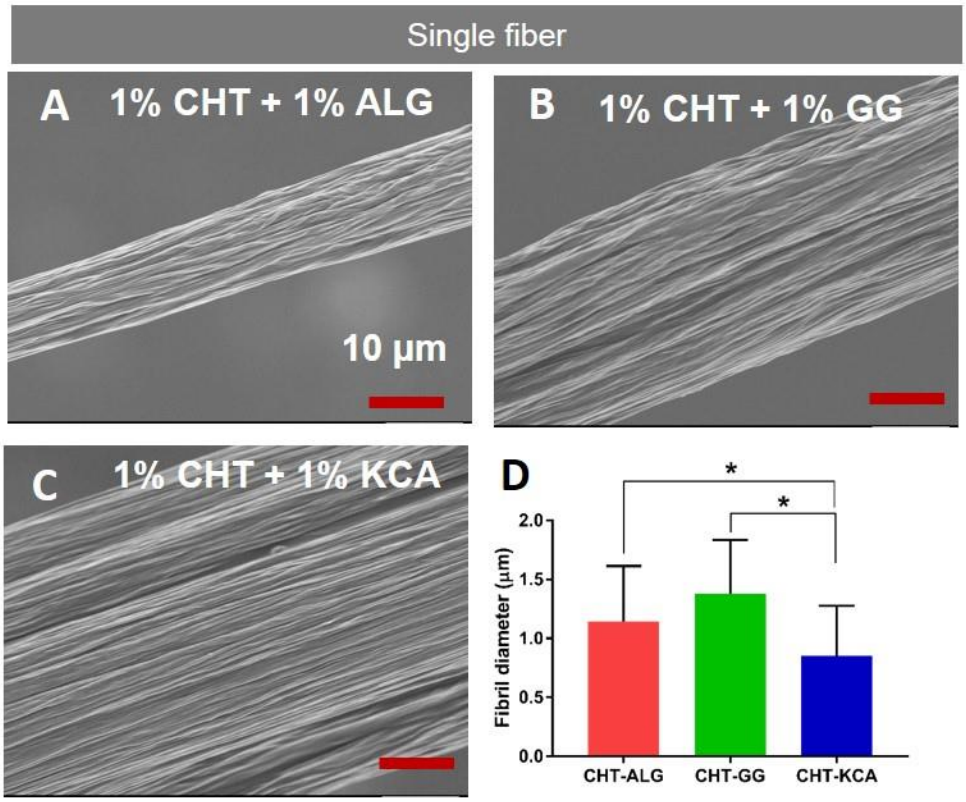

Figure 16: Single fiber surface morphology and fibril diameterSEM images of single fiber of CHT-ALG (**A**), CHT-GG (**B**), and CHT-KCA (**C**), respectively; **D** shows fibril diameter quantification for the three types of scaffolds, n≥10 fibers per image, 3 images per group, * indicates p <0.05 (one-way ANOVA and Tukey's post-hoc

To assess optimum concentration combinations for continuous fibrous complex formation, two oppositely charged polysaccharide solutions were brought in contact with each other at varying concentrations (**Figure 17A**) such that they would form a continuous interface at the center of the well. Oppositely charged polysaccharide chains at such interface facilitated crosslinking through electrostatic interactions. Volumetric pipettes were employed to selectively apply upward pulling force at five points at the interface. This resulted in formation of fibrous complexes for concentrations higher than 0.75% w/v for all three polysaccharide pairs (**Figure 17B1, C1, D1**), whereas 0.5% w/v solutions resulted in the formation of predominantly non-fibrous coacervate complexes (**Figure 17B2, C2, and D2**). These complexes appeared turbid, which was quantified

using absorbance plate reader.[159] Turbidity measurement showed higher absorbance values for ALG and GG (1% w/v), which decreased for concentrations higher than 1 % w/v (**Figure 17B3, C3**). CHT-KCA complexes showed similar trend with increase in absorbance values for concentrations up to 1.25% w/v, which decreased for higher concentrations (**Figure 17D3**). This decrease in turbidity could be due to decreased coacervates formation at higher concentrations.

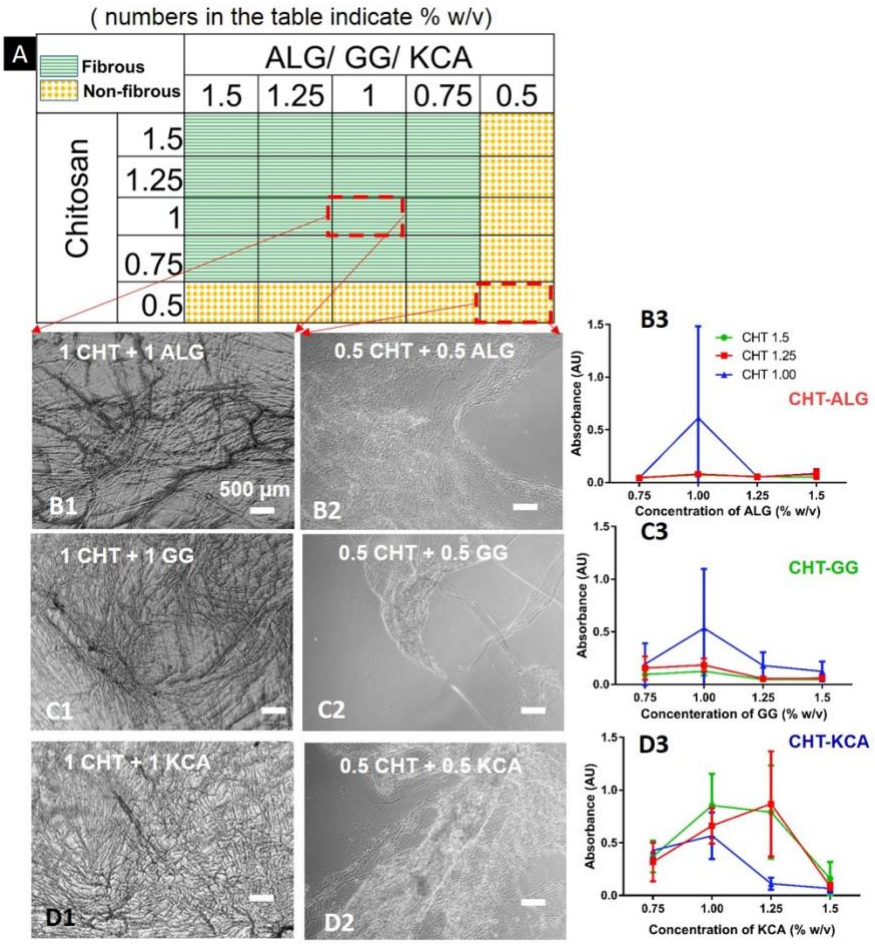

Figure 17 : Interfacial mixing of oppositely charged polysaccharides of various concentration.

A. XY matrix showing effect of polymer concentration on the form of complexes that dominate (fibrous or non-fibrous) after interfacial mixing for all three pairs, CHT+ALG, CHT+GG, and CHT+KCA. **B1-B2, C1-C2, and D1-D2:** Light microscopy images of complexes as a result of interfacial mixing of CHT+ALG, CHT+GG, and CHT+KCA, respectively. 1% w/v combinations showed fibrous complexes whereas 0.5% w/v combinations showed dominant non-fibrous complexes in light microscopy images. **B3, C3, and D3:** Absorbance values at

630nm for turbid complexes as a result of interfacial mixing of various concentration of CHT+ALG, CHT+GG and CHT+KCA, respectively. Combination of all three pairs at 1% w/v of each polysaccharide and that of KCA (1% w/v) with CHT (1.25% or 1.5% w/v) showed relatively higher absorbance values as compared to other concentration and solution pairs.

The underlying principle of interfacial complexation has been reported to depend on 1) the viscosity, which is proportional to polysaccharide concentration and 2) the fiber drawing speed or fiber drawing force at the interface of oppositely charged polysaccharides.[118] It was necessary to keep optimum viscosity or pre-gel viscosity (right before it gels) of the polyionic solutions to facilitate interfacial fiber formation. Ideally, viscosity should not be too low to allow premature diffusion of polyelectrolyte chains into each other while it should not be too high to prevent replenishment with fresh polyelectrolyte as soon as the interfacial fibrous membrane is formed and pulled out as a fiber. Such optimum viscosity is important for continuous formation of fibers.[118, 119] Indeed, Wan *et al.* demonstrated that the fiber formation using a combination of CHT (0.5% w/v) and ALG (2% w/v) resulted in fibers with beads or blobs at regular interval along the fiber as the rate of interaction of the solutions and fiber drawing speed did not match.[120] Similarly, we observed that the fiber formation was not continuous at higher polysaccharide concentrations (*e.g.*, 1.25% and 1.5% w/v KCA) as it was difficult to continuously replenish the interface due to their high viscosity. On the other hand, low concentrations of CHT *(e.g.*, 0.5 and 0.75% w/v) could not form a stable interface and formed turbid non-fibrous coacervates. We conjectured that at low concentrations, the fiber formation could have begun with small fragments of fibers, which could not continue to grow and form long enough fibers to be picked up with a tweezer from the tip of needle. Continuous fiber formation was possible with combinations of concentrations of 1% w/v and higher for all three pairs of polysaccharides. Taken together, these studies demonstrated that

interfacial mixing, optimum viscosity, and polysaccharide concentration are important to enhance continuous formation of fibers at the interface of oppositely charged polysaccharides.

2.3.3 Continuous interfacial motion is required to form micron-scale fibrous complexes within the hydrogels

Based on our results from interfacial mixing studies, three concentrations of CHT (1.5, 1.25, and 1% w/v) with KCA (1% w/v) were chosen to further assess optimum combination of concentrations for continuous and efficient fiber fabrication. A programmable syringe pump was set upright with syringe loaded with one of the concentrations of CHT and the needle was immersed inside KCA solution (1% w/v) on a hotplate set at 60 °C to prevent its gelation (**Figure 18A**). The petri plate was moved as the pump printed CHT solution into KCA solution in the petri plate. This resulted in formation of CHT channels in the KCA solution as shown in **Figure 18B.**

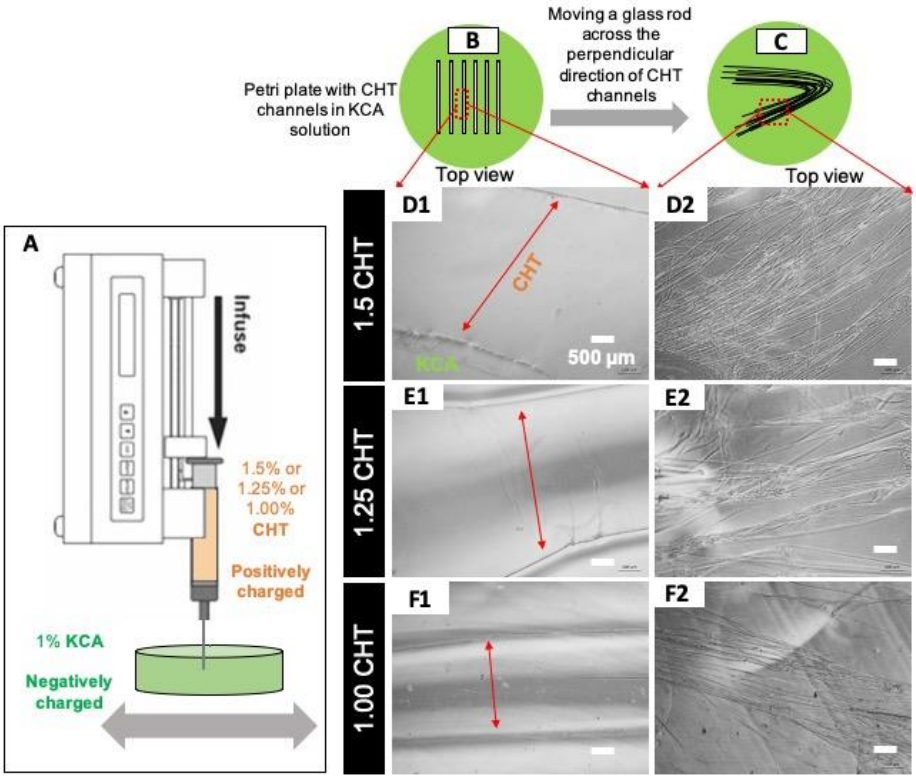

Figure 18: Three-dimensional printing of CHT channels in KCA solution. A. Set up with inverted syringe pump programmed at 50mL/h dispensing either CHT (1, 1.25 or 1.5% w/v) into KCA (1% w/v) solution at 60°C in a manually movable petri plate. **B**. Top view of petri plate after printing CHT channels parallel to each other. **C**. Fiber bundles formed by moving a glass rod across CHT channels in the perpendicular direction; **D1, E1, F1**. As-printed CHT channels (1.5, 1.25 and 1% w/v) in KCA (1% w/v). **D2, E2, F2.** Formation of fiber bundles as transparent fibers with glossy boundaries.

Irrespective of CHT concentration, these channels showed crosslinked membranes at the interface as shown in **Figure 18D1, E1, and F1** and the chitosan in between the two interfaces was found to be un-crosslinked clear solution (no fibers evident) as marked with **red arrows**. Interestingly, when a glass rod was used to streak through the middle of the CHT channels (**Figure 18C),** they formed fibrous complexes (**Figure 18D2, E2, and F2).** The fibrous complexes formed as a result of local motion at the interfacial membrane. This was in line with our observation in interfacial mixing experiments, in which local motion (fiber drawing force) at the interface was provided by continuous pulling at the interface using volumetric pipets. Therefore, in order to form

fibrous complexes, it was necessary to achieve continuous motion at the interface of oppositely charged polysaccharide solutions.

Since optimum interfacial interaction between the two oppositely charged polysaccharides is crucial to form fibers, it was difficult to achieve interfacial fibrous complexes just by printing CHT solution into the KCA solution in a static condition. As a potential solution, Zhu *et al.* have reported pneumatic extrusion-based 3D printing of pre-mixed polyion complex hydrogel using cationic and anionic monomer solutions.[170] They used extrusion and 3D printing technologies to arrange pre-mixed oppositely charged monomers and crosslinked in multiple shapes. However, these bulk-mixed complexes can be further improved by engineering important biophysical features such as multi-scale architecture and anisotropic contact guidance for cells to confer bioactivity to the IPC fibrous hydrogels.

2.3.4 Interfacial mixing chamber facilitates formation of continuous fibers, which were further assembled into centimeter-scale hydrogels with aligned parallel fibers

To assemble fibrous hydrogels with multi-scale fibrous structure and anisotropy, it was important first to facilitate continuous interfacial interaction between oppositely charged polysaccharides. Hence, we developed an assembly of programmable syringe pumps continuously dispensing oppositely charged polysaccharide solutions (kept at 60°C using syringe heat jackets) into an interfacial mixing chamber, where they formed fibers made of fibrils, which were extruded out through a needle. The assembled setup of syringe pumps was operated at room temperature with syringe heat jackets on the syringes. This resulted in continuous interfacial interaction of the oppositely charged solutions (**Figure 19)** and continuous fiber formation at the tip of the needle as

previously reported for our nanocomposite scaffolds of graphene-CHT and GG.[91] As a result of continuous infusion of oppositely charged polysaccharides, the resultant fiber was extruded to the tip of the needle (**Figure 20A**), which was collected manually as shown in **Figure 20B**. In addition to the fibers, non-fibrous blobs were occasionally observed at the tip of the needle (**Figure 20C**) impeding continuous fiber formation. Such blobs were counted for each of the three concentrations of CHT (1, 1.25 and 1.5% w/v) keeping KCA concentration constant (1% w/v). CHT and KCA solutions (1% w/v each) showed least number of blob formation and higher average number of fibers formed with 10 mL of each polysaccharide solutions (**Figure 20D**). Blob formation was found to be inversely proportional to the fiber formation. Specifically, relatively higher blob formation for 1.5% CHT could be due to slower replenishment of fresh CHT for KCA due to their higher viscosities resulting in lower interfacial interaction and eventually, resulting in blobs at the tip of the needle.

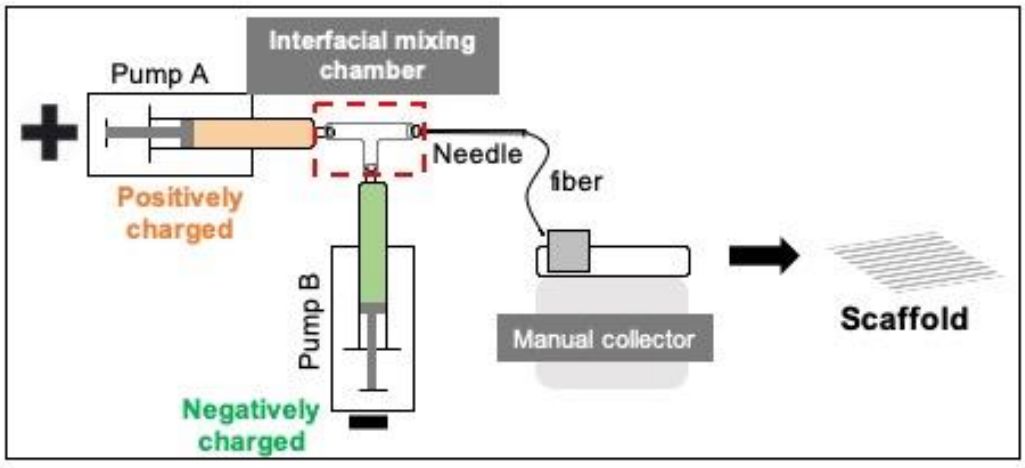

Figure 19: Interfacial mixing chamber with manual collector. Set up for fiber fabrication using two syringe pumps, interfacial mixing chamber and manual collector to obtain fibrous hydrogels.

The extruded fibers were collected manually and aligned parallel to each other to obtain anisotropic fibrous hydrogels (dried hydrogels, **Figure 22C1**). Fibrous surface of the dried hydrogels was confirmed using SEM (**Figure 22C2**). These fibrous hydrogel surface appeared as a union of multiple micron-scale fibers made of submicron-scale fibrils similar to CHT-ALG IPC fibers reported by Wan *et al.* exhibiting micron- and submicron-scale parallel features in the SEM images.[120] Additionally, The developed fabrication platform also enabled us to vary hydrogels

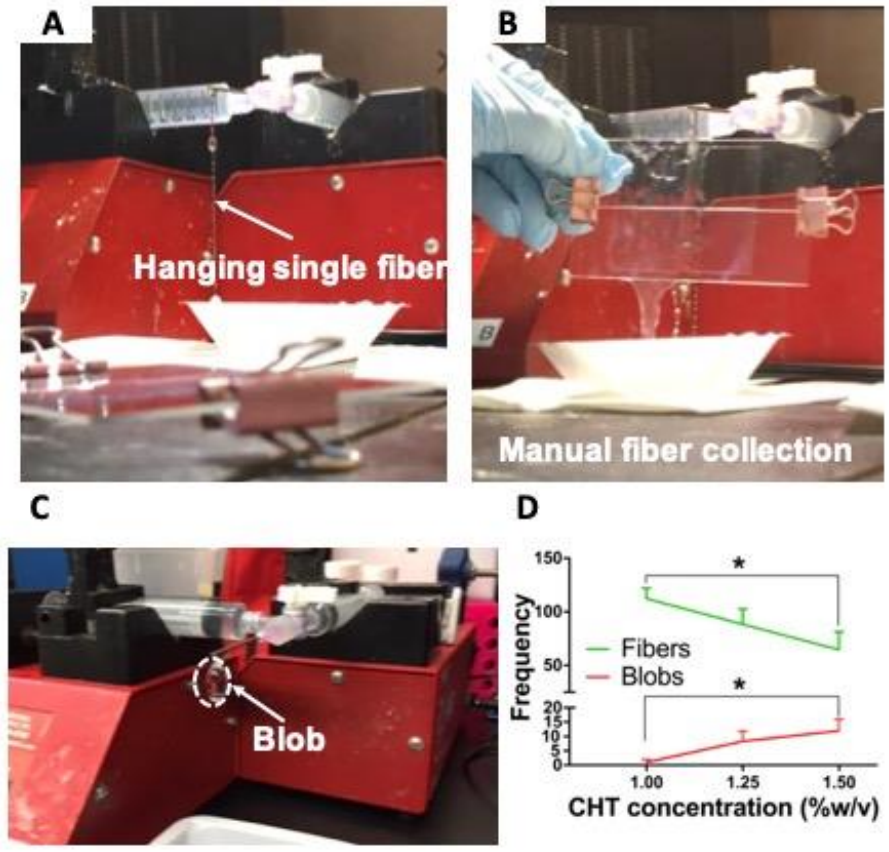

Figure 20: Continuous fiber formation process set-up and blob formationA. A single fiber made of CHT and KCA hanging at the tip of a hypodermic needle; **B**. Manual collection of multiple fibers to obtain a fibrous hydrogels on a glass slide collector; **C**. A representative picture of blob formation (white arrow) using CHT (1.5% w/v) and KCA (1% w/v); **D**. Quantitative comparison of fibers and blobs formed when 1.5, 1.25 or 1% CHT was used with 1% KCA (n=3); * indicates $p < 0.05$ (One-way ANOVA and Tukey's post-hoc test).

microarchitecture by arranging a layer of fibers perpendicular to the other layer, resulting in a crisscross fibrous arrangement (**Figure 21**).

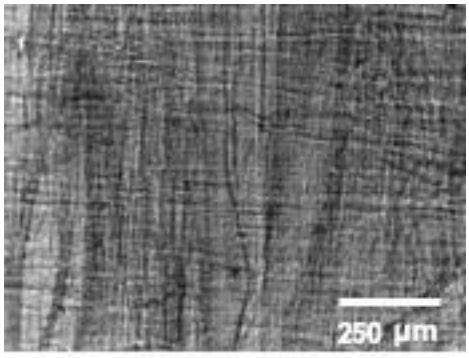

Figure 21: Criss-cross arrangement of fibers achieved by perpendicular collection of the fibers

Notably, the above hydrogel fabrication parameters optimized for CHT and KCA pair were easily adapted to fabricate CHT-ALG and CHT-GG hydrogels as well. To compare effects of differences in charge imparting groups (carboxylate *vs.* sulfate) as well as the magnitude of zeta potential on the resultant hydrogel properties, we fabricated CHT-KCA, CHT-ALG and CHT-GG

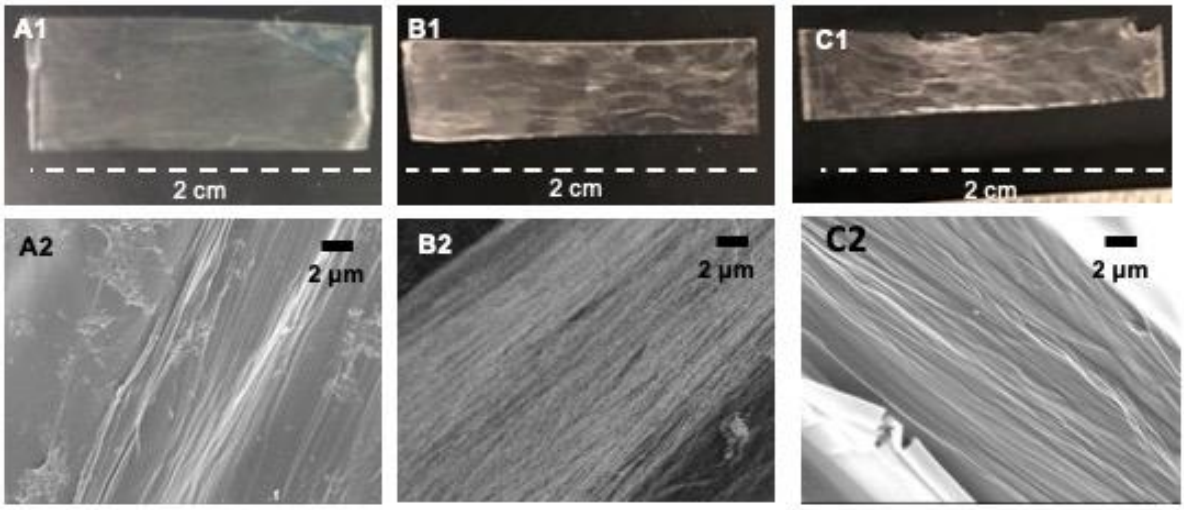

Figure 22: Fibrous hydrogel appearance and surface morphology Photographic image of CHT-ALG (**A1**), CHT-GG (**B1**), and CHT-KCA (**C1**) hydrogels. **A2**, **B2**, and **C2** show SEM image fibrous surface of corresponding hydrogels in the same order; scale bar represents 2 µm

hydrogels at concentrations of 1 % w/v. Air dried CHT-ALG and CHT-GG hydrogels showed similar flexible film-like morphology as shown in **Figure 22A1 and 22B1,** respectively.

Moreover, SEM images of CHT-ALG and CHT-GG showed parallel alignment of submicron fibrils and micro-scale fibers throughout the hydrogels (**Figure 22A2 and 22B2**, respectively). Collectively, the three types of hydrogels showed multi-scale microarchitecture with parallel alignment of fibers.

2.3.5 Automated fiber collector assembly provided more control over process parameters and enhanced precision for collection and orientation of fibers

Fiber collection and alignment using manual collection method is dependent on the familiarity and practice of the user. Therefore, to ensure user-independent control over fiber collection and alignment, we further designed an assembly of gear motor mounted on a programmable stage (**Figure 23A1**). Temperature was controlled using a constant temperature incubator. The circular motion of the shaft of gear motor (**Figure 23B1,** white circular arrowhead) provided repeated encounters with the hanging fibers at the tip of the needle. Programmable stage (**Figure 23B1,** white triangular arrow) ensured collection of fibers next to each other and parallel to each other also providing the flexibility to achieve a single layer, bilayer or multilayer hydrogels due to ability to move the stage in horizontal direction with mounted coverslip (on which fibers are collected). Needle, coverslip and the rotating shaft are shown in **Figure 23B2** whereas **Figure**

23A2 demonstrates fiber hanging from the needle with the rotating collector in the background \ and fiber collected on the rotating collector (**Figure 23A3**).

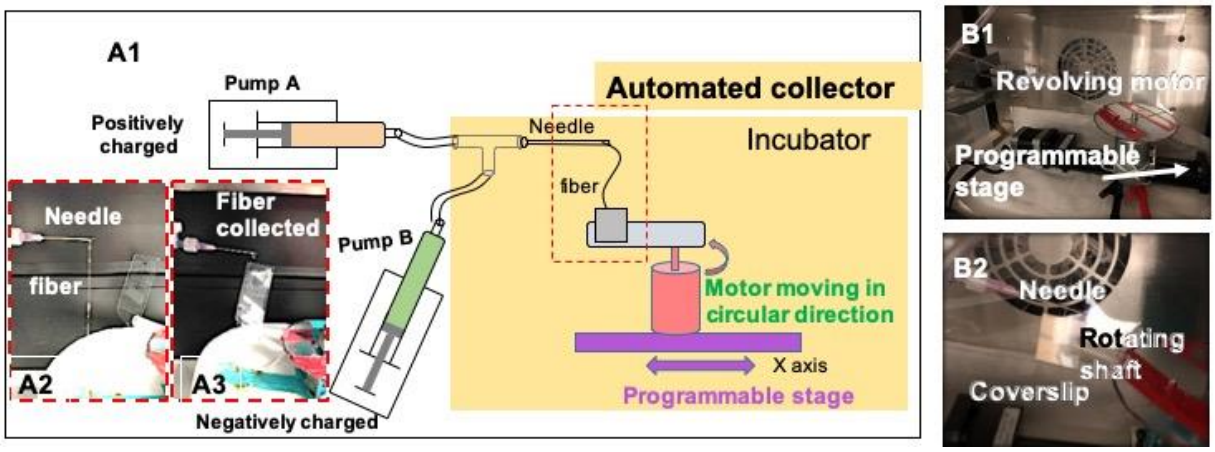

Figure 23: Automatic collection of anisotropic fibrous hydrogels.A1. A schematic of the set up for automated collection of fibers in a temperature-controlled incubator using two types of motors: one moving in the circular direction to collect and cut fibers on a glass slide while the other (programmable stage) moving along the horizontal axis to arrange fibers parallel to each other; Red-dotted outline pictures exhibit corresponding area in the schematic (red dotted outline) before **(A2)** and after **(A3) c**ollection of the fiber. **B1.** Assembly with both the motors and fiber dispensing needle in the controlled temperature incubator; **B2.** Coverslip near fiber dispensing needle.

We further optimized the synchronization of three programmable components in the assembly: 1) two syringe pumps, 2) programmable stage, and 3) revolving motor. The revolving motor was adjusted based on the rate of fiber formation for each scenario and therefore, it was excluded from optimization studies. Infusion rate of both the syringe pumps determines the dispensing rate of oppositely charged polysaccharides, which was kept the same for both the pumps to simplify optimization efforts. Four different infusion rates of syringe pumps were considered for the optimization, namely, 25, 40, 50, and 75 mL/h. The efficiency of fiber formation was measured as the number of fibers per minute (fibers/min) and number of fibers per unit volume (fibers/mL). Although we did not find any statistical significance in the linear correlation between concentrations of polysaccharides and fibers/minute or fibers/mL, the overall trend showed

significantly higher number of fibers/minute when the pump rate was increased from 25 mL/h to 40 mL/h (pink line, **Figure 24A**). However, there was a non-significant increase in fibers/minute beyond 40 mL/h. Further, we analyzed number of fibers/mL with increasing rate of pumps. While pump rates of 25 and 40 mL/h showed similar fibers per mL of raw materials, higher pump rates of 50 mL/h and 75 mL/h showed comparatively lower number of fibers/mL (purple line, **Figure 24A**). Taken together, the results of fibers/min and fibers/mL, we selected 50mL/h as optimum pump rate for further studies. We then varied programmable stage speed from 25, 50 or 100 μm/sec to determine optimum speed to obtain uniform distribution of fibers aligned parallel. We then compared the number of fibers per unit area (defined as 'fiber distribution density') and total hydrogel scaffold size per unit volume of polysaccharides for three different stage speeds to decide the optimum stage speed. Fiber distribution density significantly reduced when the stage speed was increased from 25 to 50 or 100 μm/sec (orange line, **Figure 24B**). This is expected since with faster moving stage, the collected fibers were distributed over a larger area. Total hydrogel scaffold size per mL of polysaccharides showed marginal increase when the stage speed was changed from 25 to 50 μm/sec; however, 100 μm/sec showed significantly larger scaffold area compared to 25 μm/sec (brown line, **Figure 24B**). This was further confirmed through thickness measurement of these hydrogels, which indicated an inverse linear correlation between stage speed and thickness (**Figure 24C).** Faster stage speed prevented deposition of subsequent fiber upon each other and decreased the thickness of the hydrogels as anticipated. Thus, the stage speed altered fiber distribution density. Fiber distribution density could impact packing density/unit area and structure reinforcement, thus affecting the mechanical properties of the hydrogel. Therefore, hydrogels prepared at different stage speeds were characterized for their tensile mechanical properties. However, hydrogels exhibited no statistically significant differences in the UTS or percentage

elongation between three stage speeds (**Figure 24D**). These results indicated that the inherent mechanical properties of the single hydrogel fiber dominate the overall hydrogel mechanical properties irrespective of fiber collection parameters. Therefore, stage speed of 50 µm/sec was considered optimum for assembling multi-scale fibrous hydrogels.

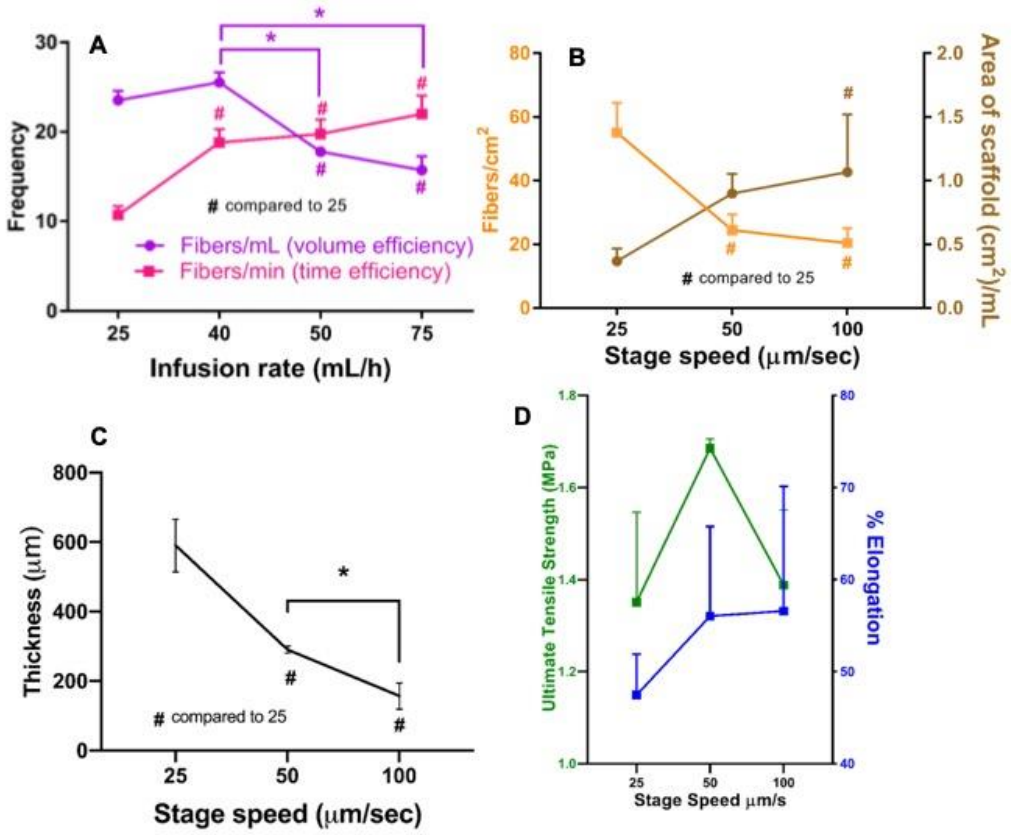

Figure 24: Effect of variable fabrication parameters on fibrous hydrogel properties.A. Effect of pump speed on formation of fibers per minute and fiber formation per milliliter; **B**. Effect of stage speed on fiber distribution density (Fibers/cm2) and scaffold area covered per unit volume (cm2/mL), respectively; C. Thickness of hydrated CHT-GG hydrogels prepared at various stage speeds. **D.** Ultimate tensile strength (right y-axis) and percentage elongation (left y-axis) for CHT-GG hydrogels prepared at various stage speeds. * and # indicates $p < 0.05$ (one-way ANOVA and Tukey's post-hoc test).

We then compared fiber alignment within the hydrogels prepared with manual collector with those collected with the automated collector. Light microscopy images of hydrogels prepared with manual collector and automated collector were used to quantitate the degree of fiber

alignment. This was accomplished by using orientation J plugin in FIJI. The color survey image of hydrogels prepared using automated collector (**Figure 25B**) showed more consistency in parallel fiber alignment compared to that of manual collector (**Figure 25A**), which was evident by the presence of more predominant red color in the hydrogel prepared using automated collector. Moreover, hydrogels prepared using manual and automated collectors varied in fiber alignment depending on the user precision. Therefore, hydrogels were prepared by two users independently using both the manual and automated collectors and they were quantified for directionality using FIJI. Hydrogels prepared with manual collector showed larger user error compared with hydrogels prepared with automated collector (shaded region, **Figure 25C**). Moreover, comparison of standard deviation in fiber orientation showed greater disparities between the two users when manual collector was used compared to the automated collector (inset bar graphs, **Figure 25C**). Thus, automated collector provided more control over the fiber alignment independent of the user variation.

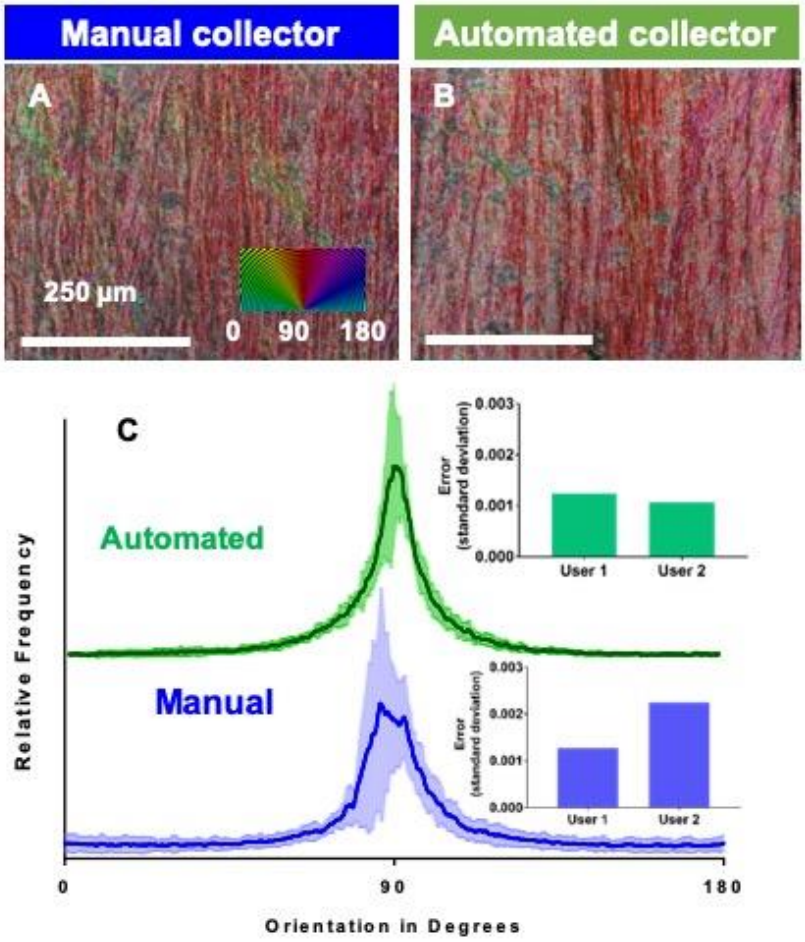

Figure 25: Comparison of fibrous hydrogels collected with manual and automated collectors for their orientation accuracy. A-B. Representative color survey corresponding to the fiber orientation angle output images from FIJI of light microscopy images from manual and automated collector hydrogels, respectively; red color indicates parallel fibers. **C**. Histogram showing distribution of angles from hydrogels made by at least two users independently using either manual (blue) and automated (green) collector; 90º refers to the parallel alignment of fibers. The inset bar graphs show standard deviation for each user from the histograms for corresponding methods. Note higher differences in standard deviation for manual collector (blue bar graphs in the inset).

Many of the previously reported approaches to obtain hydrogels from collected interfacial fibers have focused mostly on pre-mixed bioink formation followed by extrusion or using rotary collector.[130, 170] These are some other efficient approaches to form fibers and also incorporate biochemical entities such as small drugs or proteins that are soluble in either of the two solutions. Lu *et al.* [171] and Yim *et al.* [130] reported polyelectrolyte hydrogel fiber collectors based on a

rotating wheel on the top a continuously interacting oppositely charged solutions to collect the fibers. Specifically, they mixed alginate with cells prior to pulling of the fibers, which resulted in high cell encapsulation efficiency of 88.38 ± 8%.[130] As shown later, our platform is amenable to encapsulation of a variety of cargo other than cells such as particle suspensions, small drug molecules and proteins. Potential advantage of our platform could be enhancement of electrostatic charge-based interaction among the particles (or cells) with the polysaccharides when infused at constant rate through syringe and needle instead of particles loaded by simple physical entrapment. In summary, we reported an innovative collector controlled by two motors working in coordination with the frequency of fiber formation to precisely collect and orient hydrogel fibers in the form of desired multi-scale anisotropic architecture.

2.3.6 Fibrous hydrogels show cytocompatibility and cell adhesion

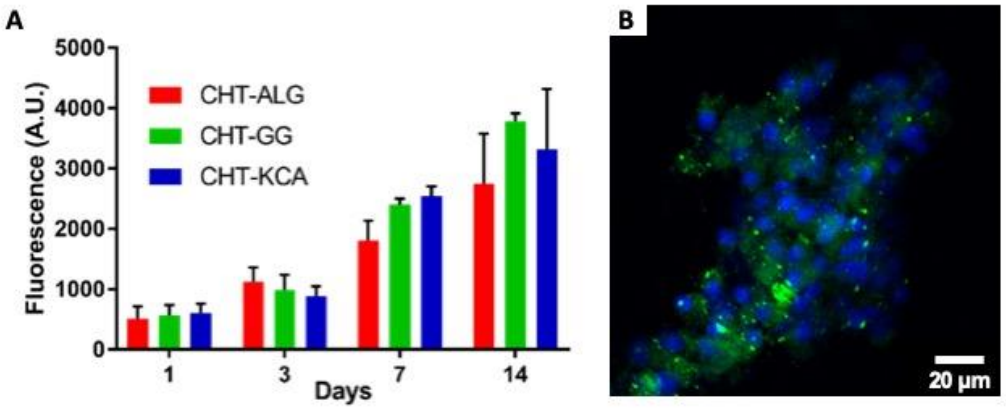

Figure 26: Cytocompatibility of fibrous hydrogels A. Cytocompatibility of cells seeded on hydrogels at days 1, 3, 7, and 14, measured by metabolic activity alamarBlue assay. There was no statistical significance between hydrogel conditions at the same time point; **B.** Cytoskeletal images of MC3T3- mouse preosteoblast cells seeded and cultured for 14 days on CHT-KCA hydrogels; actin: green and nuclei: blue.

Polysaccharides have been used in pharmaceutical and biomedical research as compatible

materials for host cells. In addition to cytocompatibility, differences in cell-material interaction may impact metabolic activity and therefore, proliferation of mouse pre-osteoblast cells was assessed using alamarBlue® assay. The three types of hydrogels showed no statistically significant differences in their metabolic activity **(Figure 26A)**. Moreover, actin and nucleus staining **(Figure 26B)** of mouse pre-osteoblasts (MC3T3) cells after 14 days of culture demonstrated good cell-adhesion on CHT-KCA hydrogels. These cytocompatibility and cell adhesion findings are in line with our previously reported graphene-CHT-GG hydrogels and other similar studies done using CHT-ALG.[91, 108, 163]

2.3.7 Fibrous hydrogels show tough and elastic mechanical properties

Most of the mechanical testing on IPC fibers has been done on the dried hydrogel scaffolds or individual fibers due to the technical challenge of mounting hydrated fibers on the grips; however, hydrated form is more relevant for biomedical applications.[110] Hence, we tested tensile mechanical properties of the hydrogels in their hydrated form. The CHT-GG showed significantly higher Young's modulus and significantly lower percentage elongation than CHT-ALG and CHT-KCA (**Figure 27A and 27B**). The ultimate tensile strength (UTS) followed the same trend as Young's modulus (**Figure 27C)**. However, all three hydrogels showed similar toughness values (**Figure 27D**). These results suggest that CHT-GG was the stiffest of all three materials with the highest UTS and elastic modulus and the lowest percentage elongation. This suggests that CHT-GG dissipated a large amount of energy for a relatively small extension and underwent a quick and sharp fracture. CHT-KCA and CHT-ALG, on the other hand, were ductile and stretchable as they dissipated energy over much larger extensions giving rise to a much lower elastic modulus and UTS, along with the 600-700% elongation. The toughness was not

significantly different between the three hydrogels, suggesting that they each withstand the same amount of tensile stress, but possibly through different mechanisms. Differences observed in CHT-GG compared to CHT-ALG and CHT-KCA could be due to the difference in their electrostatic charge densities (**Figure 12**). While ALG and KCA had nearly same magnitude of zeta potential as CHT, GG had almost 50% reduced zeta potential than CHT. This may allow a stronger cross-linking at the interface between CHT and GG due to more of GG chains interacting with each of the CHT chains, thereby, resulting in an overall tough mechanical property.

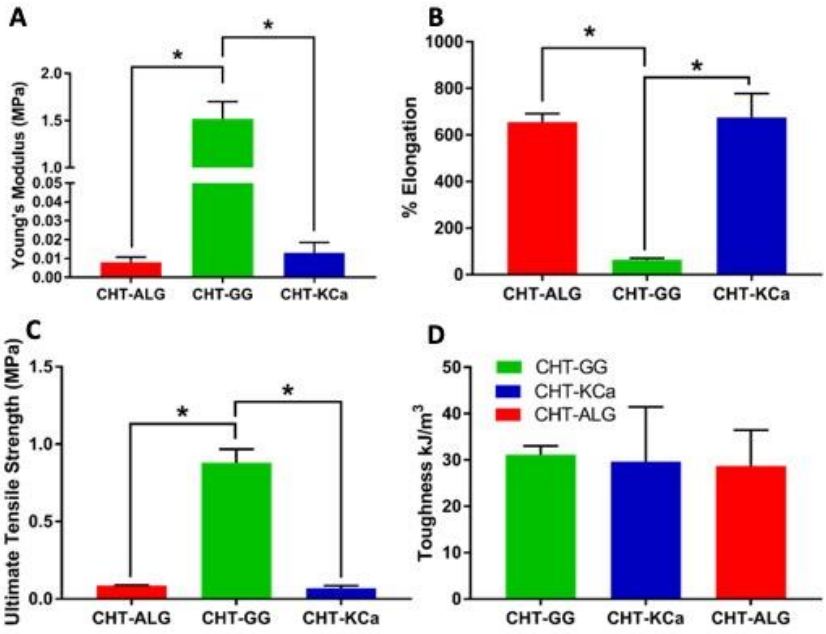

Figure 27: Uniaxial tensile mechanical properties for all three pairs of hydrogels. Mechanical properties of CHT-GG, CHT-KCA, and CHT-ALG hydrogels showing Young's modulus **(A),** Percentage elongation **(B),** Ultimate tensile strength **(C),** and Toughness comparison **(D)** n=3.

2.3.8 Fibrous hydrogel fabrication platform enabled single-step encapsulation of nanoparticles or small molecules to further modulate hydrogel properties

IPC fibers have been utilized as a delivery vehicle for small molecules, particles and cells through encapsulation.[172, 173] Entrapment inside the interfacial fibers has been used as a simple way to load moieties into the IPC fibers with main goal to control and sustain the release. Similarly, immobilization of insoluble nanoparticles can also be achieved to form composites at nanoscale.[91] We have previously reported a similar entrapment of graphene sheets to form nanocomposite fibrous hydrogels of CHT-GG, which enhanced UTS and toughness of the hydrogel without altering their elastic modulus.[91] Moreover, this strategy not only evaded toxicity of the graphene but also conferred electrical conductivity to the IPC fibers due to the graphene sheets, which enhanced formation of myotubes from myoblasts seeded on the composite hydrogels.[91]

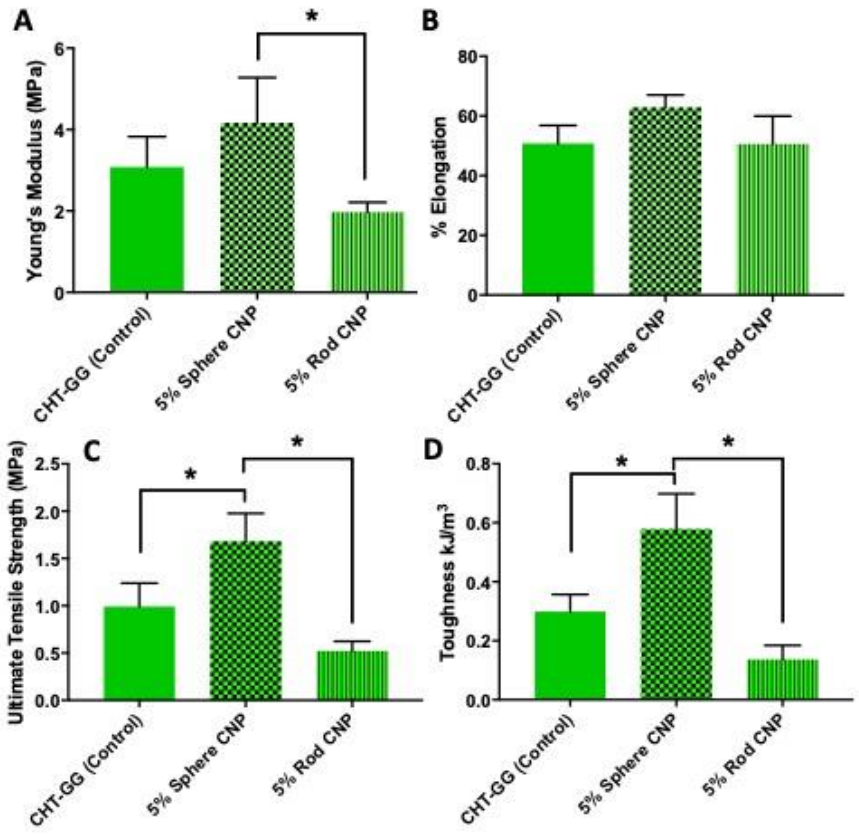

Figure 28 : Uniaxial tensile mechanical properties for CNP-CHT-GG hydrogels. Mechanical properties of CHT-GG hydrogels encapsulating sphere- or rod-shaped CNPS (5% w/v) (referred as CNP-CHT-GG), showing Young's modulus **(A),** Percentage elongation **(B),** Ultimate tensile strength **(C),** and Toughness comparison **(D)** n=3; * $p<0.05$; One-way Analysis of Variance and Tukey's post-hoc test.

In this study, we exploited our platform technology for IPC-based multiscale hydrogel fabrication to entrap cerium oxide nanoparticles (CNPs). CNPs have gained interest as dynamic bioactive nanomaterial for their shape-specific activity as well as their redox activity to alter cell phenotypes.[174] In the scope of this study, we studied shape-specific effect of CNPs on the mechanical properties of the hydrogels. The sphere-CNPs and rod-CNPs (each 5% w/v) were homogenized into CHT solution prior to the interfacial mixing of CHT and GG. Indeed, the sphere-CNP-CHT-GG showed increased Young's modulus compared to rod-CNP-CHT-GG (**Figure 28A).** However, percentage elongation of CNP-CHT-GG remained unchanged as compared to CHT-GG without CNPs (**Figure 28B**). UTS (**Figure 28C**) and toughness (**Figure 28D**) showed

significantly higher values for sphere-CNP-CHT-GG compared to CHT-GG and rod-CNP-CHT-GG, indicating greater reinforcement caused by sphere-CNPs. These findings are similar to those in our graphene-CHT-GG study.[91] In contrast, rod-CNP-CHT-GG showed reduction in UTS and toughness, compared to the sphere-CNP-CHT-GG. In most encapsulation approaches using IPC, both electrostatic and physical entrapment collectively contribute to the loading of insoluble moieties such as CNPs to an extent. Sphere- and rod-CNPs may have interacted with CHT and GG differently; this could be the reason for their different tensile properties. Similarly, Zou *et al.* [175] and Razdan *et al.* [176] have demonstrated entrapment of graphene sheets and carbon nanotubes, respectively. Razdan *et al.* compared mechanical properties of IPC fibers made with single-walled carbon nanotubes (SWNTs) with that of multi-walled carbon nanotubes (MWNTs) dispersed in polystyrene sulfonate (PSS) and electrostatically crosslinked with polydiallyldimethylammonium chloride. The MWNTs group showed 3-4 times greater tensile strength and Young's modulus compared to SWNTs group, which was attributed to higher level of interaction of MWNTs with PSS.[176]

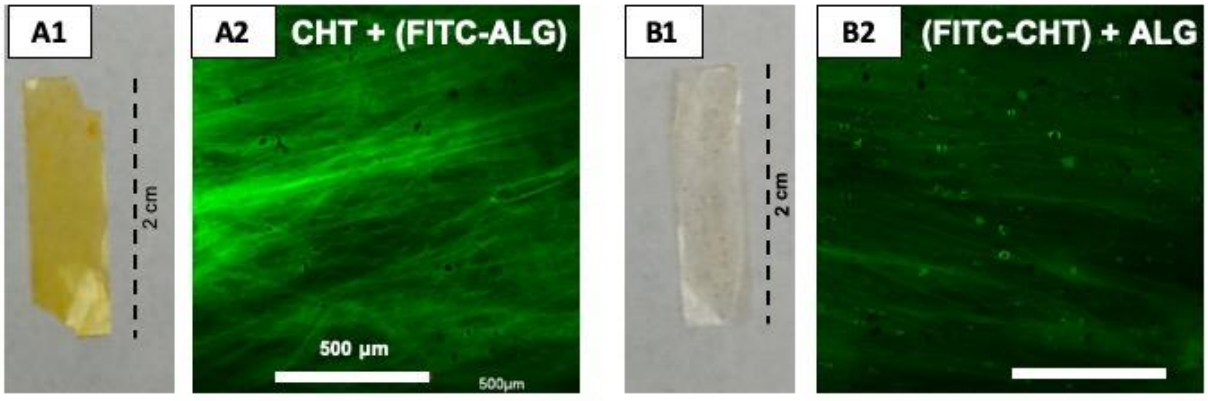

Figure 29 : CHT-ALG with FITC A1. Photographic image of CHT + (FITC-ALG) hydrogels; **A2.** Confocal image of CHT+ (FITC-ALG) scaffold with green fluorescence of FITC; **B1.** Photographic image of (FITC-CHT) + ALG hydrogels; **B2.** Confocal image of (FITC-CHT) + ALG hydrogels; white scale bars indicate 500µm.

Similar to nanoparticles, small molecules have also been incorporated in the IPC fibers.[110] We incorporated fluorescein isothiocyanate (FITC) as a model small molecule to demonstrate small molecule loading capacity of our fiber fabrication platform. We used FITC as a model small molecule to be incorporated into and CHT-ALG interfacial fibrous hydrogels in order to demonstrate their potential as a small molecule carrier. FITC was dissolved either in CHT or ALG solutions prior to fiber formation. FITC incorporated into ALG (FITC-ALG) prior to CHT-ALG fiber formation (CHT + FITC-ALG, **Figure 29A1)** showed more uniform distribution of FITC across the hydrogel compared to FITC incorporated into CHT (FITC-CHT + ALG, **(Figure 29B1**). Confocal images of CHT + FITC-ALG (**Figure 29A2**) further validated the uniform distribution and higher loading of FITC when FITC was added in ALG instead of CHT (FITC-CHT + ALG, **Figure 29B2**). These studies demonstrated the flexibility of our platform technology to encapsulate or entrap nanoparticles and small molecules inside IPC-based multi-scale hydrogels. Overall, we have developed flexible and robust automated platform for fabrication of IPC-based anisotropic fibrous hydrogels with multi-scale hierarchy, high tensile strength (MPa) and ability to incorporate nanoparticles or small molecules in the hydrogels for additional multifunctionality.

2.4 SUMMARY

In this chapter, we demonstrated that bulk mixing of oppositely charged polysaccharide pairs failed to produce continuous interfacial fibers while interfacial mixing of the same pairs showed greater extent of fiber formation. Combination of CHT (1% w/v) and KCA (1% w/v) showed more efficient interfacial fiber formation using the interfacial mixing chamber. To further

improve fiber alignment accuracy and efficiency, and reproducibility of fiber formation in a user-independent manner, we optimized and developed an automated fiber collection method. The automated fiber collection method reduced user-dependent variation and provided robustness to hydrogel fabrication process. CHT-GG hydrogels showed significantly higher UTS, higher Young's modulus, and significantly lower percentage elongation without significant differences in toughness compared to CHT-ALG and CHT-KCA. Interestingly, encapsulation of sphere-shaped CNPs enhanced UTS, Young's modulus and toughness of CHT-GG without affecting elongation while rod-shaped CNPs exhibited opposite effects. Altogether, we successfully developed a versatile platform technology to fabricate IPC-based hydrogels with anisotropic fibrous architectures (parallel *vs.* perpendicular) with additional ability to encapsulate small molecules and nanoparticles.

3 COLLAGEN-INSPIRED MINERAL-HYDROGEL NANOCOMPOSITE SCAFFOLDS SHOW PROMISE AS GROWTH-FACTOR-FREE BONE GRAFT SUBSTITUTES IN MICE CALVARIA DEFECT

[Patel A, Zaky S, Beniash E, Schoedel K, Li H, Sfeir C, Sant V, Sant, S]

ready for submission

3.1 BACKGROUND

Trauma due to sports injuries, road accidents, and combat lead to loss of bone beyond the capacity of body to heal. Bone also is lost to cancer. After blood, bone grafts are the second most commonly transplanted materials.[1] Synthetic bone grafts made of metal and ceramics are clinically approved and are employed with the primary purpose of providing mechanical support to the damaged tissue. The majority of synthetic grafts are bio-inert with some of ceramic materials being bioactive or bio-absorbable, which get integrated with the healing bone.[11] Synthetic grafts intended to serve temporary function such as non-resorbable screws require surgery for their removal or else they stay in the body forever. Both resorbable and non-resorbable metal implants often lead to fibrotic tissue formation around their surface due to delayed bone healing in the area.[16] Autografts (bone tissue harvested from the host) and allografts (cadaveric bone from bone bank) also are clinically approved surgical options. Autografts are near gold standard option

for grafting; however, the surgery and harvesting of grafts is associated with complications such as infections, chronic pain and cosmetic defects in 8-20% of cases.[8, 9]

Bone graft substitutes that locally deliver highly potent growth factors such as bone morphogenic protein-2 (BMP2) exhibit osteogenic bioactivity such as osteoconduction (facilitation of new bone growth produced by surrounding mature bone) and osteoinductive (recruitment and differentiation of immature cells and further bone formation by them). It should be noted that these bone grafts are approved only for spinal fusion indications but due to their appealing clinical outcome of bone regeneration and limited number of approved Food and Drug Administration (FDA) indications other than spinal fusion have led to their extensive "off-label" use such as craniofacial bone injuries and cervical spine surgeries.[22, 177] These substitute bone grafts are mostly composed of the two main components: a highly potent growth factor such as recombinant human bone morphogenic protein-2 (rhBMP2) and its carrier material, which is mostly deemed bio-inert. The use of rhBMP2 makes it highly efficacious, however, it is not specific for bone tissue and has effects on cellular processes and it exhibits dose-dependent effect and therefore, its continuous dose should be maintained for optimum efficacy.[178-180] In addition, as rhBMP2 is highly soluble in the body fluids found at injury site, if used alone without any carrier material, it disperses instantly after implantation, thereby, either increasing the risk of side effect or failing to induce bone growth due to its degradation by proteases and subsequent inactivation in 20 to 30 minutes.[23, 24] Relatively less potent bioactive alternatives include undefined osteogenic agent mixtures such as demineralized bone matrix (DBM) or bone putty [181, 182] and platelet concentrates [183] which comprises of many endogenous growth factors including BMP2 and platelet-rich plasma are under development since more than two decades.

However, batch to batch variability is a tough challenge to overcome due to their biological source.[184]

Limitations of clinically used bone graft options have provided opportunities to orthopedic industry for the development of innovative technologies for osteogenic bioactivity. rhBMP2 remains as an essential ingredient in bone graft substitutes for the clinical success of osteoinductive bone graft substitutes, however, its optimum carrier is yet to be figured out. Current clinically used products use absorbable collagen sponges for local delivery which showed no osteogenic bioactivity and presented safety and precision issues due to squeezing of the BMP2 out of the sponge due to soft tissue compression in nonhuman primate studies.[185] Majority of experimental bioinert as well as osteoconductive organic-inorganic mixture carriers employ hydroxyapatite (HA)[186] or other calcium phosphate-based mineral blends as inorganic phase along with polyester-based polymers such as poly (ε-caprolactone) (PCL)[187] as organic phase. However, these mineral-polymer composites often form physical mixture without molecular interaction between organic matrix and minerals which is considered to be the most important feature of natural bone mineralization process, thereby imparting no osteoinductive bioactivity. On the other hand, there are a few experimental approaches which have aimed to design osteoinductive carriers such as silicate nanoparticles,[188] bacterial cellulose,[189] and biphasic calcium phosphate.[190] At best, bioactivity of these materials has been demonstrated to induce osteogenic properties due to the degradation products of the composite scaffolds.[188, 191] Therefore, selection of the osteogenic raw material is essential to impart bioactivity to the carrier biomaterial.

Ideal biomaterial properties should benchmark with biomimetic molecular interactions and structural hierarchy of collagen fibrils, although with added osteogenic bioactivity from the biomaterial. In the natural bone development, collagen is one of the main components of bone-

ECM, which induces nucleation of HA crystals majorly due to its nanoscale architecture and electrostatic charges from the positive net charge close to the C-terminal end of the collagen molecules.[192] Natural bone development process involves deposition of inorganic minerals in an organic matrix, forming inorganic-organic nanocomposites. The mineral deposition is controlled largely by the organic components of ECM which includes cells, collagen and other proteins, from which collagen comprises 85-90%.[133] Although the mechanisms of mineralization are not fully understood, mineral sequestration, nucleation and its growth have been found to constitute three key steps in the process.[133, 135, 136] Electrostatic and hydrophobic interactions along with nanoscale arrangement of collagen promotes sequestration and nucleation whereas collagen organization acts as an organic template to guide mineral deposition.[133, 137]

Such collagen-mineral interaction could be incorporated through the use of electrostatic interaction of the biomaterial with simulated body fluid. Indeed, electrostatic charges and charge-imparting groups (carboxylate vs. sulfate) have been proven as key determinants in sequestration of minerals.[133] To facilitate such matrix-mineral interactions, polysaccharides are one such class of polymers, which have been explored for its potential for promoting mineralization. Polysaccharides control and guide mineral deposition in marine creatures and crustaceous animals. Chitosan [69, 70] and other polysaccharides such as alginate, [71] gellan gum, [72, 73] etc. either alone or in combination with other polysaccharides have shown mineralization potential, which makes them excellent candidates as organic template for mineral deposition.[75] Therefore, we employed chitosan as the common cationic polysaccharide and three different anionic polysaccharides with carboxylate (alginate and gellan gum) and sulfate (carrageenan) functional groups to generate three types of fibrous hydrogel scaffolds. Chitosan (CHT) was chosen as the common positive polyelectrolyte for its proven role in mineralization process in various sea

creatures such as shrimp [75] whereas negatively charged polyelectrolyte were selected based on their negative charge imparting functional group found in the components of natural ECM. Specifically, alginate (ALG) and gellan gum (GG) with carboxylate (COO^-) as negative charge imparting group have been chosen for its similarity with hyaluronic acid in natural cartilage ECM. Similarly, kappa carrageenan (KCA) was chosen for its sulfate (SO_4^{2-}) group and helical coil formation of its chains.[193] Sulfate group is common charge imparting group found in glycosaminoglycan and chondroitin sulfate in natural bone and cartilage ECM.[194] Additionally, natural origin and extensive use of these polysaccharides in food industry alleviate concerns related to biocompatibility and biodegradation.

Due to large chains, most polysaccharides can form hydrogels, although with limited multi-scale hierarchical features to incorporate structural features similar to bone-ECM. These hydrogels offer advantages to preserve growth factors to facilitate their sustained activation.[103] Interfacial polyionic complex (IPC) fibers, formed due to the electrostatic interaction at the interface of oppositely charged polymers, [110] offer great opportunity to design bone-ECM mimetic materials.

3.2 MATERIALS AND METHODS

3.2.1 Materials

Gellan gum (GG) (G1910), alginic acid (ALG) (A0682), chitosan (CHT) (C3646), and acetic acid (695092) were all purchased from Sigma-Aldrich Co. (St. Louis, MO). The kappa carrageenan (KCA) (C41070) was obtained from Research Products International (Mt. Prospect,

IL). Cell culture supplies including Dulbecco's minimum essential medium alpha (DMEM) and Dulbecco's phosphate-buffered saline (DPBS) were purchased from Mediatech Inc. (Manassas, VA) or Corning Inc. (Corning, NY) unless otherwise specified. Fetal bovine serum (FBS) was purchased from Atlanta biologicals Inc. (Flowery branch, GA).

3.2.2 Hydrogel scaffold fabrication for in vitro and in vivo studies

Briefly, CHT (1% w/v) solution was prepared in aqueous acetic acid solution (1% w/v). ALG, GG, and KCA (1% w/v) were prepared in distilled water. Two programmable syringe pumps (BS300, Braintree Scientific INC., Braintree, MA) were set at 50mL/h using 10mL syringes connected using luer-lock three-way valve. The opening of the valve was connected to an 18G needle (REF305185, Becton, Dickinson and Company, Franklin Lakes, NJ). Syringes were jacketed with temperature jackets (BS-SYR-H, Braintree Scientific INC., Braintree, MA) which were set at 60°C. Both the pumps were set at 50 mL/h and 14.5 mm syringe diameter. Fibers were manually collected using two 2 cmx2 cm square plastic cover slips mounted over a glass slide at the tip of the needle. The plastic cover slips helped detach the dried scaffold and cut it in precise shape and dimensions. The fibers were collected in such a way that the fibers were aligned parallel to each other.

3.2.3 Cell culture

The MC3T3 cells were cultured in Minimum Essential Medium *alpha* (MEM-a) supplemented with 10% v/v of heat inactivated FBS and 1% v/v antibiotic (Penicillin and

Streptomycin). The cells were cultured in T75 or T125 flasks in a humidified incubator at 37◦C and 5% CO_2. Fresh media was replaced every 2-3 days and cells were split 1:3 at 70% confluence.

3.2.4 Cell seeding on scaffolds

Cells were seeded on scaffolds as described previously.[91] Briefly, fibrous hydrogel scaffolds with an area of 1 cm^2 were sterilized followed by seeding at a density of 200000 cells/scaffold in 24-well plate. Each scaffold was transferred into a new well after 1-day incubation to remove non-adherent cells. MC3T3 cells were cultured in growth media up to 14 days.

3.2.5 Scanning Electron Microscopy (SEM)

Hydrogel samples were flash-frozen in liquid nitrogen and lyophilized prior to 5 nm sputter coating of gold-palladium using Cressington 108 auto sputter coater (Cressignton Scientific Instruments, UK). SEM micrographs were obtained using JEOL 9335 Field Emission SEM (JEOL, Japan) at an accelerated voltage of 3kV and a working distance of 8 mm.

3.2.6 Transmission electron microscopy (TEM)

After 3 days of incubation in SBF the scaffolds were flash-frozen in liquid nitrogen and were immediately kept for lyophilization. Lyophilized samples were kept in Epon for embedding overnight. The sectioned samples were mounted on carbon grids and were scoped using JEM-1011 electron microscope at an accelerating voltage of 80kV.

3.2.7 Fourier transform infrared spectroscopy (FTIR)

Hydrogel scaffolds were flash-frozen in liquid nitrogen and lyophilized. The lyophilized scaffolds were crushed along with vacuum dried potassium bromide (KBr) powder before pressing it into pellet using a hydraulic press. Blank KBr pellet (without any matrix) was used to correct the background. FTIR spectra were recorded in the absorption mode with a resolution of 4 cm^{-1} using Bruker Vertex 70 FTIR spectrometer.[195] The results are presented as an average of 256 scans.

3.2.8 X-ray diffraction spectroscopy (XRD)

After 3 and 10 days of incubation in SBF, the scaffolds were flash frozen in liquid nitrogen and were lyophilized overnight (Labconco Freezone 4.0, Labconco Corporation, Kansas City, MO). Dried scaffolds were crushed, and the powdered samples were tested in Bruker D8 Discover XRD (Bruker Corporation, Billerica, Massachusetts) at a generator voltage of 40kV and current of 40mA. The lyophilized scaffolds were crushed using mortar and pestle in order to analyze crystals present in all different orientations. The 2Θ values were exported and plotted using GraphPad Prism 8 (GraphPad Software Inc., San Diego, CA).

3.2.9 Critical sized mouse calvarial defect and implantation

SKH1 Mice were anesthetized using isofluran 2-5%. The effect of the anesthetic was determined by absent whisker-twitch response and unresponsiveness to gentle, passive extremity extension. Ophthalmic ointment was gently placed on the corneas. The calvaria were prepped with

betadine and draped in standard aseptic fashion. The mouse was then numbered using a base three ear notch system. The operating field was disinfected with 5% solution of iodine. A 1 cm sagittal mid-scalp incision was performed, periosteum was retracted, and a 0.5 cm defect was drilled 1 mm anterior to the lambdoid suture in the calvaria bone with a slow speed handpiece with copious irrigation.

Scaffold, pre-trimmed into 0.5cm diameter disk, was placed in the defect. The skin wound was closed with resorbable sutures.

3.2.10 Micro computed tomography

After 6 weeks and 12 weeks, the calvaria samples were harvested and scanned using VivaCT40 (Scanco Medical AG, Bruttisellen, Switzerland) with settings: energy 55kV, intensity 142 μA, integration time of 300 msec, and isotropic voxel size of 10.5 μm. 3D reconstruction was carried out using the acquired 2D lateral projections using VivaCT40 operating software interface.

3.2.11 Image analysis

FIJI (FIJI is just ImageJ) was used to quantitate bone regeneration outcomes from μCT analysis. Percentage closure of the defect was determined by first setting the scale using the total defect area of 5 mm. Further, wand tool and freehand selection tools were used to annotate the regenerated bone areas to measure the area of regenerated bone. Percentage regenerated bone area of the total defect area was reported and plotted. Further, cumulative osseous bridge was calculated by measuring the length remaining to complete a union of bone going diagonally through the

defect. Percentage length remaining of the total 5 mm length (100) was reported and plotted on the graph.

3.2.12 Histological analysis

Mouse calvaria samples were fixed in 10% paraformaldehyde and subsequently decalcified in ion-exchange decal unit (BioCare Medical, Pacheco, CA) for 6-8 hours after μCT imaging. The decalcified calvaria samples were embedded in paraffin and subsequently sectioned along the longitudinal axis using a microtome. The sections were deparaffinized and rehydrated before hematoxylin and eosin (H&E) and Mason's Trichrome staining (HT15, Sigma--Aldrich Co. (St. Louis, MO) to assess new bone formation.

3.2.13 Histomorphometry analysis

H&E and Trichrome stained samples were evaluated using light microscopy by an independent pathologist. A semi-quantitative scoring system was adapted and modified from Vo *et al.* [196] to evaluate healing of the bone defect. Briefly, a score was assigned for a specimen for each study group. A null score (zero) was assigned when the defect site lacked any bone growth or fibrosis activity; 1 was assigned when the defect site showed presence of histiocytes and new focal immature disorganized bone formation; 2 was assigned when new bone formation was observed with presence of granulation tissue; 3 was assigned when incomplete formation of lamellar bone was observed; 4 was assigned when complete formation of lamellar bone was observed.

3.2.14 RNA isolation and real time quantitative polymerase chain reaction analysis

Mouse pre-osteoblasts (MC3T3) and mouse macrophages (RAW) were cultured on the scaffolds prior to gene expression analysis using real time quantitative polymerase chain reaction (RT-qPCR) after 3 and 14 days for MC3T3 and after 2 and 4 days for RAW cells. RNA was isolated using GeneJET RNA purification kit (Thermo Scientific, Lithuania, EU) according to manufacturer's protocol. Briefly, the cells were collected from the scaffolds after the respective time point and pelleted down. Cell pellet was suspended in lysis buffer which was supplemented with 14.3M β-Mercaptoethanol, 20μL/mL followed by short vertexing. Further, ethanol was added, and the mixture was passage through the GeneJET purification column. Column was washed multiple times with the manufacturer provided buffers and centrifuged at 12,000 rpm. The total RNA adsorbed onto the column was finally eluted using nuclease free water. RNA concentration in the eluent was measured using spectrophotometer (Nanodrop 2000, Thermo Scientific, USA) which reported the RNA quality by measuring the absorbance ratio at 260/280 nm. Expression of osteoblast markers (OCN, OPN, and BMP2) and macrophage markers (IL4, IL6, IL10) were measured while GAPDH was used as a housekeeping control gene. Osteoblasts or macrophages cultured on tissue culture plastic (TCP) were considered as the experimental control. Further, the mRNA expression was measured by RT-qPCR using iTaq Universal SYBR Green RT-PCR kit (172-5150, BioRad Laboratories Inc., USA).

Gene	Forward Primer	Reverse Primer
OCN	GAGGACCATCTTTCTGCTCACT	CGGAGTCTGTTCACTACCTTATTG

OPN	CGCGAATTCCATGAGATTGGCAGT GATTTG	CGCGGATCCTTAGTTGACCTCAGAAGA TG
BMP2	GCTTCTTAGACGGACTGCGG	GCAACACTAGAAGACAGCGGGT
IL4	ACAGGAGAAGGGACGCCAT	GAAGCCCTACAGACGAGCTCA
IL6	ATAGTCCTTCCTACCCCAATTTCC	GATGAATTGGATGGTCTTGGTCC
IL10	GAGAAGCATGGCCCAGAAATC	GAGAAATCGATGACAGCGCC
NOS2	AAACCCCTTGTGCTGTTCTC	GTCTCTGGGTCCTCTGGTCA
GAPDH	GGAGATTGTTGCCATCAACGA	GAAGACACCAGTAGACTCCACGACA

3.2.15 Immunofluorescent staining

Cell-seeded scaffolds were fixed using 4% paraformaldehyde for 20 min and washed three times with DPBS followed by the permeabilization with DPBS containing 0.1% Triton X-100 and blocking in DPBS containing 0.1% Triton X-100 and 5% BSA for 1 h at room temperature. The cell nuclei were stained with Hoechst 33342 (Thermo Fisher Scientific, Waltham, MA). Osteopontin was stained using primary antibody (MPIIIB10(1), Developmental Studies Hybridoma Bank, Iowa city, Iowa) and AlexaFluor 488 secondary antibody (A-11059, Thermo Fisher Scientific, Waltham, MA).

3.2.16 Confocal microscopy

Confocal images were acquired using inverted confocal laser scanning microscope (Olympus Fluoview 1000; Olympus Corporation, Tokyo, Japan) using 488- and 633 nm wavelength lasers. Objective lens of ×20 was used for the z-stack images with 10 μM thickness of each z-slice. Data are presented as maximum intensity projection of the z-stack.

3.3 RESULTS AND DISCUSSION

3.3.1 Fibrous hydrogel scaffolds show collagen-mimetic multi-scale hierarchy

We employed interfacial mixing principle to fabricate interfacial polyionic complexation (IPC) to fabricate single hydrogel fiber with collagen-mimetic structural attributes.[131] These fibers are water insoluble unlike collagen and can readily dry and get rehydrated while maintaining their macroscopic and microscopic structure in various shapes and forms.[116] Electrostatic cross-linking through IPC also obviates the use of cytotoxic photo-crosslinking agents to provide structural integrity to hydrogels. Moreover, in another study, we demonstrated an improved method to fabricate multicomponent IPC fibers with CHT, GG, and graphene via electrostatic interaction which resulted in mechanically strong fibrous composite hydrogel.[91] Here, we have developed a versatile fabrication platform to produce scaffolds with parallelly aligned fibers (**Figure 30A**) for multiple pairs of polysaccharides. We hypothesized that the collagen-inspired multi-scale hierarchical architecture and the polysaccharide raw materials would structurally and chemically resemble bone-ECM features and promote bone regeneration *in vivo.*

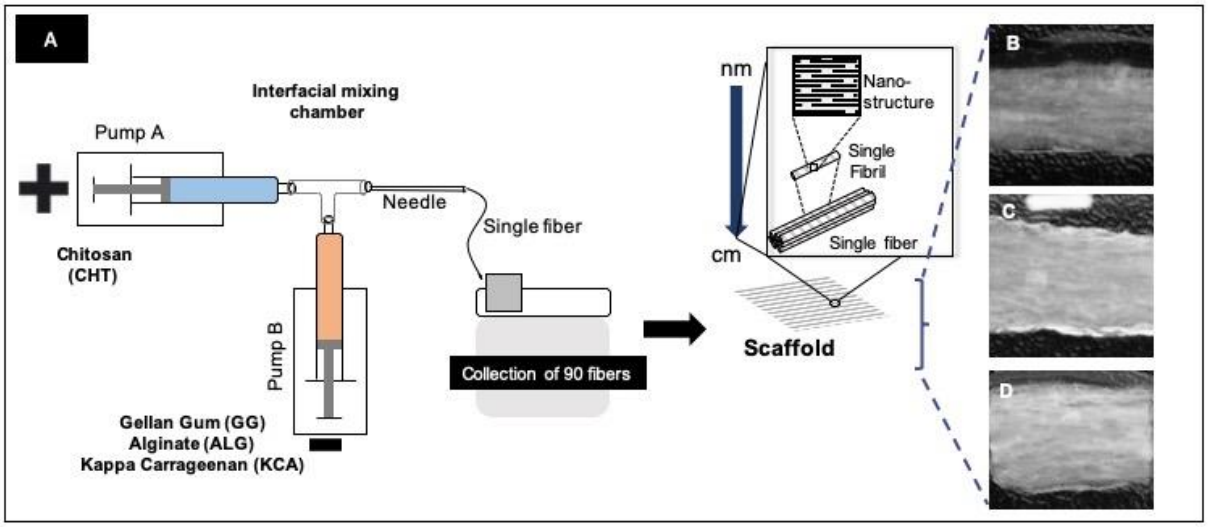

Figure 30: Schematic of collagen-mimetic fibrous hydrogel scaffold fabrication(A) Fabrication setup (left) and schematic representation of bottom-up hierarchy (right) common to the three types of hydrogel scaffolds**; (B, C, and D)** Photographic images of CHT-ALG, CHT-GG, and CHT-KCA scaffold, respectively

Specifically, solutions of positively and negatively charged polysaccharides (1% w/v each) were brought in contact with each other at a fixed rate of 50 mL/h in a microfluidic chamber to form fibers at the tip of the needle (**Figure 30A**). Amine group of CHT crosslinked with carboxylate group of ALG and GG or sulfate group of KCA. Such crosslinked interface formed fibers with continuous infusion of oppositely charged polysaccharides from syringe pumps. Based on the constituents of the fibrous hydrogel scaffolds, we have abbreviated them as CHT-ALG, CHT-GG, and CHT-KCA. Scanning electron microscopy (SEM) images of single fiber of each type (**Figure 1B1, 1C1, and 1D1**) revealed fibrils bundling up to make each type of fiber whereas transmission electron microscopy (TEM) images of single fiber exhibited periodic regions with differential electron density, which appeared as light and dark bands at nanoscale for all three polymer pairs (**Figure 1B2, C2 and D2**). These fibers were collected and arranged manually parallel to each other to produce a bilayer scaffold with 45 fibers in each layer. Macroscopic structures showed similarity between the three pairs of scaffolds (**Figure 30B, 30C, and 30D**).

Similarly, light microscopy images of scaffolds exhibited parallel alignment of fibrils in the scaffolds (**Figure 31A3, 31B3, and 31C3**). Further, surface analysis of scaffolds using SEM (**Figure 31A4, 31B4 and 31C4**) exhibited fibrous surface morphology in all three pairs with parallel fibrils within fibers. Thus, fabricated scaffolds exhibited fibers made up of several fibrils, which formed differential electron density regions at nanoscale through self-assembly similar to tropocollagen chains. Collectively, the bottom-up self-assembly of oppositely charged polysaccharides resembled natural bone tissue, in which self-assembled nano-scale building blocks and their hierarchical organization confer unique strength, flexibility and facilitates functional feasibility to the tissue at multiple length-scale.[134]

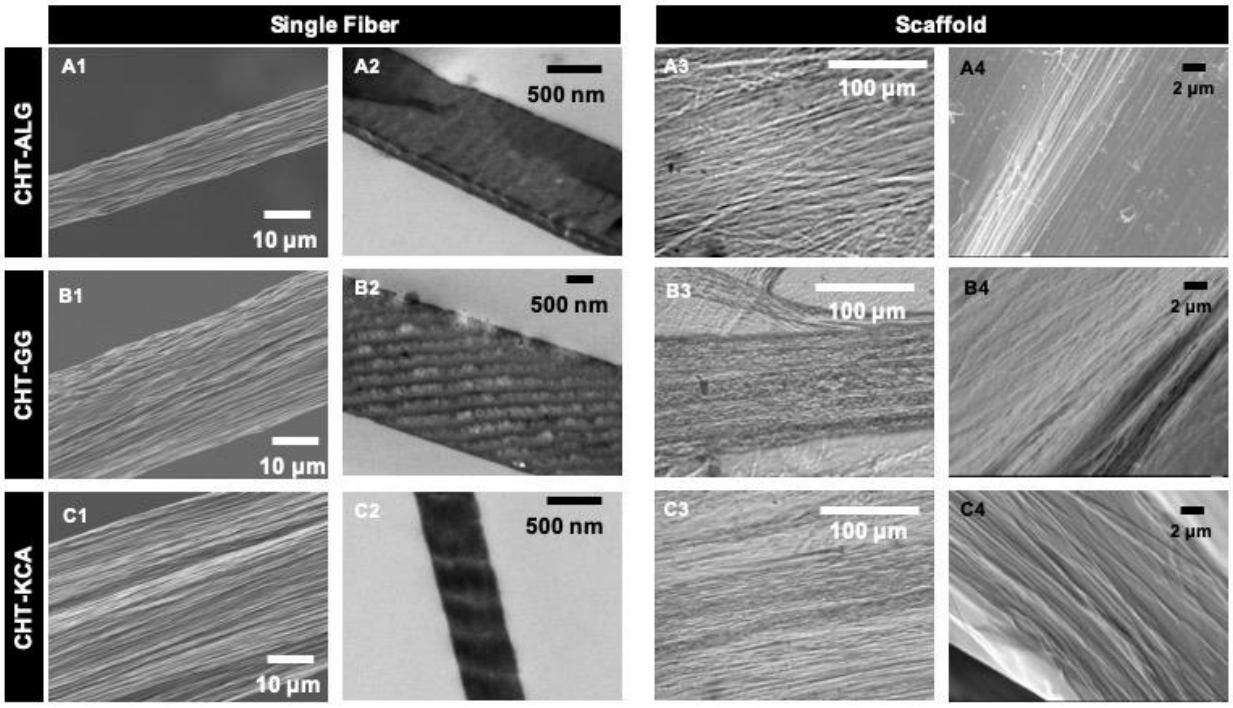

Figure 31: Collagen-mimetic multi-scale hierarchical structure of fibrous hydrogel scaffolds.A1, B1, and C1) SEM micrographs of single fiber of CHT-ALG, CHT-GG, and CHT-KCA, respectively. **(A2, B2, and C2)** TEM micrograph showing dark and light regions with periodically varying electron density at nanoscale for single fiber of CHT-ALG, CHT-GG, and CHT-KCA, respectively. **(A3, B3, and C3)** Light microscopy images of CHT-ALG, CHT-GG, and CHT-KCA scaffold, respectively; **(A4, B4, and C4)** SEM micrograph showing fibrous surface of CHT-ALG, CHT-GG, and CHT-KCA scaffold,

3.3.2 Fibrous hydrogel scaffolds promote biomimetic mineral deposition on the scaffolds after incubation in simulated body fluid

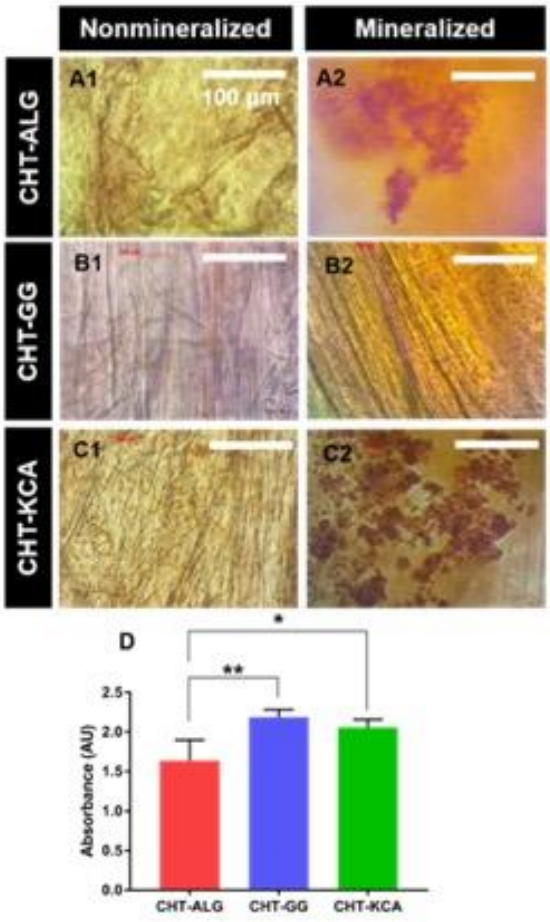

Figure 32 : Alizarin red assay on three-day mineralized scaffolds.A1, B1, and C1 show light microscopy images of alizarin red stained CHT-ALG, CHT-GG, and CHT-KCA scaffolds, respectively. **A2, B2, and C2** show similar images for three-day mineralized CHT-ALG, CHT-GG, and CHT-KCA scaffolds, respectively. **D** shows quantification of Alizarin red using cetylpyridinium chloride

The ability of biomaterial to promote deposition of calcium phosphate minerals is considered as a predictor of its *in vivo* mineralization bioactivity.[197] In order to simulate *in vitro* mineralization, scaffolds were incubated in simulated body fluid (SBF) with similar ion concentration to that of human blood plasma.[197] Following three days of incubation in SBF,

mineral deposition on the scaffolds was assessed through Alizarin Red S staining (stains for calcium) for all the three pairs. CHT-ALG (**Figure 32A1-A2**) showed smaller granular mineral deposits whereas CHT-GG (**Figure 32B1-B2**) and CHT-KCA (**Figure 32C1-C2**) showed relatively larger mineral deposits on the surface of the scaffolds. Moreover, CHT-GG and CHT-KCA exhibited greater extent of mineralization than that of CHT-ALG as confirmed with quantification of alizarin red stain (**Figure 32D)**. Further surface characterization of morphology of minerals deposited on the surface after 3 days of mineralization for CHT-GG (**Figure 33B1**) and CHT- KCA (**Figure 33C1**) were similar with irregular shapes compared to mostly spherical mineral deposits on CHT-ALG (**Figure 33A1**). At higher magnification SEM images, CHT-ALG confirmed spherical mineral morphology (**Figure 33A2**) whereas CHT-GG (**Figure 33B2**) and CHT-KCA (**Figure 33C2**) showed similar irregularly shaped mineral morphology.

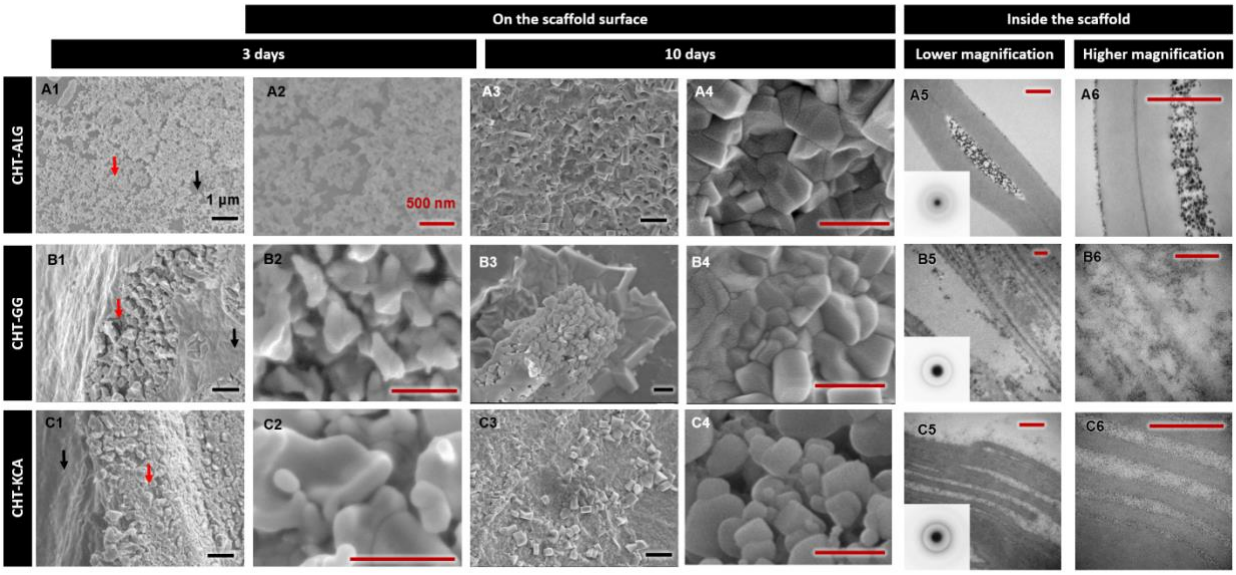

Figure 33 : Surface mineral morphology after *in vitro* mineralization. (A1-A2, B1-B2 and C1-C2) SEM micrographs of the deposited minerals (red arrow) and scaffold area without minerals (black arrow) for three-day mineralized CHT-ALG, CHT-GG, and CHT-KCA, respectively; (**A3-A4, B3-B4 and C3-C4)** SEM micrographs for ten-day mineralized CHT-ALG, CHT-GG, and CHT-KCA, respectively; **A5-A6, B5-B6, and C5-C6** show transmission electron microscopy images of transverse sections of three-day mineralized CHT-ALG, CHT-GG, and CHT-KCA, respectively; **Inset images in A5, B5, and C5** show selected area electron diffraction patterns of the corresponding scaffold type;

The greater extent of mineralization by CHT-GG and CHT-KCA indicate stronger affinity of the scaffold to promote sequestration of calcium ions from SBF which could be due to higher availability of negative charge or structural nucleation sites on the scaffold surface. Specifically, the capacity of a functional group to induce apatite formation was found to be in the order of PO4H2 > COOH ≫ CONH2 ≃ OH > NH2 ≫ CH3 ≃ 0 by Tanahashi and Matsuda.[198] Unfortunately, their study did not include sulfate group, making direct interpretation difficult for carboxylate *vs.* sulfate in the context of our study. In case of our scaffolds, it can be observed that both CHT-GG and CHT-KCA show similar extent of apatite formation on the surface despite their different functional groups (carboxylate and sulfate functional groups) CHT-ALG and CHT-GG possess the same carboxylate functional group, however, average ALG chain has almost half surface charge as compared to average GG chain (zeta potential data from Chapter 1). This could possibly mean that the charge neutralization in ALG resulted in less net surface charge after CHT-ALG crosslinking compared to CHT-GG. Interestingly, CHT-ALG and CHT-GG showed significant difference in the extent of apatite formation on the surface possibly due to different available surface charges, thereby supporting different mineral- scaffold interaction.

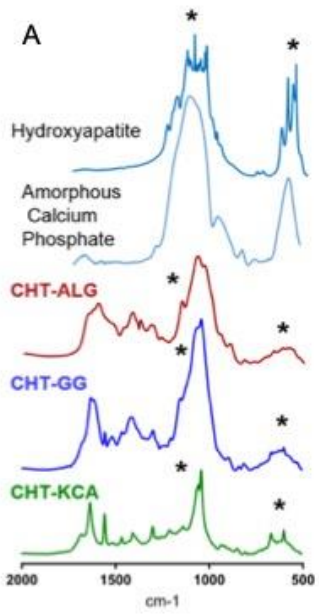

B

	Phosphate signature peaks
CHT-ALG	588.3 (smooth)
CHT-GG	597.9, 617.2 (sharp)
CHT-KCA	597.9, 626.8 (sharp)
Hydroxyapatite	540.0, 600.0 (sharp)
Amorphous calcium phosphate	574.0 (smooth)

Figure 34 : FTIR spectra of three-day mineralized scaffolds and positive controls (star indicates calcium phosphate peak): **A** shows FTIR spectra and **B** shows table of matching phosphate peaks in which CHT-ALG showed resemblance with amorphous calcium phosphate whereas CHT-GG and CHT-KCA showed resemblance with hydroxyapatite.

Further chemical characterization for three-day mineralized scaffolds through Fourier transform infrared spectroscopy (FTIR) spectrum showed characteristic peaks of phosphate group (**Figure 34A**). However, we observed differences among the three pairs. For example, CHT-GG showed a peak at 597.9 cm^{-1} extending as a smooth curve with a tiny shoulder at 617.2 cm^{-1}, whereas CHT-KCA showed peaks at 597.9 cm^{-1} and 626.8 cm^{-1}, although with sharp shoulders. Such peaks resemble typical sharp double peaks of HA at approximately 540 cm^{-1} and 600 cm^{-1} which indicate v_4 vibration of phosphate group.[199, 200] Moreover, the peak at 630 cm^{-1} suggests vibrational mode of OH^- ions in of HA. On the other hand, three-day mineralized CHT-ALG showed relatively smooth peak at 588.3 cm^{-1} (**Figure 34A**) which resembles typical smooth peak of amorphous calcium phosphate (ACP) near 574 cm^{-1}. These signature peaks for phosphate are summarized in a table in **Figure 34B.** Additionally, CHT-ALG, CHT-GG and CHT-KCA showed

a sharp peak at 1039 cm^{-1} with a shoulder at 1047, 1053, and 1070 cm^{-1}, respectively which further confirm vibrations of phosphate group (1072-1032 cm^{-1}).[199] Thus, spectra for mineralized CHT-GG and CHT-KCA exhibited peaks resembling HA-like apatite whereas peaks in CHT-ALG indicate ACP-like amorphous mineral depositions after three-day mineralization. Taken together, morphological and chemical characterization results indicated that within three days of SBF incubation of scaffolds from all three pairs provided sites of nucleation and promoted growth of biomimetic minerals over the scaffold.

The mineral morphology differences observed through SEM of three-day mineralized scaffolds disappeared in ten-day mineralized scaffolds (**Figure 33A3, 33B3, and 33C3**), to appear as packed mineral morphology irrespective of the scaffold. Moreover, the extent of mineralization for each of the three pairs was higher as well as uniformly distributed after ten-day mineralization compared to its three-day mineralized counterpart. By day 3, scaffold surface could be seen (black arrow, **Figure 33A1, 33B1, and 33C1**) whereas by day 10, almost entire hydrogel scaffold surface was covered with minerals (**Figure 33A3, 33B3, and 33C3**). Additionally, micro computed tomography of CHT-GG was carried out to confirm uniform distribution of mineral deposition. Non-mineralized CHT-GG did not show any signal, whereas CHT-GG incubated in SBF for ten days showed uniform distribution of minerals (**Figure 35**)

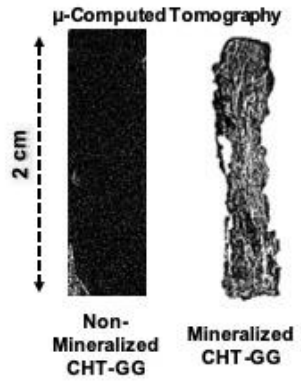

Figure 35 : 3D Micro-CT image of CHT-GG scaffold A representative three-dimensional micro-CT image of 2 cm x 0.5 cm non-mineralized CHT-GG (left) and ten-day mineralized CHT-GG scaffold.

To further characterize crystal types of the deposited minerals, X-ray diffraction (XRD) analysis of mineralized scaffolds was carried out. All three pairs exhibited crystalline spectra as shown in **Figure 36A** (three days) and **36B** (ten days). Interestingly, CHT-KCA (green spectrum) showed more prominent peaks matching with carbonated apatite after both three and ten days of mineralization, whereas CHT-GG and CHT-ALG showed similar carbonated apatite ()peaks after three days, which was converted to more HA-like peaks (00-001-1008) after ten days.[201, 202] Such apatite formation on the surface of SBF-incubated biomaterial is used as an indicator of bone-bonding (osteointegration) ability when implanted *in vivo*.[197] Moreover, during natural bone development, anionic macromolecular matrix composed of mostly collagen works as the regulator of mineralization which is similar to the role of common anionic polysaccharide chitosan in our scaffolds. Further, functional groups available at the surface of scaffolds is known to control deposited mineral crystal-type in SBF.

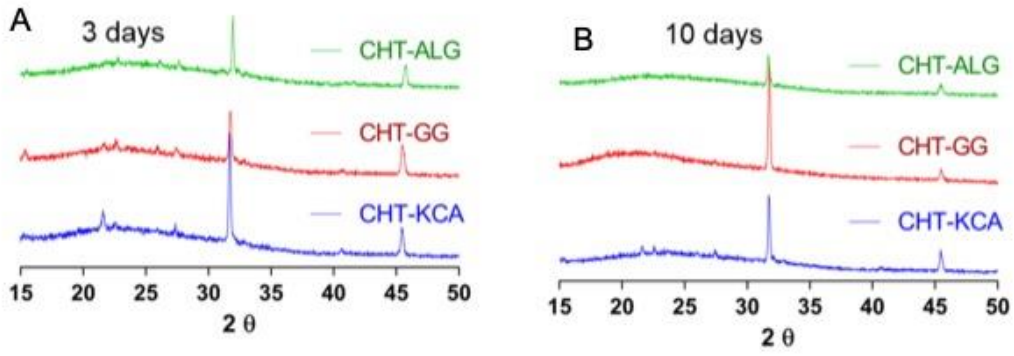

Figure 36 : XRD spectra of three-day (D1) and ten-day (D2) mineralized scaffolds

After confirming presence of apatite-like mineral on the surface of hydrogel scaffolds as early as 3 days, TEM was employed to evaluate potential of three hydrogel scaffolds to deposit minerals inside the hydrogel scaffolds. Transversely sectioned samples were mounted on the grid for TEM imaging. Relatively lower magnification images (**Figure 33A5, 33B5, and 33C5**) confirm the presence of minerals inside the hydrogel scaffolds. Higher magnification images (**Figure 33A6, 33B6, 33C6**) exhibited distinct patterns of mineral deposition for different pairs. Specifically, CHT-GG and CHT-KCA both exhibited similar intrafibrillar distribution of minerals (**Figure 33B5 and 33C6**), while CHT-ALG showed aggregation of minerals in interfibrillar space (**Figure 33A6**). On similar lines, Boskey studied the effect of surface minerals on the minerals inside the materials and concluded that mineral deposits on the surface guide crystal orientation within fibrils and also dictate their size and shape.[203] Considering the patterns of mineral deposition on both surface and inside together, SEM images of three day mineralized CHT-GG and CHT-KCA revealed greater mineral deposition on the surface of scaffolds than CHT-ALG scaffolds, which could act as a diffusion barrier, preventing infiltration of the larger mineral deposits beyond surface in CHT-GG and CHT-KCA. On the other hand, CHT-ALG scaffolds do not deposit significant amount of minerals on the surface of scaffold initially which allows saturated mineral liquid phase to easily diffuse inside the scaffold. As the minerals are sequestered

inside the scaffold to a greater extent in CHT-ALG, they start aggregating intrafibrillar as described earlier in **Figure 33A5 and 33A6**. Thus, diffusion kinetics of minerals inside the scaffolds depends on the extent of mineral deposition on the surface. Collectively, characterization of mineral deposits on the surface and inside of the scaffold could be according to widely acknowledged hypotheses that the amorphous mineral nucleation on surface diffuses into the inside as well as transforms from crystalline phase by losing water over time.[204] Organized mineral deposition along the fiber alignment demonstrate biomimetic molecular interaction between mineral-scaffold throughout the scaffold. Altogether, polyionic nature of the polysaccharides in the hydrogel scaffolds and fibrous alignment could be attributed to the deposition of biomimetic minerals to form biomimetic composites.

3.3.3 Lyophilized CHT-KCA promotes significant closure of critical-sized calvarial defect after 12-weeks of implantation compared to empty defect

Next, bone regeneration efficacy of hydrogel scaffolds was evaluated in critical size (5 mm diameter) mouse calvarial defect model. All three pairs of hydrogel scaffolds were further processed in aseptic conditions and implanted in hydrated form to test their potential for bone regeneration. Surgical implantation of hydrogel scaffolds in critical size calvarial defect is shown with representative images of exposed calvaria (**Figure 37A1**), marked defect area (**Figure 37A2**), and removed calvaria (**Figure 37A3**).

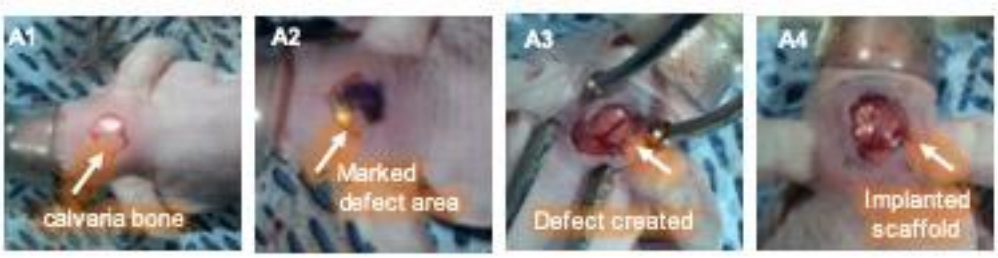

Figure 37 : Hydrogel scaffold implantation surgery.(A1) Calvaria bone in the skull, (**A2)** marked 5mm diameter area for creating the defect, **(A3)** calvarial bone defect exposing the brain underneath, and **(A4)** implanted scaffold;

Hydrated hydrogel scaffolds often pose a challenge to handle during the surgery and drop-out or misplacement post-implantation, requiring suturing of fascia,[205] however, our hydrogel scaffolds were retained in the defect area as seen in **Figure 37A4**. At the end of 12-weeks, none of the three pairs of hydrogel scaffolds led to serious systemic reaction like difficulty in movement or sudden weight loss in mice (data not shown). μCT was employed to quantitate the extent of bone regeneration as well as visualize the spatial distribution of regenerated bone. Out of the three types of hydrogel scaffolds, CHT-KCA (**Figure 38A1-A2**) exhibited greater bone regeneration than empty defect control after 12 weeks, however, CHT-GG (**Figure 38B1-B2**) and CHT-ALG (**Figure 38C1-C2**) failed to significantly regenerate bone compared to empty defect control. While CHT-KCA showed significantly better osteoinduction than empty defect after 12 weeks, we observed less than 40% closure of the defect (**Figure 38D**).

Similar to our growth-factor-free approach, Koike *et al.* assessed osteoinductive efficacy of bacterial cellulose (BC), which is made of type I and type II cellulose forming 3D architecture with randomly oriented nanofibers in a rabbit frontal sinus model.[189] The ectopic bone tissue formed surrounding implanted BC was attributed to the 3D microfibrillar network leading to stem cell and fibroblast recruitment and organization. This is similar to fibrous architecture and multi-scale hierarchy of our hydrogel scaffolds, which can act as a 3D guide for the local cells to populate

the hydrogel and allow organized bone regeneration. Another similar study reported bioactive injectable poly(N-isopropylacrylamide (PNiPAAm) hydrogel implants. PNiPAAm hydrogels mineralized and regenerated rat calvarial defect after 12 weeks without added cell, growth factors or minerals similar to our study, although their early time point of four weeks of did not show any bone growth.[196] The mineralization initiation and bone regeneration activity was attributed to hydrophobicity as driving force in PNiPAAm hydrogel study, whereas our hydrogels promoted bone regeneration due to its polyionic composition made of osteogenic polysaccharides.

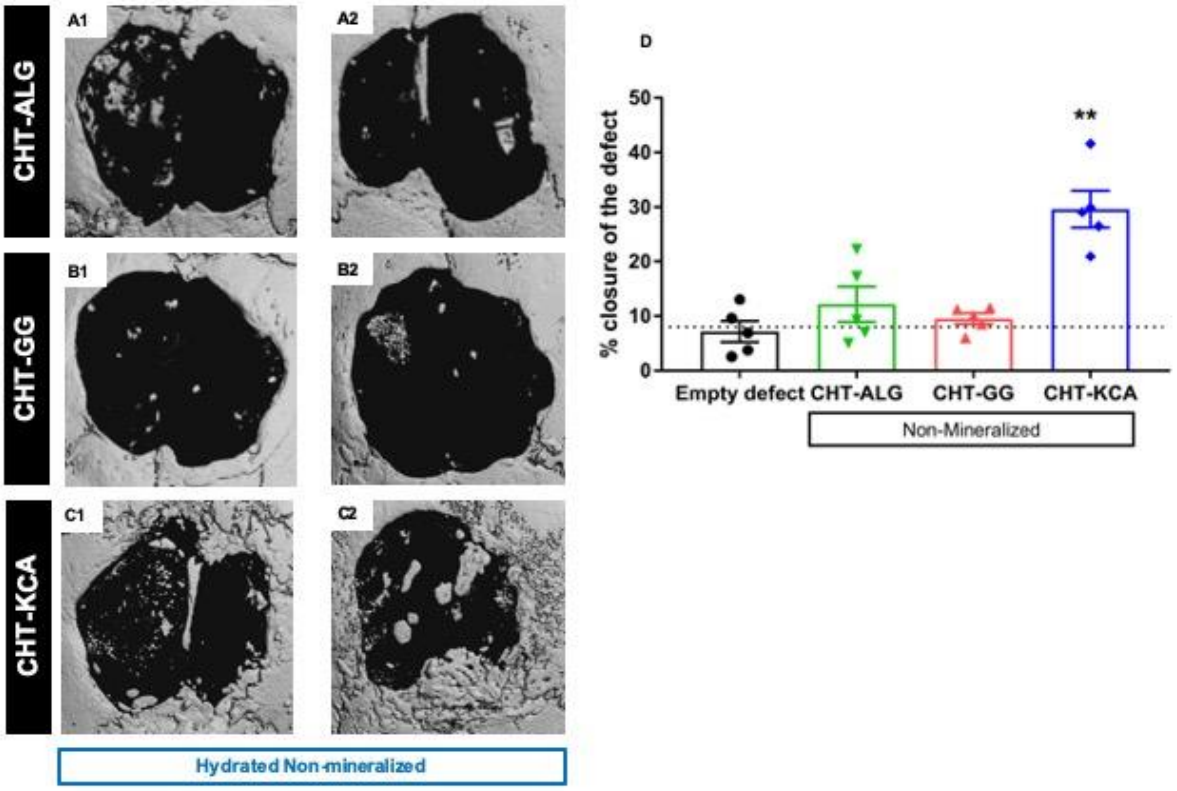

Figure 38 : Closure of mouse critical sized defect 12-weeks after implantation of nonmineralized scaffoldsA1-A2 show representative 3D reconstructed μCT images for non-mineralized CHT-ALG; **B1-B2, and C1-C2** show similar μCT images for non-mineralized CHT-GG, and CHT-KCA, respectively. **D** shows a comparison of percent closure of the critical sized defect by regenerated bone quantified using FIJI. ** indicates statistical significance ($p<0.005$) compared to empty defect with one-way ANOVA analysis and Tukey's post-hoc test; error bars: standard error of mean; n=5.

Among the three types of hydrated hydrogel scaffolds implanted in our study, better performance of CHT-KCA may be attributed to the presence of sulfate group from carrageenan as sulfate has been shown to improve bone regeneration bioactivity.[206-208] The difference in three types of hydrogel scaffolds to facilitate bone growth could also be due to the protein deposition ability from serum, which could potentially help attract stem cells and osteoblasts from the surrounding area. Sulfate group in carrageenan has shown to possess greater ability to bind to proteins.[209] In addition, sulfated polysaccharides prevent protein denaturaturation and prolong its efficacy.[210] Relatively stronger binding of KCA chains to the endogenously produced growth factors at the implant site may have rendered CHT-KCA with higher osteoinduction as compared to gellan gum and alginate.

Calcium phosphate minerals have been utilized mostly for their osteoconductive properties when used as chemically synthesized highly crystalline form such as HA ,[211] however, they have been indicated as osteoinductive when HA were mixed to form biphasic mixtures with beta tricalcium phosphate (β-TCP) and other soluble calcium phosphate, which release calcium and phosphate ions.[212, 213] These are used as a physical mixture and fail to mimic the intricacies of natural nanocomposite formation at multiple length-scale. However, we found that our hydrogel scaffolds promoted formation of organic-inorganic composites with crystalline apatite with carbonated substitutions rendering them with advantages of both crystalline apatite and soluble calcium phosphate locally releasing ions. Therefore, to further increase the bone regeneration bioactivity of CHT-KCA, mineralized CHT-KCA were implanted in the critical size (5 mm) mouse calvarial defect. Mineralized CHT-KCA were aseptically fabricated in a similar way to *in vitro* characterization studies (**Figure 33**) using sterile SBF and implanted in mice in hydrated form. Indeed, the extent of closure with mineralized CHT-KCA (**Figure 39C1-39C2**) was

significantly improved compared to empty defect (**Figure 39A1-39A2**) and about 5-10% greater closure of the defect was achieved compared to hydrated non-mineralized CHT-KCA. The improved bone regeneration performance of hydrated mineralized CHT-KCA was further evident by presence of unidirectional non-union regenerated bone spicules compared to empty defect. However, mineralized CHT-KCA showed only marginal improvement compared to non-mineralized CHT-KCA. Quantification of defect closure (**Figure 39D1**) and cumulative length of osseous bridge (**Figure 39D2**) revealed significantly better performance of mineralized CHT-KCA as compared to empty defect, however, it was similar to non-mineralized CHT-KCA.

Figure 39 : **Closure of mouse critical sized defect 12-weeks after implantation of scaffolds (A1-A2)** Representative 3D reconstructed μCT images for empty control (no material implanted in the calvarial defect); **(B1-B2 and C1-C2)** μCT images for nonmineralized and mineralized CHT-KCA, respectively, in hydrated form; **(A3-A4)** μCT images for lyophilized collagen sponge, **(B3-B4 and C3-C4) μ**CT images for non-mineralized and mineralized CHT-KCA, respectively, in lyophilized form; **(D1)** a comparison of percent closure of the critical sized defect by regenerated bone quantified using FIJI and **(D2)** shows a comparison of percent cumulative length of osseous bridge quantified using FIJI. * indicates statistical significance ($p<0.05$) compared to empty defect with one-way ANOVA analysis and Tukey's post-hoc test, ** indicates $p<0.005$, **** indicates $p<0.00005$; error bars: standard error of mean; n=5.

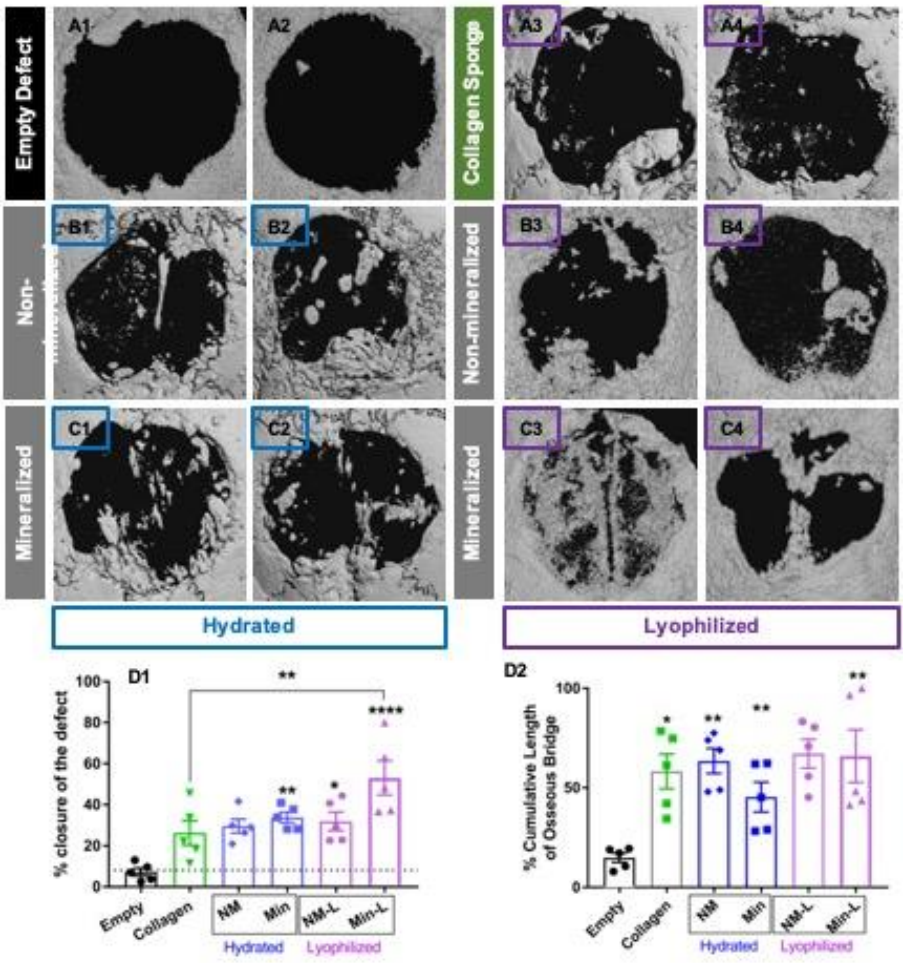

In a similar approach, Shao *et al.* determined efficacy of nanohydroxyapatite (nHA) with or without BMP2 peptide covalently immobilized in an *in situ* forming GelMA hydrogel.[214] Their GelMA-nHA group did not show significant bone regeneration compared to control after 4 or 12 weeks of implantation in 5 mm rat calvaria defect, whereas our hydrogels enhanced bone regeneration without any added growth factors which can be attributed to the influence of organized anisotropic assembly of mineral-fiber composites. Additionally, the surface crystalline deposits could have led to the protein adsorption due to nano-/submicron-scale surface roughness and surface electrostatic charges.[215, 216]

Moreover, amorphous mineral deposits inside the hydrogel scaffolds and leaching of crystalline minerals may have created calcium and phosphate rich microenvironment similar to

inorganic mixture of biphasic calcium phosphate consisting of HA and β-TCP.[213, 217, 218] In separate studies, calcium ions from such microenvironment have shown to stimulate mature bone cells via nitric oxide formation and stimulates osteoblasts through extracellular signal–regulated kinases 1/2 (ERK 1/2) pathway [219, 220] whereas phosphate ions, which exists mostly in PO_4^{3-} form, have shown to regulate growth and differentiation of osteoblasts via ERK1/2 and Insulin-like growth factor 1 (IGF-1) pathways as well as increase in BMP expression.[221-223] Collectively, presence of both crystalline and amorphous mineral deposits on the surface and inside the scaffolds together with bioinspired fibrous multi-scale architecture of hydrogel scaffolds may have conferred osteoconductive and osetoinductive property. However, the performance of mineralized CHT-KCA was 5-10% better than its non-mineralized counterpart for closure of the calvarial defect. This could be attributed to wash-out of some of the mineral deposits due to excessive saline washing at the defect site following bleeding. Following commonly used implantation procedure, the mineralized CHT-KCA were implanted directly after their removal from sterile SBF while in hydrated form. Washout of the minerals from the hydrated hydrogel may have reduced mineralized scaffolds similar to non-mineralized CHT-KCA.

Therefore**,** in order to preserve deposited minerals, mineralized CHT-KCA was processed in lyophilized form after 10 days of incubation in simulated body fluid (SBF) prior to its implantation.[197] Additionally, lyophilization of biomaterials preserves the architecture of the scaffold [224], makes it less prone to bacterial infection and improves its shelf-life. Preservation of mineral deposits while maintaining porosity of the hydrogel is essential to ensure its bioactivity. Indeed, lyophilized mineralized CHT-KCA showed greater bone regeneration (**Figure 39C3-39C4)** compared to its non-mineralized counterpart (**Figure 39B3-39B4**), lyophilized collagen sponge used as a positive control (**Figure 39A3-39A4** and empty defect group (**Figure 39A1-**

39A2). Further quantification of closure showed highest statistical significance for lyophilized mineralized CHT-KCA among all the groups when compared to the empty defect. Interestingly, lyophilized mineralized CHT-KCA showed significantly better closure compared to lyophilized collagen sponge. However, due to biological variation among five mice, lyophilized form was not found to be significantly different compared to the hydrated form. Quantification of cumulative length of osseous bridge showed significantly better percentage for lyophilized mineralized CHT-KCA; however, it did not show differences among the other groups.

3.3.4 Histological evaluation of the regenerated mouse calvarial defect showed better healing for scaffold implanted group compared to empty

Further, we performed histology on the regenerated defect area to evaluate the quality of the regenerated bone. Two regions of interest were identified as 1) new bone region (NB) (color-coded as green box) and 2) native old bone (OB) (color-coded as purple box). Empty defect group (control, **Figure 40A1, 40A2, 40A3**) showed limited bone growth. Further detailed evaluation of the NB region (green) showed absence of bone cells and demonstrated mainly brain tissue underneath the defect (**Figure 40A4-40A5**). The NB region of the empty defect contained hemosiderin-laden macrophages (**Figure 40A6-40A7**), representing cellular response to the defect. Based on the overall morphology and organization of regenerated bone, the healing score (H-Score) of the NB region reflected a null score out of four (**Table 2, Figure 41**). The treatment group with non-mineralized CHT-KCA (**Figure 40B1, 40B2, 40B3**) showed focal hemosiderin, focal immature and disorganized bone as well as presence of histiocytes and lymphocytes indicating focal bone regeneration activity in the NB region (**Figure 40B4-40B5**), whereas a lining

of immature bone at the defect edge was seen near the OB region (**Figure 40B6-40B7**) (**Figure 41, Table 1**). Immature and disorganized bone in the NB region reflected an H-score of one out of four (**Table 2, Figure 41**). Interestingly, the mineralized CHT-KCA (**Figure 40C1, 40C2, 40C3**) group revealed granulation tissue, presence of immature bone, histiocytes, and neutrophils indicating greater extent of focal bone growth in the NB region (**Figure 40C4-40C5**) compared to non-mineralized CHT-KCA. The presence of granulation tissue in the NB region was reflected by an H-score of two out of four (**Table 2, Figure 41**). Additionally, the collagen organization of bone in the NB region for bone in the mineralized CHT-KCA group was highest among the three treatment conditions.

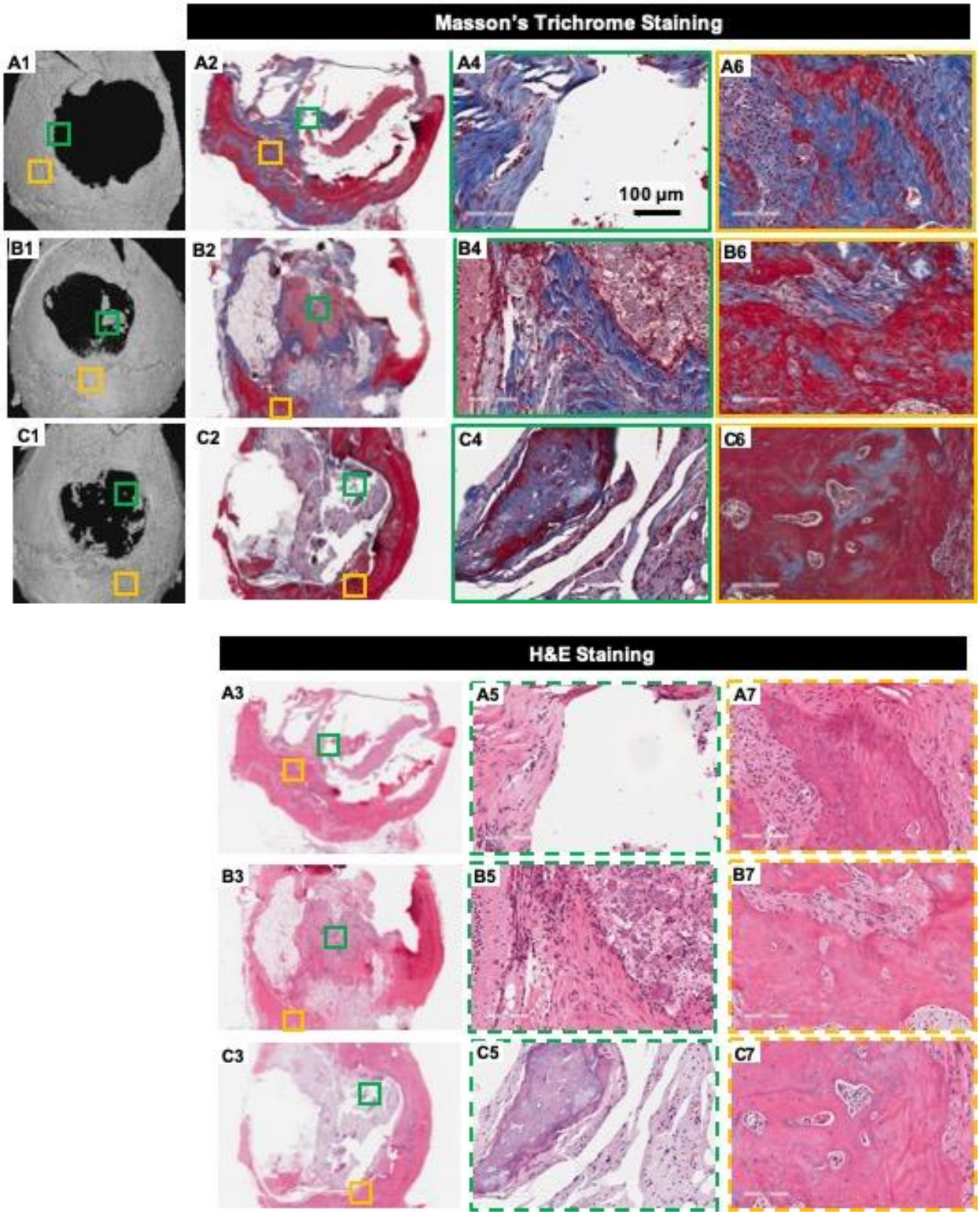
Masson's Trichrome Staining
A1
A2
A4
A6
100 µm
B1
B2
B4
B6
C1
C2
C4
C6
H&E Staining
A3
A5
A7
B3
B5
B7
C3
C5
C7

Figure 40 : **Histological analysis of regenerated mouse calvaria.(A1, B1, and C1)** μCT images of empty defect control, non-mineralized lyophilized CHT-KCA, and mineralized lyophilized CHT-KCA implanted mice used for histology sectioning, respectively. **(A2, B2, and C2)** Mason's Trichrome stained stitched images of longitudinal section of empty defect control, non-mineralized lyophilized CHT-KCA, and mineralized lyophilized CHT-KCA implanted mice, respectively; **(A3, B3, C3)** Similar H&E stained stitched image of longitudinal section of empty defect control, non-mineralized lyophilized CHT-KCA, and mineralized lyophilized CHT-KCA, respectively**; (A4-A5, B4-B5, C4-C5)** Magnified images from new bone region (NB) are indicated in green boxes for control, non-mineralized, and mineralized scaffolds, respectively. **(A6-B7, C6-C7, D6-D7)** Similar images from the native old bone region (OB) are shown in yellow boxes. Solid lined boxes are used to indicate Mason's Trichrome stained images and dotted lined

We found two studies where growth-factor-free materials were tested in calvarial defect of rabbit and rat.[189, 196]Specifically, Koike *et al.* observed immature bone around bacterial cellulose matrix populated with osteoblasts in a rabbit frontal sinus model[189] They also found the quality of regenerated bone using bacterial cellulose matrix to be better than the BMP2 alone group due to superior recruitment and 3D organization of the incoming host cells. Additionally, the inflammatory response to our hydrogel scaffolds was less than that of the hydrogels implanted by Vo *et al.* in the rat calvarial defect.[196] In contrast to their observation, we did not observe any prominent features of fibrotic capsule formation, although the presence of fibrosis and histiocytes could point to inflammatory response essential for bone repair.

Table 1

Qualitative	New Bone Region	Native Old Bone Region
Empty	No bone growth, mostly brain tissue from underneath.	Fibrosis, hemosiderin laden macrophages, fibroblasts proliferation.
Non-mineralized	Fibrosis, focal hemosiderin, focal immature bone, disorganized bone present, histiocytes, occasional lymphocytes.	Fibrosis, fibroblastic proliferation, numerous histiocytes, lining of immature bone at defect edge.
Mineralized	Fibrosis, small amount of immature bone, some neutrophils, histiocytes, granulation tissue.	Small area of fibroblastic proliferation, osteoblastic rimming.

Table 2

Quantitative	Average H-score
Empty	0
Non-mineralized	1
Mineralized	2

Figure 41 : Histomorphometry analysis and H-score of regenerated mouse calvaria.(Table 1) Qualitative evaluation of H&E and Mason's Trichrome stained longitudinal sections of mice calvaria from two different regions (Green-NB and Yellow-OB). **(Table 2)** Healing score (H-score) of the same sections from NB area; Score range: 0-4; NB- new bone, OB- old native bone.

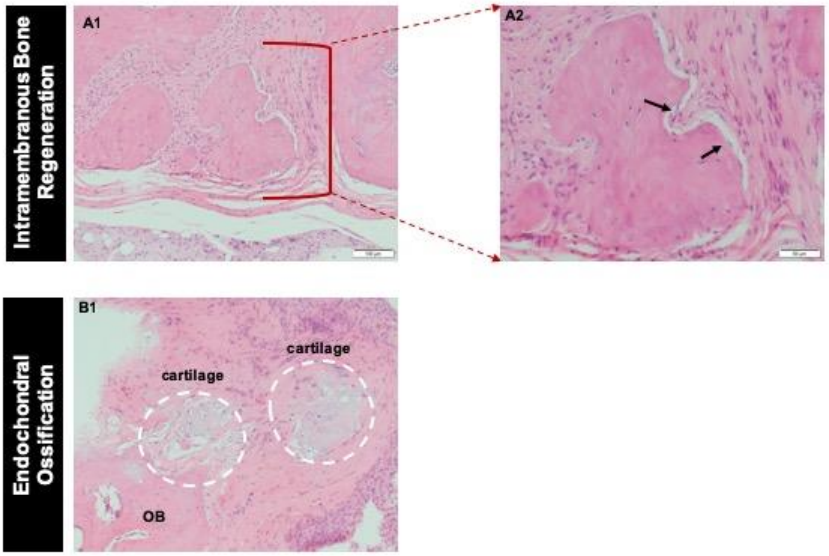

Figure 42 : H&E images showing bone regeneration mechanism in mineralized lyophilized CHT-KCA(A1) H&E stained mineralized lyophilized CHT-KCA implanted mouse show new bone formation **(A2)** Magnified distinct lines (black arrows) showing direct new bone deposition possibly by mesenchymal cells indicating intramembranous bone regeneration; **(B1)** H&E stained mineralized lyophilized CHT-KCA implanted mouse show cartilage formation (white dotted circles) indicating endochondral ossification; OB- old native bone.

Further investigation of mechanism of bone growth in mineralized CHT-KCA group revealed that the bone regeneration was through both the intramembranous bone regeneration (**Figure 42A1-42A2**) and endochondral ossification (**Figure 42B1**) although intramembranous growth predominantly was observed. In fact, implantation of *in vitro* chondrogenesis priming induced cells is proposed as an alternative strategy for enhanced bone regeneration in skull defects.[225, 226]

Bone regeneration in the calvaria region is believed to occur via an intramembranous mechanism whereby mesenchymal cells differentiate into osteoblasts and deposit osteoid, in turn, calcifies to become woven bone.[227] Therefore, the bone spicules in μCT and focal bone tissue in histology indicated successful osteoinduction by mineralized CHT-KCA. This can be attributed to our mineralization approach that led to biomimetic mineral deposition

inside and on the surface of the scaffold (**Figure 33**). Thus, the biomimetic mineralization and hierarchically aligned CHT-KCA structure may have resulted in housing the native mesenchymal cells to initiate bone formation.

3.3.5 Pre-osteoblasts seeded on hydrogel scaffolds showed osteogenic gene and protein markers

To further investigate osteogenic properties of non-mineralized and mineralized scaffolds, qRT-PCR was employed on MC3T3 cells cultured for 3 and 14 days. Early-stage osteogenic marker such as BMP-2 showed significantly higher m-RNA expression in mineralized scaffold group on day 3 as compared to non-mineralized treatment group as well as in cells seeded on tissue culture plate (TCP) group on day 3 (**Figure 43A1**). However, subsequent time point of day 14 did not show significantly higher mRNA for BMP2. This could be due to amorphous calcium phosphate inside the mineralized scaffolds (inset image, **Figure33C5**) possibly releasing calcium and phosphate ions in the surrounding microenvironment or crystalline HA-like minerals from the surface resorbing in the media. Specifically, phosphate ions are known to increase BMP expression via ERK1/2 and IGF-1 pathway.[221-223] Additionally, late-stage osteogenic markers such as osteopontin (OPN, **Figure 43A2**) and osteocalcin (OCN, **Figure 43A3**) showed higher mean mRNA expression for mineralized scaffolds compared to TCP for both 3 days and 14 days indicating sustained upregulation of OPN, which is popularly used osteogenic marker. However, non-mineralized scaffolds promoted higher mRNA expressions for OPN whereas mRNA expression of OCN remained unchanged compared to TCP. Recently, studies with biomaterials have focused on sustained or sequential delivery of cytokines to facilitate genetic manipulation of macrophages towards a phenotype that can aid in tissue regeneration,[228] however, precise

control over the duration and sequence has been challenging. Therefore, material mediated immune activity has potential to precisely guide immune response towards the enhancement of regeneration. We further assessed the abililiy of mineralized scaffolds to alter genetic phenotype of mouse macrophages (RAW) after 2 days and 4 days of culture on scaffolds. Although, the hydrogel scaffolds showed overall trend of increased IL4 (**Figure 43B1**), IL6 (**Figure 43B2**), IL10 (**Figure 43B3**), and NOS2 (**Figure 43B4**) markers, there was no difference between non-mineralized and mineralized scaffolds. This could be due to the selection of early time points.

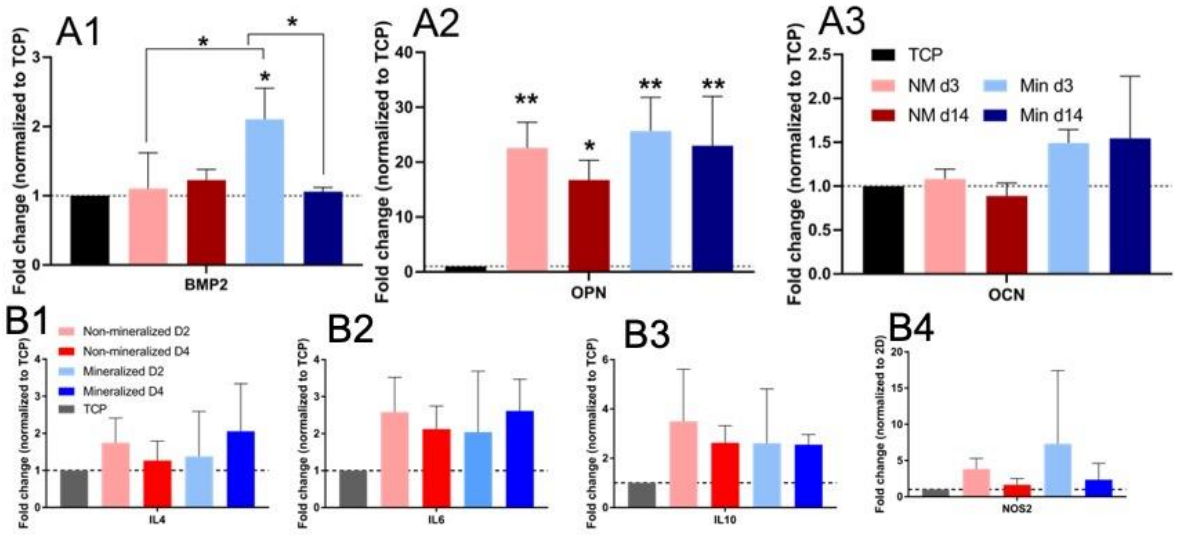

Figure 43 : qRT-PCR of osteogenic markers after 14 days of osteoblasts culture and after 2 and 4 days of macrophage culture on the scaffolds Differential mRNA expression in the form of fold change compared to TCP for mouse osteoblasts (**A1-A3**) and mouse macrophages (**B1-B4**) seeded on nonmineralized and mineralized scaffolds. A1- BMP2, A2- OPN, A3- OCN; B1-IL4, B2-IL5, B3- IL10, B4- NOS2.

Further, the OPN protein expression after 14 days of MC3T3 culture on scaffolds revealed that both the non-mineralized (**Figure 44 A1-A2**) and mineralized (**Figure 44 B1-B2**) scaffolds demonstrated OPN positive staining. OPN positive staining of osteoblasts cultured on scaffolds until day 14 correlates well with the mRNA data of OPN. Both mRNA and protein results of OPN indicate that the carrageenan by itself has potential to promote osteogenic differentiation, however,

carrageenan in combination with biomimetic minerals could marginally enhance the *in vitro* osteogenic activity of the scaffolds along the same lines as calvaria regeneration observations.

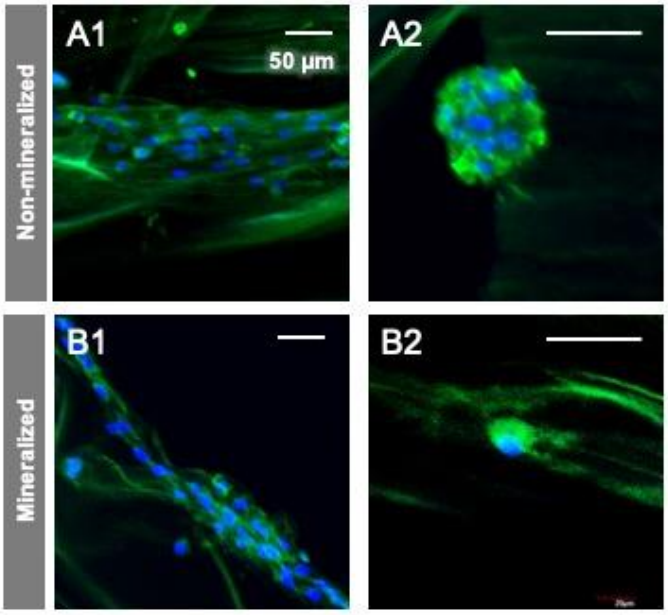

Figure 44 : Immunofluorescent staining of osteopontin after 14 days of osteoblasts culture on the scaffolds

Confocal images of osteoblasts cultured for 14-day on non-mineralized **(A1-A2**) and mineralized **(B1-B2)** scaffolds; stained with osteopontin (green) as well as Hoechst (blue).

3.4 SUMMARY

In this chapter, we demonstrated collagen-mimetic multi-scale hierarchical structure of our fibrous hydrogel scaffolds made from fibers which are a union of fibrils. Incubation of fibrous hydrogel scaffolds in SBF showed mineralization function similar to collagen in bone-ECM within as early as three days. Mineralized scaffolds showed apatite-like minerals on the surface and amorphous minerals inside after three-days of mineralization in SBF. Ten-day mineralized scaffolds showed greater extent of minerals and similar biomimetic minerals on the surface across

all three pairs of hydrogel scaffolds. CHT-KCA promoted osteogenic bioactivity to regenerate critical-sized mouse calvarial defect without the use of added growth factors. Moreover, lyophilized form of mineralized CHT-KCA was more efficacious to regenerate mouse calvaria and resulted in better healing of the tissue. We envision that our growth-factor-free and bioinspired bone graft would serve as osteoconductive as well as osteoinductive functional template to design better osteogenic biomaterials.

4 BOTTOM-UP SELF-ASSEMBLED HYDROGEL-MINERAL COMPOSITES REGENERATE RABBIT ULNA DEFECT WITHOUT ADDED GROWTH FACTORS

[Patel A, Zaky S, Li H, Schoedel K, Almarza A, Sfeir C, Sant V, Sant, S]

Submitted

4.1 BACKGROUND

Despite significant advances in material science for synthetic bone grafts, autografts remain the gold standard for large bone defect repair [229]. Autografts have been effective bone substitutes as they are non-immunogenic, histocompatible and possess indigenous bone regeneration inducing components such as growth factors. In addition to autografts, craniofacial bone repair products are largely dominated by allografts and bovine xenografts (e.g., Bio-Oss® by Geistlich Biomaterial) [230]. However, allografts necessitate secondary surgery at the site of implantation due to complications such as donor site morbidity, infection, chronic pain, and possible immunogenicity. Similar complications develop at the donor site from where the bone is harvested. Therefore, the orthopedic industry is on the lookout for surgically more feasible alternatives that stimulate progenitor bone cells to grow on the surface of the synthetic grafts and facilitate integration with the adjacent host tissue. To render the synthetic bone grafts bioactive, current approaches in the field utilize highly potent growth factors, BMP2 being the most frequently employed [231]. However, potent bioactivity of BMP2 has come under scrutiny due to its side effects, especially because of the reported continuation of bone remodeling even after the

desired bone growth is achieved and could eventually result in uncontrolled bone growth [232-234]. On the other hand, the growth factor-free approaches mostly focus on using calcium phosphate in crystalline form, sometimes mixed with collagen or other organic materials, and often result in poor osteointegration [235]. Thus, there is a clinically unmet need for a growth factor free and surgically feasible approach that can stimulate recruitment of host progenitor cells and facilitate bone regeneration and integration with the host tissue.

Synthetic bone grafts with inherent bioactivity are desirable as a safer alternative to growth factor-loaded synthetic grafts. To incorporate such bioactivity, the biomaterial is required to resemble the native tissue extracellular matrix (ECM) microenvironment. The water-rich microenvironment of hydrogels makes them ideal biomaterials mimicking the native ECM [236]. Most studies utilize hydrogel as a carrier material to deliver highly potent drug or growth factors locally [237-239]. Although biophysical properties of hydrogels can be exploited to recreate tissue microarchitecture [240], and multi-scale hierarchy[91], thereby creating a favorable biomimetic microenvironment to harness their regenerative potential, these properties remain underutilized. Albeit less potent than added growth factors, these biophysical properties stimulate favorable cellular activity to repair and regenerate the damaged tissue [241]. Natural and biodegradable biomaterials such as polysaccharides (chitosan, cellulose, glycosaminoglycans, carrageenan, etc.) have substantial overlap with native ECM properties, which include presence of microarchitecture for contact guidance, ability to serve as a growth factor reservoir, presence of electrostatic charges and functional groups to facilitate crosslinking without lethal toxicity or immunological reactions [151, 241]. These natural polysaccharides possess positive or negative charges based on their charge-imparting functional groups such as carboxylate, sulfate, or amine, which can be used for electrostatic crosslinking [150, 242]. For example, chitosan possesses

positive charge due to amine groups whereas alginic acid and carrageenan possess negative charge due to carboxylic acid and sulfate groups, respectively. When these oppositely charged polysaccharides are allowed to interact with each other in a controlled environment, they form interesting biomaterials such as bulk injectable hydrogels, beads, films, and fibers [242-245].

Another important component of synthetic bone graft is inorganic mineral phase that consists of various crystalline phases of calcium phosphate such as hydroxyapatite (HA), and beta tricalcium phosphate (β-TCP). Synthetic calcium phosphate (CaP) materials are widely used as osteoconductive components in many clinically used synthetic bone grafts such as AUGMENT®, which consists of β-TCP [246]. Several composite biomaterials with a physical blend of organic matrix and synthetic minerals have been tested and used clinically as CaP cements [247, 248]. For example, Sorrento Bone Graft Substitute (Haider Biologics LLC, San Diego, CA, USA) that consists of collagen-I and β-TCP is approved as resorbable bone void filler for clinical use. However, these blends lack the structural stability as well as multi-scale micro- and nano-architecture observed in the native ECM. This is due to the lack of molecular level interactions between the synthetic minerals and organic matrix. Such composites are often used mostly as inert space-fillers when used without potent growth factors such as recombinant BMP2.

Here, we propose ECM-mimetic bioactive materials without added growth factors that can guide and enhance tissue regeneration through the mimicry of the multi-scale architecture of bone ECM and native collagen[249]. Indeed, native collagen molecules self-assemble into triple helices, fibrils, fibers, and fiber bundles. At nano-scale, native collagen also exhibits a periodic pattern of dark/light bands that contributes to orderly mineral deposition [133]. Current synthetic materials and bone grafts fail to recapitulate these critical features of collagen such as hierarchical fibrillar structure, electrostatic charges and charged groups that are responsible for sequestration and

growth of minerals in bone ECM [133, 250]. Therefore, we exploited polyelectrolyte complexation to promote bottom-up self-assembly of oppositely charged polysaccharides at multiple length scale forming fibrils, which further assemble into fibers. We have previously demonstrated formation of collagen-mimetic single fiber through polyelectrolyte complexation between chitosan (CHT) and gellan gum (GG) using a simple microfluidic chamber [131]. We have developed this technology further into a simple yet creative fiber collection and orientation method [249] to obtain continuous aligned fibrous scaffolds with multi-scale hierarchy. We have also encapsulated electrically conductive graphene nanosheets into CHT-GG fibrous scaffolds for their application in skeletal muscle regeneration [91].

In this study, we adapted these self-assembled multi-scale fibrous hydrogels for bone tissue engineering, specifically for long bone regeneration using the critical size rabbit ulna defect model. Specifically, we employed complexation between negatively charged kappa-carrageenan (KCA) and positively charged chitosan (CHT) to form fibrous hydrogels (referred henceforth as 'RegenMatrix'). We replaced carboxylate-containing GG in our previous studies [91, 108] with sulfate-containing kappa-carrageenan (KCA) since osteogenic sulfate groups are known to sequester biomimetic minerals to boost the bioactivity towards bone regeneration, [241, 251]. The sulfate group is particularly interesting due to its role in stimulating osteogenic activity and promoting cell-matrix interaction [206, 251, 252]. Also, sulfated polysaccharides such as heparan sulfates have been shown to synergistically enhance bioactivity of BMPs by forming complexes with their negatively charged polysaccharide chains and a basic amino acid stretch in BMPs, thereby, continuously serving the ligands to their respective cell membrane receptors [206, 208]. Moreover, carrageenan exists in double helical form in its gel form, which is a key resemblance with collagen fibrils, the major organic component of bone ECM [193, 253]. CHT was chosen due

to its known role in forming mineralized matrix in crustaceous animals such as shrimp [241, 251]. To be suitable for implantation into long bone (ulna) defect, we further designed CHT-KCA RegenMatrix as cylindrical scaffolds with alternating layers of hydrogel fibers parallel and perpendicular to each other. We tested the hypothesis that multi-scale hierarchy and biomimetic mineralization observed in cylindrical CHT-KCA RegenMatrix will promote regeneration of rabbit ulna defect.

4.2 MATERIALS AND METHODS

4.2.1 Materials

Chitosan (CHT, C3646), acetic acid (695092) and the Masson's trichrome staining kit (HT15) were purchased from Sigma Aldrich Co. (St. Louis, MO). Kappa carrageenan (KCA, C41070) was obtained from Research Products International (Mt. Prospect, IL). Dulbecco's Phosphate-Buffered Saline (DPBS, 1X, 21-030CV) and Dulbecco`s Modified Eagle Media (DMEM, 1X, 10-013CV) were obtained from Corning Inc. (Corning, NY). Hematoxylin (842) and eosin (832) were obtained from Anatech LTD. (Battle Creek, MI). Bluing (CM495IW) was obtained from Cancer Diagnostics (Durham, NC).

4.2.2 Fabrication of CHT-KCA RegenMatrix

CHT (1% w/v) solution was prepared in aqueous acetic acid solution (1% w/v). KCA (1% w/v) solution was prepared in distilled water. Two programmable syringe pumps (BS300,

Braintree Scientific INC., Braintree, MA) containing CHT solution and KCA solution in separate 10mL plastic syringes were connected using Luer-lock three-way valve. The opening of the valve was connected to an 18G needle (REF305185, Becton Dickinson and Company, Franklin Lakes, NJ). The solution in both syringes was maintained at 60°C with temperature jackets (BS-SYR-H, Braintree Scientific INC., Braintree, MA). Both the pumps were set at speed of 50 mL/h. Fibers were manually collected from the tip of the needle using two 2 cm x 2 cm plastic cover slips mounted over a glass slide. The fibers were collected in four layers in such a way that top two layers were perpendicular to the two bottom layers as shown in 3D schematics in **Figure 1A**. These scaffolds were aseptically prepared using sterilized polymer solutions in a culture hood a few days before the rabbit ulna surgeries. Mineralized scaffolds were prepared by incubating dry scaffolds (before rolling) in sterile simulated body fluid (SBF) for 10 days [254]. The hydrated scaffolds (non-mineralized and mineralized) were rolled into a cylindrical spiral using pharmaceutical grade plastic films (Scotchpak 9744 Film, 70-000209164-3, 3M, Maplewood, MN) with the help of sterile twist-ties. The rolling was performed in such a way that the fibers on the outermost two layers were perpendicular to the length of the cylinder while the inner two layers were parallel to the length of the cylinder resulting in alternating layers of fibers perpendicular to each other as depicted in schematics in **Figure 1A**. The rolled scaffolds were flash frozen in liquid nitrogen and lyophilized to maintain the cylindrical structure in dried form.

4.2.3 Scanning electron microscopy (SEM)

Scaffold samples were lyophilized, and sputter coated with gold-palladium (5 nm thickness) using Cressington 108 auto sputter coater (Cressignton Scientific Instruments, UK).

SEM micrographs were obtained using JEOL 9335 Field Emission SEM (JEOL, Japan) at an accelerated voltage of 3kV and a working distance of 8 mm.

4.2.4 Cell infiltration and immunofluorescence staining

A cylindrical PDMS conduit was used to hold the cylindrical scaffold for cell infiltration studies to mimic the *in vivo* condition (**Figure 49A)**. The osteoblast precursor cells (250,000 cells per scaffold) were seeded at one end of the cylindrical scaffold and cylindrical scaffolds were incubated in DMEM supplemented with FBS (10% v/v) and penicillin/streptomycin (1% v/v) media for culturing at 37°C in 5% CO2 incubator. After 7 days, osteoblasts-seeded scaffolds were fixed using 4% paraformaldehyde for 20 min and washed three times with DPBS. The cell nuclei were stained with Hoechst 33342 (Thermo Fisher Scientific, Waltham, MA).

4.2.5 Confocal microscopy

Confocal images were acquired using inverted confocal laser scanning microscope (Olympus Fluoview 1000; Olympus Corporation, Tokyo, Japan) using 405 nm wavelength lasers. Objective lens of 20X was used for the z-stack images with 10μM thickness for each z-slice. Data are presented as maximum intensity projection of the z-stack.

4.2.6 X-ray diffraction analysis

RegenMatrix mineralized in SBF for 10 days were flash-frozen in liquid nitrogen and crushed using mortar pestle. Samples were tested in Bruker D8 Discover XRD analyzer at generator voltage of 40kV and current of 40mA.

4.2.7 Critical sized rabbit ulna defect and implantation of scaffolds

Skeletally matured New Zealand white (NZW) rabbits at least 19 weeks of age (3.5±0.2kg) were purchased from Charles River (Wilmington, Massachusetts). Rabbit ulna surgeries were performed according to a protocol approved by the University of Pittsburgh Institute of Animal Care and Use Committee. The rabbits were anaesthetized using intramuscular Ketamine (80–100 mg/kg)-Xylazine (5–10 mg/kg) injection. Critical size (16-mm) ulna defects were created in 15 New Zealand white rabbits [255]. Following the injury, sterile cylindrical scaffolds (non-mineralized or mineralized) were implanted into the defects and stabilized in place being enveloped by the muscle and subcutaneous fasciae. The periosteum was sutured back with the muscle layer (n=5 for each scaffold type). Empty defect with no scaffold served as a negative control.

4.2.8 Live and micro-computed tomography and quantification of regenerated bone volume

Live computed tomography was conducted immediately after the RegenMatrix implantation or empty control surgeries (zero-week), as well as after four and after six weeks using

Fidex X-ray system (Animage LLC, Pleasanton, CA). After 12 weeks, the radius-ulna samples were harvested and scanned using VivaCT40 (Scanco Medical AG, Bruttisellen, Switzerland) with settings: energy 55kV, intensity 142 μA, integration time of 300 msec, and isotropic voxel size of 10.5 μm. 3D reconstruction was carried out using the acquired 2D lateral projections using VivaCT40 operating software interface. Bone volume quantification analyses were performed using SkyScan DataViewer and SkyScan CTAn softwares (version 1.13.5.1) as described previously [256]. Region of interest was defined to include the defect area of bone related to the ulna while avoiding bone area related to radius. Volume of regenerated bone tissue was quantified.

4.2.9 Four point bending mechanical testing

To test the structural integrity of bony union in the ulna defect, four-point bending was performed immediately after μCT and before fixation in paraformaldehyde as described previously [257]. Briefly, in order to only measure the mechanical contribution of the ulna, the radius was transversely cut (**Figure 4A**) from each side of 16 mm defect and 4 cm apart from each cut using an Isomet low speed saw and a 0.4 mm thick diamond wafering blade (Buehler-USA). Mechanical testing was carried out using Instron 5564 (Instron-USA, 2kN load capacity). The bone was positioned as shown in **figure 4B**. The two upper (moving) loading points were 2 cm apart from each other to cover the ulna defect area (**Figure 4B**). Starting pre-load of 0.1N was applied to ensure touching of the loading points and the bone. Then the test was performed at a loading speed of 5mm/min and a stopped after 0.85mm of flexural extension. This pre-fracture threshold (0.85 mm) was determined with normal samples to avoid fracturing the sample, as they were to be processed for histological analysis. The flexural load at 0.85 mm extension was recorded for each sample.

4.2.10 Histology

Ulna samples were fixed in 10% paraformaldehyde and subsequently decalcified in ion-exchange decal unit (BioCare Medical, Pacheco, CA) for 6-8 hours after μCT imaging. The decalcified ulna samples were embedded in paraffin and subsequently sectioned along the forearm longitudinal axis using a microtome. The sections were deparaffinized and rehydrated before hematoxylin and eosin (H&E) and Mason's Trichrome staining (HT15, Sigma--Aldrich Co. (St. Louis, MO) to assess new bone formation.

4.2.11 Histomorphometry analysis

H&E and Trichrome stained samples were evaluated using light microscopy by an independent pathologist. A semi-quantitative scoring system was adapted from Seeherman *et al.* [258] to evaluate healing of the bone defect. Briefly, a score was assigned for each specimen as follows: a null score (zero) was assigned when the defect site lacked any bone or cartilage growth activity; 1 was assigned when the defect site exhibited bone growth at one or both the ends of the ulnar defect; 2 was assigned when new bone formation was observed at both the ends of the ulnar defect or showed fusion of ulna to the adjacent radius through periosteal cell activity; 3 was assigned when woven trabecular bone completely occupied the defect area; 4 was assigned when cortical continuity was present; 5 was assigned when cortical remodeling and medullary canal restoration were seen.

4.3 RESULTS AND DISCUSSSION

4.3.1 Cylindrical RegenMatrix: Fabrication, mineralization, and characterization of its fibrous and porous microarchitecture

In order to test RegenMatrix as a synthetic bone graft for long bone regeneration, cylindrical RegenMatrix with 16 mm in length and 4-5 mm in diameter was developed to match the defect dimensions of critical size rabbit ulna model using our in-house fabrication platform. The micro-architecture of fibrous RegenMatrix was designed such that the outermost layer of the cylindrical scaffold exhibited fiber direction perpendicular to the long axis of the cylinder (**Figure 45,** green) and the inside core had spiral coils with fibers parallel to the long axis of the cylinder (**Figure 45**, red). To achieve this, fibers were collected in four layers as a rectangular scaffold with fibers in the outer two layers arranged perpendicular to those in the inner two fiber layers (schematic in **Figure 45**). The four-layered rectangular scaffold was then rolled into a cylinder using pharmaceutical grade plastic sheets and twist-ties. The rolling of the scaffold created alternating layers of fibers parallel and perpendicular to each other reinforcing the overall scaffold structure and cylindrical architecture. In addition to the fibrous crisscross micro-architecture, we lyophilized these hydrogels to improve their stability during storage and transportation to the animal facility.

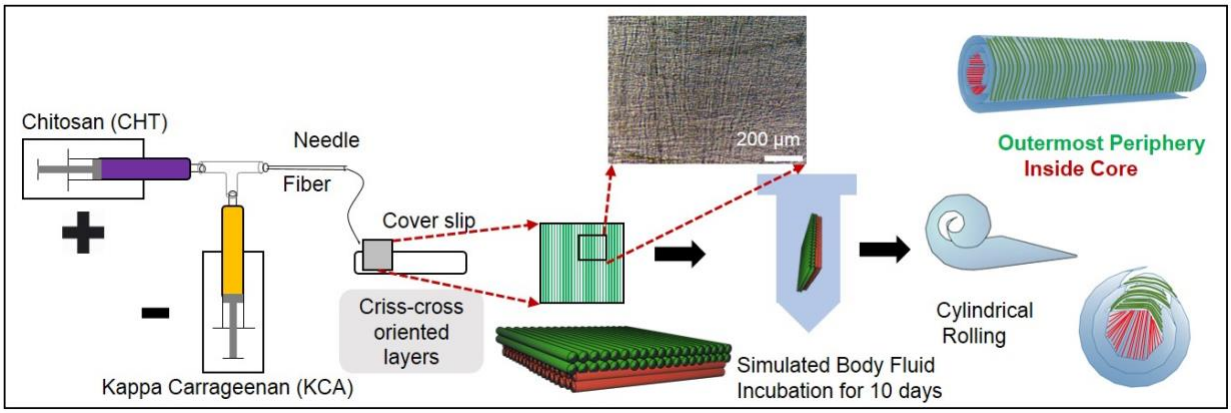

Figure 45 : Schematic of cylindrical scaffold fabrication and structural features. A schematic showing fabrication method involving two programmable syringe pumps dispensing chitosan (CHT) and kappa-carrageenan (KCA) into a two-way valve. The resultant polysaccharide complex passes through the needle forming a hanging fiber, which was collected in four layers with first two consecutive layers parallel to each other followed by next two layers perpendicular to the first two layers. These fibrous sheets were then rolled in a cylindrical spiral architecture of RegenMatrix resulting in the alternating patterns of outer layer of fibers radially concentric to the long axis (green) while inner layer of fibers was parallel to the long axis of the cylindrical scaffolds (red).

The structural stability also facilitated easy handling of cylindrical RegenMatrix in its lyophilized form, which is a significant advantage over conventional soft hydrogels. Cylindrical RegenMatrix exhibited microporous surface in lyophilized form (**Figure 46A1)** with an overall spongy texture and also exhibited excellent shape memory on compression with a pair of tweezers (**Figure 46A3 and 46A4**). Such shape memory is another important feature for surgical feasibility of tissue-engineered bone grafts. When rehydrated, cylindrical RegenMatrix swelled to form a semi-transparent cylindrical structure in hydrated form (**Figure 46A2**). Most hydrogels tend to have poor control over their architecture following rehydration [259]. Indeed, Xia *et al.* reported that crisscross gelatin-methacrylamide (GelMA) and hyaluronic acid methacrylate (HAMA) hydrogels could not retain architecture as well as mechanical strength in hydrated form [224]. Only their lyophilized, 3D printed, and photo-crosslinked hydrogel scaffolds showed retention of the

porous microarchitecture. However, RegenMatrix retained its architecture and porosity even after rehydration without any need for additional covalent crosslinking such as photocrosslinking and was easy to handle during the surgical implantation due to its fibrous crisscross architecture.

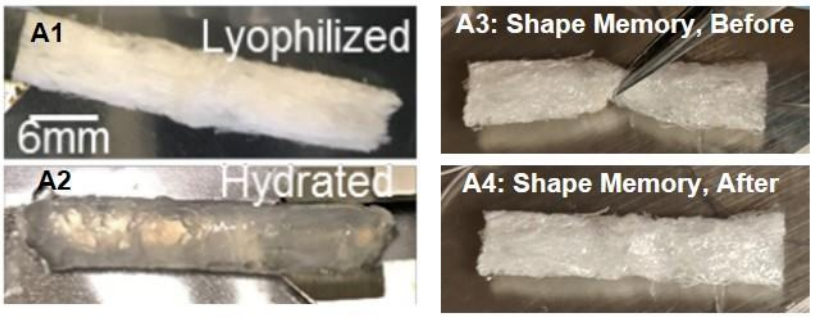

Figure 46 : Visual appearance and shape-memory of cylindrical scaffold Photographic images of the cylindrical RegenMatrix in lyophilized (**A1**) and hydrated (**A2**) form, respectively. (**A3**) Image of compressed cylindrical RegenMatrix using a pair of tweezers, (**A4**) Image of the same cylindrical RegenMatrix after regaining the original shape following the release from the tweezers.

The cylindrical RegenMatrix preserved fibrous alignment on the outer surface as shown in SEM micrographs ((**Figure 1C1)**. Magnified SEM images showed fibrous alignment along the thickness of the outer layers (**Figure 1C2**). The cross-section of cylindrical RegenMatrix along the radius exhibited the inner core with macroporous layered structure (**Figure 1C3 and 1C4**). Mineralized RegenMatrix also showed fibrous microarchitecture on the rolled layers of the cylindrical scaffold (**Figure 1D1 and 1D2**) with presence of mineral deposits on the outer surface as well as inside the scaffold forming hydrogel-mineral nanocomposite (**Figure 1D5)**. A cross-section along the radius showed the macroporous structure with presence of minerals (**Figure 1D3 and 1D4**). Magnified SEM image showed presence of mineral-RegenMatrix composite even in the inside core of the cylindrical RegenMatrix (**Figure 1D6**) similar to the ones observed on the surface (**Figure 1D5**). Since RegenMatrix was mineralized in SBF prior to rolling into cylindrical scaffolds, the minerals were uniformly present throughout the cylindrical RegenMatrix.

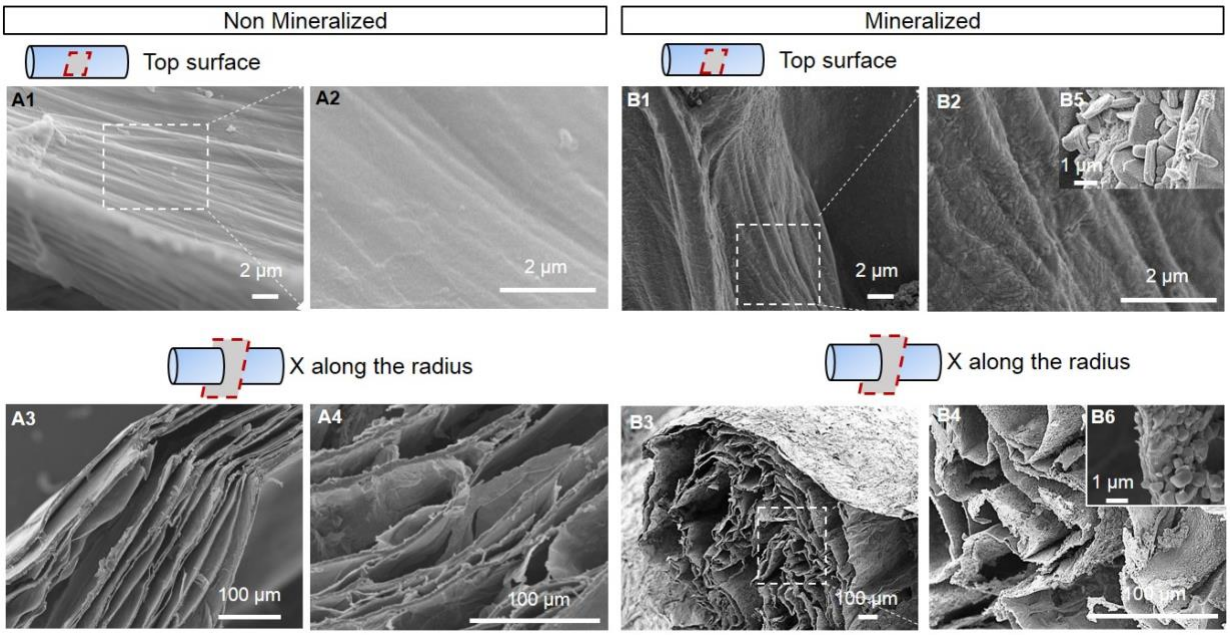

Figure 47 : Surface morphology of cylindrical scaffolds and mineral morphology of mineralized cylindrical scaffolds Low magnification (5000X) SEM images of the outer surface of the cylindrical RegenMatrix showing radially concentric fibers parallel to each other for non-mineralized **(A1)** and mineralized **(B1)**. **(A2)** High magnification (20000X) SEM image of non-mineralized RegenMatrix showing unidirectional fibrous layer. **(B2)** High magnification (20000X) SEM image of mineralized RegenMatrix showing mineral deposits on the fibrous surface. Cross-section along the radius of the cylindrical non-mineralized **(A3, A4)** and mineralized **(B3, B4)** scaffolds. High magnification images of minerals deposited on the surface **(B5)** at the center **(B6)** of the mineralized RegenMatrix.

Moreover, the XRD analysis (**Figure 48)** of deposited minerals on RegenMatrix showed similarities with previously reported carbonated apatite [202] and HA nanofibers [213] indicating that RegenMatrix promoted biomimetic biphasic nanocomposite formation. Collectively, these results demonstrated the macroporous and fibrous microarchitecture of the cylindrical RegenMatrix and uniform deposition of biomimetic minerals throughout the RegenMatrix.

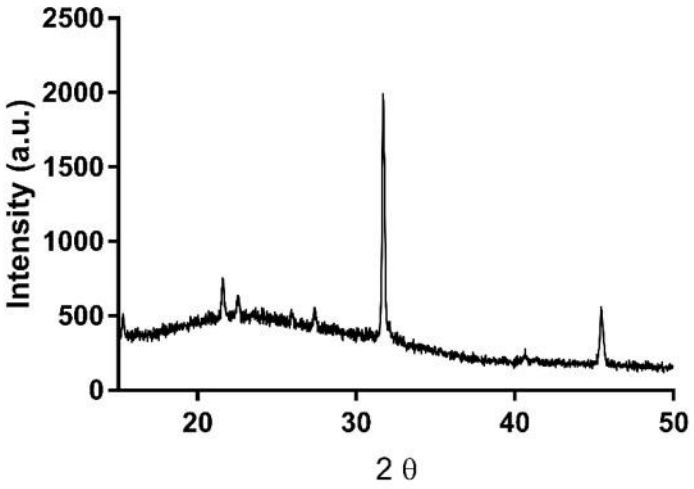

Figure 48 : XRD spectrum of mineralized CHT-KCA We then tested the ability of cells to infiltrate the cylindrical RegenMatrix *in vitro*. Cellular infiltration inside implanted acellular scaffold is an important functional feature, which determines its clinical success to ultimately regenerate the bone defect [189]. The cylindrical scaffolds were enclosed in a cylindrical PDMS conduit (**Figure 49A**) and mouse pre-osteoblasts (MC3T3) were seeded from the side by laying the cylindrical conduit on a horizontal axis (Schematic **Figure 49B)** to avoid effect of gravity on the cells seeded on the top of the cylindrical scaffolds. The PDMS conduit was used to prevent cell infiltration from other sides of the cylindrical scaffolds. Following 7 days of culture, cell nuclei were stained with Hoechst and cell distribution inside the scaffolds was observed under the confocal microscope. As shown in **figure 49B**, cells were present in the center of the scaffolds as well as at the end of the cylinder farthest from the seeding point (**Figure 49C**) indicating that the cylindrical RegenMatrix promoted infiltration of mouse pre-osteoblasts. Such cell infiltration throughout the cylindrical RegenMatrix could be attributed to the presence of surface roughness and nano-topography (fibrils/fibers), which are known to play an important role at the initial stage of cell-material interaction such as native cell attachment as well as in the later stages when implant integrates with the native tissue [260]. Moreover, anisotropic

microarchitecture of the scaffolds with integrated bioinspired features such as fibrous alignment and multi-scale hierarchy have been shown to provide contact guidance using various hydrogel and electrospun fibrous scaffolds [82, 131, 261, 262].

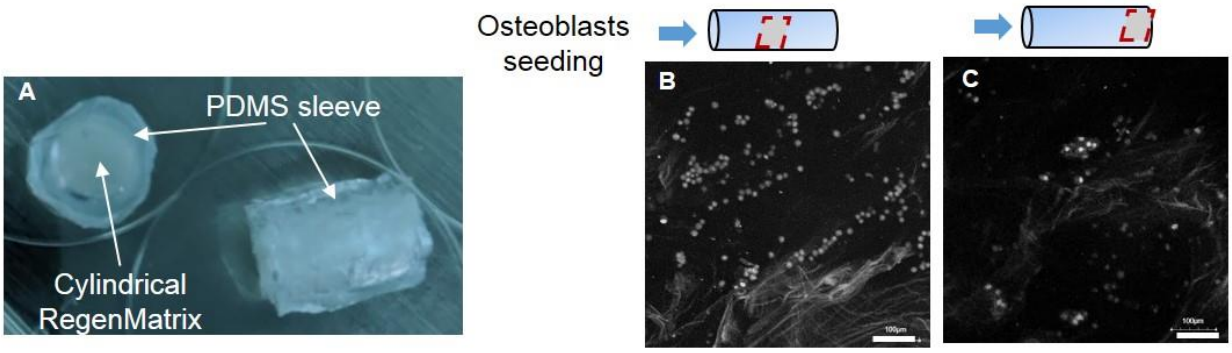

Figure 49 : MC3T3 cell infiltration in cylindrical scaffolds.A shows two cylindrical RegenMatrix inside separate PDMS sleeves set in different orientation. The white core is cylindrical RegenMatrix prior to cell seeding and the shiny and transparent periphery is PDMS mold. Infiltration of osteoblasts (nuclei stained and represented in monochromatic images) in the middle of the cylindrical scaffold **(B)**. Infiltration of osteoblasts to the farthest from seeding point in the cylindrical scaffold **(C)**; Schematic on the top depicts the area of scaffold for B and C.

Together, we demonstrated that RegenMatrix scaffolds mineralized in SBF showed uniform mineral deposits throughout the scaffolds. Further, non-mineralized and mineralized scaffolds could be rolled into cylinders and maintained their structural integrity in both lyophilized and hydrated forms. Finally, the fibrous microarchitecture of cylindrical RegenMatrix could have played important role in infiltration of mouse pre-osteoblasts throughout the scaffolds.

4.3.2 Mineralized cylindrical RegenMatrix enhanced bone regeneration in rabbit ulna defect

We next tested the potential of cylindrical RegenMatrix processed as either non-mineralized (as prepared) or mineralized scaffolds to promote long bone regeneration using a

critical size rabbit ulna defect model. This semi-load-bearing rabbit ulna defect model provides a unique opportunity to implant and test hydrogel materials for bone regeneration since an intact radius has the advantage of bearing the load on itself [263]. New Zealand white rabbits were conditioned for ulna defect surgeries. Intact ulna prior to creating the defect is shown in **Figure 50A1**. The sixteen mm length of ulna (yellow box) was marked and removed (**Figure 50A2**). Lyophilized cylindrical RegenMatrix (non-mineralized or mineralized, n=5 each) was implanted in the defect area as shown in **Figure 50A3.** Following the implantation of RegenMatrix, fascia was sutured to provide fixation of RegenMatrix in the defect site.

Figure 50 : Surgical implantation of cylindrical scaffolds in rabbit ulna defect.

(**A1**) Rabbit ulna prior to creating the defect, (**A2**) Critical size (16 mm) ulna defect, and (**A3**) after implantation of RegenMatrix in the ulna defect.

To follow the progress of bone regeneration over time, base-line (0-week) live CT was performed on the rabbits in all three treatment groups (empty defect, non-mineralized and mineralized) immediately after implantation to record the area of the empty ulna defect in each animal (time 0) irrespective of the treatment group (**Figure 51A1, 51B1, and 51C1**). Live CT images revealed an early onset of ulna regeneration starting as early as 4 weeks in all three treatment groups (**Figure 51A2, 51B2, and 52C2**). The empty ulna defect has been shown to be inconsistent study control as it self-regenerates, although not to the same extent as study conditions [264]. For example, Yu *et al.* showed almost unionized regenerated μCT images of empty control, although the regenerated bone volume was not reported for empty defect controls since these were

excluded from the quantification [264]. In our study, the non-mineralized (**Figure 51B3**) and mineralized RegenMatrix (**Figure 51C3**) showed enhanced bone regeneration at six weeks as compared to the empty defect group (**Figure 51A3**). Moreover, bone growth in the empty defect was disorganized as compared to bone growth in the RegenMatrix groups.

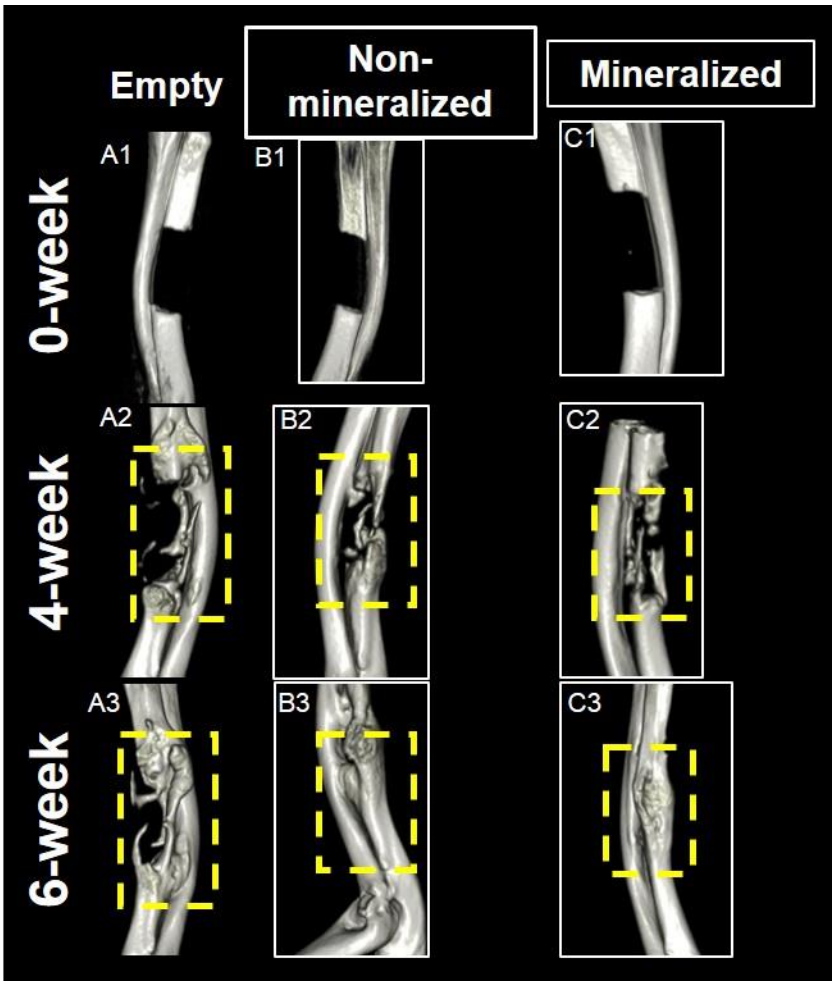

Figure 51 :Live-CT images of ulna defect after 0-week, 4-week, and 6-week of implantation.

A1-A3 show live CT images of empty ulna defect from 0-week to 6-week. Likewise, B1-B3 show corresponding live CT images of non-mineralized group and C1-C3 show corresponding live CT images of mineralized group

Twelve weeks following the implantation surgeries, the group with empty defects showed bone regeneration to some extent in most of the rabbits as seen in μCT images (**Figure 52A1-A5**, defect area highlighted with yellow dotted box). However, only two of the five rabbits showed

bony union (**Figure 52A2, 2A4**). Moreover, most rabbits showed disorganized regenerated bone, with the exception of one rabbit in the empty defect group (**Figure 52A4**), which showed self-regeneration of the empty bone defect. In the non-mineralized RegenMatrix treatment group, three out of five rabbits showed bony union (**Figure 52B1, B3, B5)**. Similarly, mineralized RegenMatrix treatment promoted bony union in three out of five rabbits (**Figure 52C2, C4, and C5**). All rabbits in non-mineralized and mineralized RegenMatrix treatment groups with bony unions showed organized structure of regenerated ulna unlike the empty defect group. Further quantification of regenerated bone volume from the μCT scans revealed significantly higher bone volume in the mineralized RegenMatrix treatment group compared to the empty defect group as shown in **Figure 53**. Collectively, these results show greater potential of mineralized RegenMatrix to promote organized bone regeneration compared to the empty defect. This could be due to the collective effect of multi-scale hierarchical architecture of scaffolds, presence of sulfated polysaccharide KCA and mineral-rich microenvironment in the mineralized RegenMatrix due to deposition of biomimetic minerals. Indeed, recent studies have shown that a calcium phosphate-rich microenvironment comprising both amorphous and crystalline forms of apatite play crucial role in promoting osteoinduction [211, 265]. Indeed, mineralized RegenMatrix exhibit crystalline apatite on the surface while amorphous CaP inside the scaffolds (unpublished data). Therefore, it is also possible that the release of calcium and phosphate ions may be responsible for enhanced osteogenic potential of mineralized RegenMatrix. Moreover, sulfated polysaccharides similar to KCA have shown to improve osteogenic activity. For example, Cao *et al.* successfully demonstrated synergistic osteoinductive and osteoconductive potential of sulfated chitosan nanoparticles loaded in rhBMP2 containing gelatin hydrogels, which promoted greater bone growth in the rabbit radius defect [266]. The same research group have previously reported the

osteogenic activity of sulfated chitosan using an ectopic bone formation model in mice, however, their rabbit radius defect study excluded sulfated chitosan and gelatin control, which could be directly relevant to our non-mineralized CHT-KCA [207]. The improved regeneration of the radius was attributed to controlled release of rhBMP2 rather than the osteogenic activity of sulfated chitosan. Therefore, drawing a direct conclusion regarding osteogenic activity of sulfated chitosan is difficult from this study.

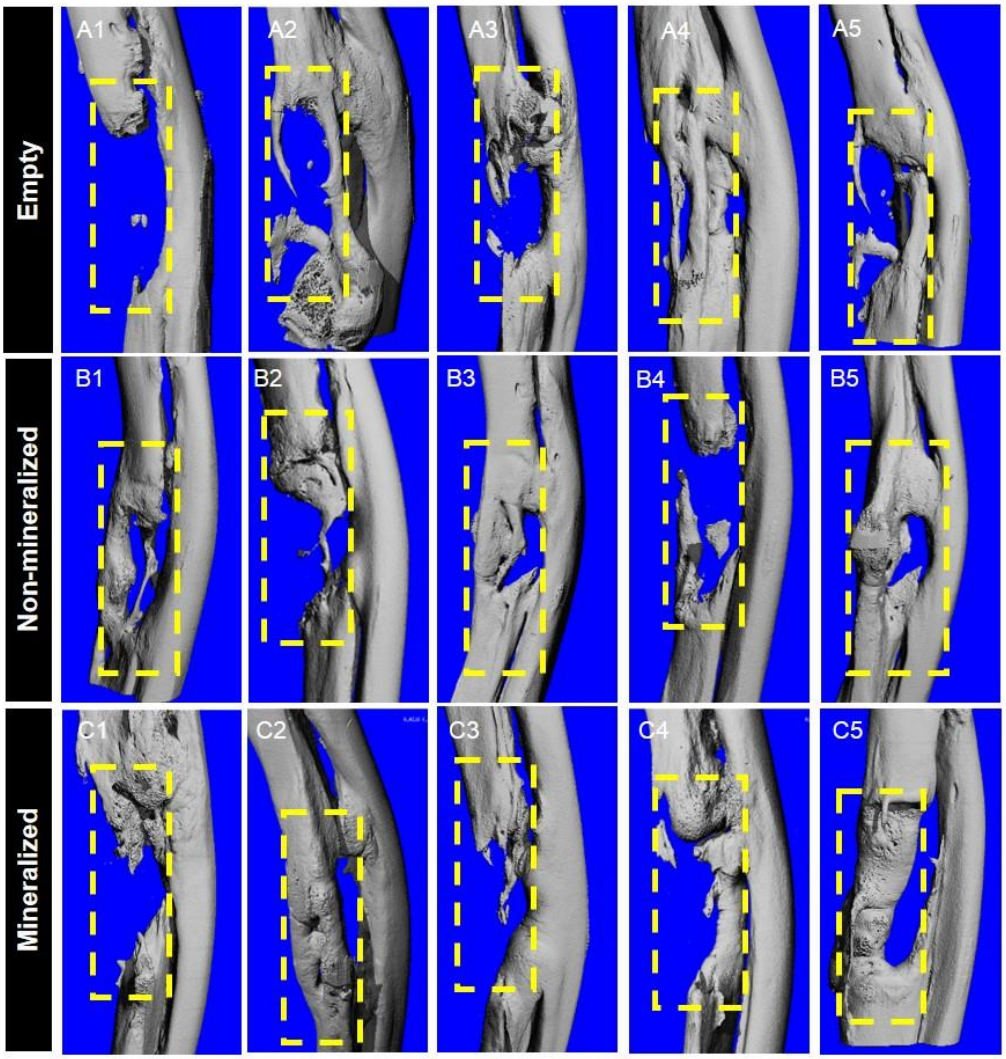

Figure 52 : 3D reconstructed Micro-CT images of regenerated rabbit ulna after 12 weeks of implantation of cylindrical scaffolds. 3D reconstructed □CT images after 12 weeks of surgeries showing regeneration of ulna defect

for empty defect (**A1-A5**), non-mineralized RegenMatrix (**B1-B5**), and mineralized RegenMatrix (**C1-C5**), respectively.

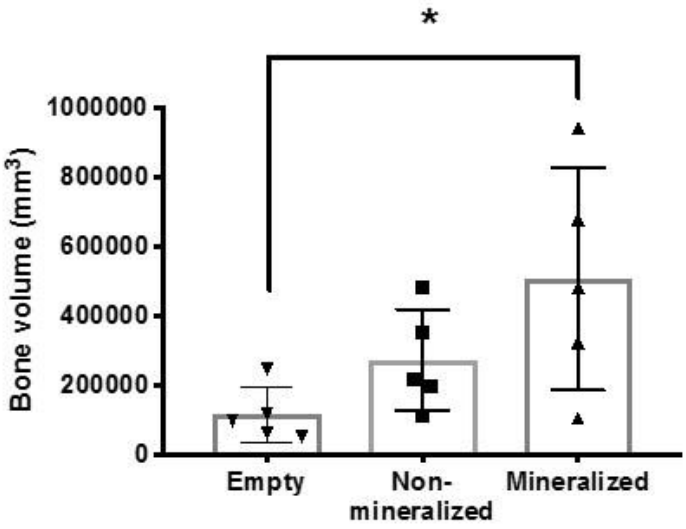

Figure 53 : Regenerated rabbit ulna bone volume from micro-CT analysis.

Quantification of regenerated bone volume using CTAnalyser software (Bruker). * indicates statistical significance ($p<0.05$) compared to empty defect; One-way ANOVA; Error bars: standard error of mean; n=5 rabbits/group.

Further, we performed histology on the regenerated defect area to evaluate the quality of the regenerated bone. Both trichome (**Figure 54A1, 54B1, 54C1**) and H&E (**Figure 54A2, 54B2, 54C2**) staining images are shown. Three regions of interest were identified as 1) region with periosteal activity (color-coded as green box) where radius interfaces with the defected ulna, 2) region in the middle of the defect (color-coded as purple box), and 3) region covering the boundary of the native ulna and defect margin (color-coded as yellow box). Treatment group with empty defect (control, **Figure 54A1-A2**) showed limited bone growth. A detailed evaluation of the region with periosteal activity (green) showed absence of periosteal fibroblasts (**Figure 54A3-A4**). The region in the middle of the defect (purple region) showed woven bone at one of the ends of the defect along with histiocytes in the nearby marrow space (**Figure 54A5-A6**); however, there was no bone or cartilage in the boundary region of the native ulna and the defect (boundary between

native old bone (OB) and new regenerated bone (NB) demarcated with white dotted line) (**Figure 54A7-54A8**).

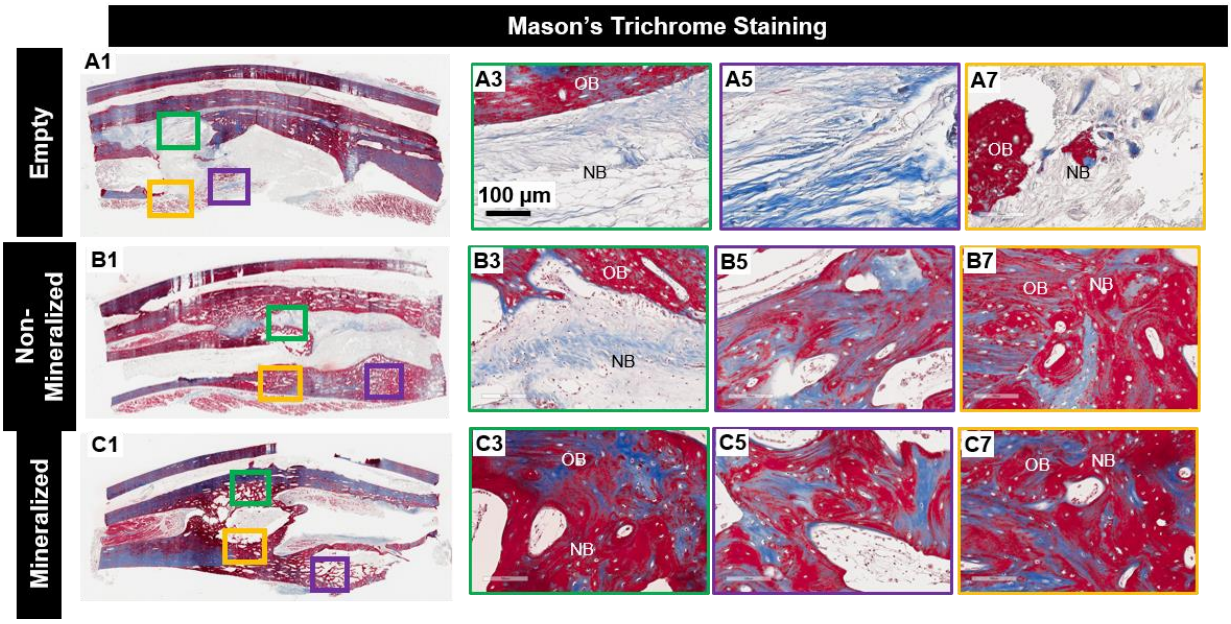

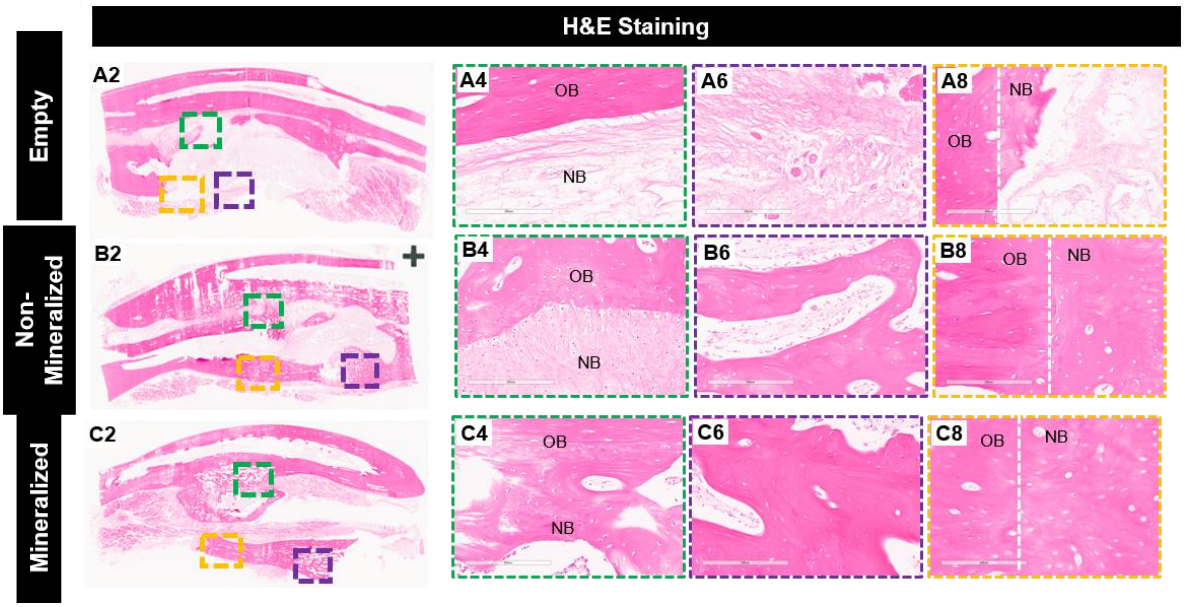

Table 1

Qualitative Observations	Region with periosteal activity (Green)	Region in the middle of the defect (Purple)	Region covering the boundary of the native ulna and the defect (Yellow)
Empty	No periosteal fibroblasts.	Woven bone present at one end of the defect. Histiocytes in marrow space adjacent to normal bone.	No bone or cartilage present.
Non-mineralized	Increased cellularity on ulnar surface. Mononuclear cells and neutrophils in aggregates in marrow space of radius and ulna.	Immature bone present between Haversian systems, continuity present.	Immature bone present, not completely remodeled. Clear demarcation between new bone and native ulna.
Mineralized	Endochondral ossification with a bony mass. Histocytes, marrow elements present.	Immature bone still present but Haversian systems well formed, More mature bone.	Clear demarcation between woven and mature bone present. Longer lamellae on non defect side (More organized collagen)

Table 2

Quantitative H-score	Region in the middle of the defect (Purple)	Region covering the boundary of the native ulna and the defect (Yellow)	Average H-score
Empty	1	1	1
Non-mineralized	4	4	4
Mineralized	5	5	5

Figure 54: Histological evaluation and histomorphometry for regenerated rabbit ulna. (A1, B1, and C1) Mason's Trichrome stained stitched images of longitudinal section of control (empty defect), non-mineralized, mineralized rabbits, respectively; **(A2, B2, C2)** Similar H&E stained stitched image of longitudinal section of control (empty defect), non-mineralized, mineralized rabbits, respectively;

(A3-A4, B3-B4, C3-C4) Magnified images from periosteal activity region are indicated in green boxes for control, non-mineralized, and mineralized rabbits, respectively. **(B5-B8, C5-C8, D5-D8)** Similar images from the middle of the defect area and at the start of the defect area are shown in purple and yellow boxes, respectively. Solid lined boxes are used to indicate Mason's Trichrome stained images and dotted lined boxes are used for H&E stained images.

(Table 1) Qualitative evaluation of H&E and Mason's Trichrome stained longitudinal sections of radius and ulna from three different regions (yellow, green, and purple boxes) from the defect area. **(Table 2)** Healing score (H-score) of the same sections from two different regions from the defect area as indicated in the schematic above the table. NB- new bone, OB- old native bone.

Based on the overall morphology and organization of regenerated bone, quantification of the healing score (H-Score) of the purple and yellow regions in the empty defect group indicated an average score of 1 out of 5 **(Table 2, Figure 54)**. The treatment group with non-mineralized RegenMatrix (**Figure 54B1-54B2**) showed more bone and cartilage in the regenerated areas as well as higher degree of bony union of regenerated bone with the native bone as compared to the empty defect group. The periosteal activity region (green) showed increased cellularity at the regenerated ulnar defect region indicating an active role of periosteal cells in the new bone

formation (**Figure 54B3-54B4**). The middle region of the defect (purple box) contained immature bone between Haversian systems with continuity indicating active bone formation orchestrated by presence of implanted non-mineralized RegenMatrix (**Figure 54B5-54B6**). Moreover, the region encompassing the boundary between the native ulna and the defect (yellow box) showed immature bone yet to be remodeled resulting in clear demarcation between regenerated NB and the native OB (boundary marked by white dotted line, **Figure 54B7-54B8**). The non-mineralized RegenMatrix group received an average H-score of 4 out of 5 (**Table 2, Figure 54**). Interestingly, the treatment group with mineralized RegenMatrix (**Figure 54C1 to C8**) showed predominantly organized mature bone with little or no cartilage indicating faster transformation into mature bone as compared to non-mineralized RegenMatrix. Further, the region of periosteal activity (green box) showed evidence of endochondral ossification with a bony mass (**Figure 54C3-54C4**) indicating that the bone in this region has undergone relatively rapid transformation from cartilage as compared to the other two study groups. The middle region in the defect area (purple box) showed immature bone similar to non-mineralized RegenMatrix; however, the Haversian systems were well formed (**Figure 54C5-54C6**). Additionally, the maturity of bone in this region was highest among the three treatment conditions. The yellow region showed longer lamellae on the non-defect side with more organized collagen showing a clear demarcation between woven and mature bone (**Figure 54C7-54C8**). Mineralized RegenMatrix implanted defect promoted regeneration with a H-score of 5 out of 5.

Osteointegration is another success criterion important for clinically viable bone graft substitutes. The implanted scaffold should integrate well with the surrounding native bone tissue for functional success of the regenerated bone [267, 268]. Such osteointegration depends on several factors such as adhesion, differentiation, and mineralization of osteoblast precursor cells.

In order to prevent collapse or creep of the ulna, native subchondral bone must bond with the implanted scaffold during the initial few weeks of implantation. Rabbits used in this study were not sacrificed earlier than 12 weeks; therefore, we could not perform histological analysis to confirm early osteointegration in presence of the scaffolds. However, integration of regenerated ulna with native ulna at 12 weeks could be readily observed as evident from the distinct boundary in H&E images of the non-mineralized RegenMatrix groups (white dotted line, **Figure 54B8**) possibly suggesting a role of osteoconductive RegenMatrix. The mineralized RegenMatrix, on the other hand, showed comparatively better osteointegration evidenced by relatively less distinct boundary between native old and regenerated new bone in H&E images of mineralized RegenMatrix (white dotted line, **Figure 54C8**) compared to the non-mineralized counterpart. This was reflected in H-scores of 4 and 5 out of 5 for non-mineralized and mineralized RegenMatrix, respectively. Some of the non-mineralized and mineralized groups also showed fusion of regenerated ulna with native radius due to radius periosteal activity for new ulna regeneration. The perfect H-score of mineralized RegenMatrix could be attributed to our biomimetic mineralization approach that led to uniform mineral deposition throughout the scaffold (**Figure 47B5, 47B6**), which may have further enhanced osteoconductive activity and even may have promoted osteoinductive properties of the RegenMatrix. Thus, the biomimetic bone microenvironment created by the presence of minerals, together with microporous aligned fibrous network may have resulted in better regeneration of mature bone in the mineralized RegenMatrix group.

A previous study that utilized PGS scaffolds showed that the ulna regeneration was mainly due to the periosteal activity [269]. Moreover, the study group, which received implants consisting of PGS and HA exhibited chondrocyte activity and cartilage formation similar to RegenMatrix. However, the bone regeneration due to PGS-HA was not sufficient to result in regenerated bone

union. On the other hand, in case of the RegenMatrix, bone growth from either endosteal activity or bone marrow clearly was evident in the live CT images (**Figure 51**). Thus, the observed bone growth could have resulted from the bone marrow (*i.e.* the boundary of the defect), endosteum (*i.e.*, inner surface of ulna where defect was created), or the periosteum (*i.e.* from the intact radius side). This could be due to synergistic effects of fibrous contact guidance and the presence of biomimetic calcium phosphate minerals in addition to osteogenic potential of the sulfate-containing KCA [206, 208, 252]. Additionally, presence of cartilage transforming into mature bone (**Figure 3C3-C5**) also suggested endochondral ossification as the underlying mechanism.

4.3.3 Cylindrical RegenMatrix improved mechanical strength of regenerated ulna defect

To measure the functional mechanical strength, we performed four-point bending test on the regenerated radius-ulna bones that were harvested at the end of 12 weeks. A threshold was decided based on the previous study [257]. Radius was cut using a saw as shown in **Figure 4A** (points 1 and 2). This enabled us to avoid contribution of radius in the mechanical testing. The bone was mounted on the four-point bending test apparatus as shown in **figure 4B**. **Figure 4C** shows the maximum flexure load endured by the regenerated ulna. Although non-mineralized and mineralized RegenMatrix showed greater average flexure load, it was not statistically significant when compared to the empty defect group. Lack of statistically significant change across different treatment groups can be attributed to the biological variation among rabbits in the same treatment conditions. The fusion of regenerated ulna with the native radius could be another source for variation. Despite cutting the intact radius from the joints on both sides, this variation was difficult to eliminate. Total sample size required to achieve statistically significant effect (α error = 0.05,

80% power) was found to be 27 rabbits (n=9/treatment group) instead of 15 rabbits (n=5) used in our study. This was calculated using data from four-point bending test.

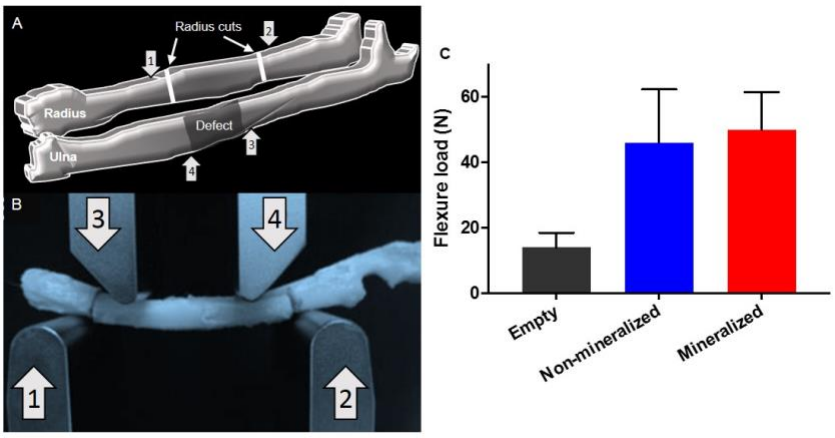

Figure 55 : Four-point bending test of regenerated rabbit ulna. Schematic shows radius and ulna of the rabbit with cuts in radius (points 1 and 2) and darker shaded area shows the ulnal defect (points 3 and 4). Numbers on the bone are correlated to four-point bending mechanical tester stress points in **A**. **(B)** Quantification of maximum flexure load (N). Error bars: standard error of mean; n=5 rabbits/group. No statistical significance was found when empty group was compared with experimental groups using one-way ANOVA.

In summary, RegenMatrix exhibited a great promise as a biomaterial that can regenerate long bone defect without the use of any added growth factors.

4.3.4 Summary

In this study, we developed self-assembled cylindrical hydrogel based RegenMatrix with fibrous multi-scale architecture. We demonstrated that microfluidic self-assembly followed by mineralization and rolling resulted in robust cylindrical RegenMatrix with excellent retention of the multi-scale architecture and uniform mineral deposition throughout the scaffolds. RegenMatrix, in both non-mineralized and mineralized forms enhanced bone regeneration in the

semi-load bearing critical size rabbit ulna defect when compared to the empty defect. RegenMatrix also showed greater histocompatibility without any fibrous tissue formation, which may be attributed to its biocompatible polysaccharide constituents. Histomorphometry analysis demonstrated that the ulna regeneration could be due to endochondral ossification. Collectively, the RegenMatrix developed in this study has a great potential as a bioactive bone graft.

5 CONCLUSIONS AND FUTURE PERSPECTIVE

5.1 MAJOR CONCLUSIONS

Hydrogels have gained popularity as biomaterial due to their water-rich microenvironment for cells. After the advancement of fabrication technologies which can control multiple length-scale structural features, pioneering leaders in hydrogel field such as Langer, Peppas, and Khademhosseini have expanded the horizon for hydrogel application for the release of active moiety as well as tissue regeneration. In the last decade, biomaterial research focus including hydrogels has shifted towards mimicking physical aspects of natural extracellular matrix (ECM) to recreate microarchitecture and even sub-micron structural cues to trick the native cells into embryonic development. Recent studies have been focused on true mimicry of structural and physical aspects to engineer natural bioactivity in the hydrogels.

Hydrogel bone grafts are of particular interest as commonly used substitute bone graft in clinic is made of collagen hydrogel combined with rhBMP2. Due to safety concerns related to off label uses of these bone grafts, leading firms in orthopedic industry are on the lookout for better alternatives. After the discovery of BMP2 by Marshall Urist in in 1965 and first approval by FDA in 2001, BMPs have been proven as potent inducer of bone regeneration in numerous *in vitro* and *in vivo* studies. Therefore, the scope of innovation lies with the engineering of its release and reduction of its dose complimented by other biologic or a carrier hydrogel with bioactivity of its own. Several studies have tried to chemically engineer the release of BMPs but for my dissertation, I have focused on the bioinspired design of carrier hydrogel with its own bioactivity.

Few recent studies have attempted to delve into this area and design hydrogel mixed with bone-minerals to form composites. However, they show limited influence on the local microenvironment at the bone injury site *in vivo* to elicit osteogenic response. This is majorly due to heavy focus on resembling bone composition and ignoring the intricate multi-scale hierarchical structure of the bone forming composites between organic matrix and inorganic minerals. Unfortunately, these aspects are challenging to incorporate due to technological challenges in fabrication of bone grafts.

I approached this scientific challenge by focusing on mimicry of bone ECM from sub-micron to centimeter scale through interfacial polyionic complexation (IPC) phenomenon first reported by Amaike and colleagues in 1998. Although there are various IPC related studies reported after 1998, it has been never employed for bone graft development. In chapter 2, I reported automated fabrication method for of three types of fibrous hydrogel scaffolds made from bottom-up self-assembly of oppositely charged polysaccharides. It was exhibited that the fibrous hydrogel scaffolds possess collagen-mimetic multi-scale structural features. Moreover, the versatility of this fabrication technology to fabricate fibrous hydrogel scaffolds with various architecture as well as to encapsulate small molecules and nanoparticles was demonstrated. In chapter 4, I assessed the bioactivity of these hydrogel scaffolds *in vitro* and in mouse calvarial defect. It was found that all three different compositions of hydrogel scaffolds promoted biomimetic apatite minerals on the surface and amorphous minerals inside *in vitro* in simulated body fluid (SBF). Through implantation of hydrogel scaffolds in non-load-bearing critical-sized mouse calvarial defect, it was found that the hydrogel scaffolds showed promising osteogenic activity, however, it was far from complete closure of the defect. It was further improved to incorporate biomimetic minerals from SBF mineralization and implanted in lyophilized form which demonstrated significantly better

calvaria defect closure. In chapter 5, I designed cylindrical form of the hydrogel scaffolds and evaluated their efficacy to regenerated critical-sized semi-load-bearing defect in rabbit ulna. It was exhibited that the cylindrical hydrogel scaffolds showed excellent osteogenic activity and led to complete bridging in 3 out of 5 rabbits with in both non-mineralized and mineralized form. Moreover, through histological tissue assessment, it was found that the bone tissue healing was excellent without any irreversible inflammation complication. Moreover, the hydrogel fabrication technology and hydrogel scaffolds are widely tunable to incorporate other moieties or various constituents for not just bone tissue engineering but other tissue regeneration applications as well.

5.2 STUDY LIMITATIONS

The reported studies have several limitations. This section will describe major limitations of each research chapter.

In chapter 2, the collagen-mimetic multi-scale structures of our hydrogel scaffolds were limited to qualitative mimicry of the features and assembly. We did not benchmark the sub-micron features as well as the mechanical strength of the fibers to match with collagen fibers.

In chapter 3, we characterized minerals deposited on the surface and inside hydrogel scaffolds using various physicochemical characterization techniques, however, we did not perform elemental analysis of the mineral-hydrogel composites which is often reported in similar studies in the field. Additionally, calcium and phosphate release has been reported to influence osteogenic potential of the bone graft, however, we did not characterize the release and its kinetics. Moreover, many studies in this area correlate the *in vitro* SBF studies with *in vitro* cell culture studies, however, we did not assess mineral deposition bioactivity in the

presence of pre-osteoblast or stem cells. Our cell culture studies were limited to qRT-PCR and immunofluorescence for selective gene and protein markers. Our mice studies had limited number of mice per group (n=5) which is far from achieving true power of statistical tests with only two time points. Moreover, bone radiographs of the defect at zero time point was not recorded which could quantify variation in surgical defect creation. Also, the characterization of new bone was limited to image analysis whereas most studies in the field also report regenerated bone volume.

In chapter 4, our cylindrical scaffolds showed cellular infiltration, however, their metabolic activity for extended culture period was not studied. We used only 5 rabbits per condition which did not allow for true power of statistical tests. Moreover, some studies in the area report regenerated bone density, however we only reported regenerated bone volume.

Lastly, our studies did not assess degradation profile of our fibrous hydrogel scaffolds as well as the compatibility of the degradation products. Although we reported promising proof-of-concept data on the efficacy of fibrous hydrogel scaffolds, the temporal link between degradation of the hydrogels and quantification of bone growth could provide a more reliable understanding of the osteogenic activity of hydrogel scaffolds.

Collectively, this left scope for important unanswered questions such as when did the hydrogel scaffold degrade? Until when did the mineralized hydrogel scaffold release calcium phosphate at the injury site? These questions will motivate future researchers to explore this area and the limitations will guide future researchers to plan improved future studies.

5.3 FUTURE DIRECTIONS

The research studies and perspective reported in this dissertation creates opportunities for more advanced explorations in tissue engineering areas especially in the design of substitute bone grafts. This section is focused on discussion about continuation of this work and then about some long-term implications on substitute bone graft field.

First, automated collector design can be further improved with smaller and less bulky parts and the fiber collection can be customized to produce fibers with complex 3D shapes. Moreover, the encapsulation of nanoparticles, small molecules, and proteins can be optimized further by a detailed characterization of the interaction between the hydrogel scaffold and the encapsulants. Additionally, polysaccharides can be purified, and a precise molecular weight variant can be used for a precise correlation between theoretical and experimental loading of encapsulants. The raw materials (polysaccharides) used can be chemically modified to introduce linkers for selective binding of the encapsulant and cleavage by bodily enzymes to sustain the release. Moreover, electrostatically charged synthetic polymers can be used to replace natural polysaccharides or can be additional to polysaccharides reported in this dissertation. This can advance material properties and offer greater control over fabrication due to homologous polymer chains.

These are the only hydrogel biomaterial reported to have collagen-mimetic multi-scale hierarchy on self-assembly. Therefore, single hydrogel fiber and hydrogel scaffolds offer potential for multiple tissue engineering applications as collagen is part of most of the tissue ECM.

The osteogenic activity of the hydrogel scaffold can be investigated in detail by partially blocking calcium receptors from the cells to check if the calcium ions released from the mineralized hydrogel scaffold were the osteogenic driver. Moreover, alkaline phosphatase activity of mesenchymal stem cells seeded on mineralized scaffolds incubated in SBF for different duration

can be studied. Additionally, macrophages are known to be the first responder cells following implantation of biomaterials in bone injury and their reactivity to the material can determine the direction of inflammation. Specifically, M2 type of macrophages are known to aid in regeneration and healing of the defect. Therefore, the effect of mineralized scaffolds on macrophage phenotype can be characterized for time points beyond day 4. It can be investigated if macrophage reactivity towards mineralized hydrogel scaffolds can be induced further for synergistic osteogenic activity for mesenchymal stem cells. These results can help re-engineer the hydrogel scaffolds with added cytokines to recruit and genetically engineer to M2 phenotype for improved osteogenic bioactivity.

Cell therapy is gaining interest in the orthopedic and pharmaceutical industry. *In vivo* osteogenic activity of our hydrogel scaffolds can be further improved by combining the scaffolds pre-seeded mesenchymal stem cells. This will overcome low potency of bioinspired approach and help accelerate bone regeneration still keeping the approach 'growth-factor-free'. The variation among the bone regeneration performance observed in rabbit implantation studies (Chapter 4) could reduce as the crucial first step to depend on cell recruitment by the scaffold will be removed.

rhBMP2 still remains widely used clinical treatment options. Therefore, potential of our hydrogel scaffolds as a carrier for rhBMP2 should be tested. Negative charge and sulfate groups from carrageenan can provide inherent advantage for sustained release of rhBMP2 as they are known to interact electrostatically. The rhBMP2 release from our hydrogel scaffolds should be studied and adjusted for sustained release for initial 2-3 weeks. Further, a similar mouse or rabbit study can be designed with different doses of rhBMP2 to assess the synergistic effect of rhBMP2 and our hydrogel scaffolds.

We reported efficacy of hydrogel scaffolds in non-load-bearing and semi-load-bearing bone defect models. Long term-goal should be to also design a mechanically strong bone graft

with soft hydrogel core for easy infiltration of mesenchymal cells. This can be achieved by identifying a partner polymer or metal that is resorbable in matching timeframe with degradation of hydrogels. This can be further tested in femur defect model in large animals.

In conclusion, the results of this dissertation enriched tissue engineering and hydrogel formulation field with novel design, fabrication, and bioinspired characteristics of this osteogenic hydrogel scaffolds.

6 REFERENCES

1. Boyce, T., J. Edwards, and N. Scarborough, *Allograft bone. The influence of processing on safety and performance.* Orthop Clin North Am, 1999. **30**(4): p. 571-81.
2. Johnell, O. and J.A. Kanis, *An estimate of the worldwide prevalence and disability associated with osteoporotic fractures.* Osteoporosis International, 2006. **17**(12): p. 1726-1733.
3. Harada, S. and G.A. Rodan, *Control of osteoblast function and regulation of bone mass.* Nature, 2003. **423**(6937): p. 349-55.
4. Lee, K. and S.B. Goodman, *Current state and future of joint replacements in the hip and knee.* Expert Rev Med Devices, 2008. **5**(3): p. 383-93.
5. Kaiser, M.G., et al., *Guideline update for the performance of fusion procedures for degenerative disease of the lumbar spine. Part 17: bone growth stimulators as an adjunct for lumbar fusion.* J Neurosurg Spine, 2014. **21**(1): p. 133-9.
6. Laurencin, C., Y. Khan, and S.F. El-Amin, *Bone graft substitutes.* Expert Rev Med Devices, 2006. **3**(1): p. 49-57.
7. DeCoster, T.A., et al., *Management of posttraumatic segmental bone defects.* J Am Acad Orthop Surg, 2004. **12**(1): p. 28-38.
8. Summers, B.N. and S.M. Eisenstein, *Donor site pain from the ilium. A complication of lumbar spine fusion.* J Bone Joint Surg Br, 1989. **71**(4): p. 677-80.
9. Arrington, E.D., et al., *Complications of iliac crest bone graft harvesting.* Clin Orthop Relat Res, 1996(329): p. 300-9.
10. Yunus Basha, R., T.S. Sampath Kumar, and M. Doble, *Design of biocomposite materials for bone tissue regeneration.* Mater Sci Eng C Mater Biol Appl, 2015. **57**: p. 452-63.
11. Hoppe, A., N.S. Gueldal, and A.R. Boccaccini, *A review of the biological response to ionic dissolution products from bioactive glasses and glass-ceramics.* Biomaterials, 2011. **32**(11): p. 2757-2774.
12. Bauer, T.W. and J. Schils, *The pathology of total joint arthroplasty - II. Mechanisms of implant failure.* Skeletal Radiology, 1999. **28**(9): p. 483-497.
13. Ramazanoglu, M., et al., *The effect of combined delivery of recombinant human bone morphogenetic protein-2 and recombinant human vascular endothelial growth factor 165 from biomimetic calcium-phosphate-coated implants on osseointegration.* Clin Oral Implants Res, 2011. **22**(12): p. 1433-9.
14. Pap, T., et al., *Osteoclast-independent bone resorption by fibroblast-like cells.* Arthritis Research & Therapy, 2003. **5**(3): p. R163-R173.
15. Vale, F.M., et al., *Acrylic bone cement induces the production of free radicals by cultured human fibroblasts.* Biomaterials, 1997. **18**(16): p. 1133-5.
16. Amini, A.R., J.S. Wallace, and S.P. Nukavarapu, *Short-term and long-term effects of orthopedic biodegradable implants.* J Long Term Eff Med Implants, 2011. **21**(2): p. 93-122.
17. Agarwal, R. and A.J. Garcia, *Biomaterial strategies for engineering implants for enhanced osseointegration and bone repair.* Advanced Drug Delivery Reviews, 2015. **94**: p. 53-62.

18. Fischer, C.R., et al., *A systematic review of comparative studies on bone graft alternatives for common spine fusion procedures.* European Spine Journal, 2013. **22**(6): p. 1423-1435.
19. Duarte, R.M., et al., *Biomaterials and Bioactive Agents in Spinal Fusion.* Tissue Engineering Part B-Reviews, 2017. **23**(6): p. 540-551.
20. Vo, T.N., F.K. Kasper, and A.G. Mikos, *Strategies for controlled delivery of growth factors and cells for bone regeneration.* Advanced Drug Delivery Reviews, 2012. **64**(12): p. 1292-1309.
21. Carragee, E.J., E.L. Hurwitz, and B.K. Weiner, *A critical review of recombinant human bone morphogenetic protein-2 trials in spinal surgery: emerging safety concerns and lessons learned.* Spine J, 2011. **11**(6): p. 471-91.
22. Chrastil, J., et al., *Complications associated with the use of the recombinant human bone morphogenetic proteins for posterior interbody fusions of the lumbar spine.* Spine (Phila Pa 1976), 2013. **38**(16): p. E1020-7.
23. Illi, O.E. and C.P. Feldmann, *Stimulation of fracture healing by local application of humoral factors integrated in biodegradable implants.* Eur J Pediatr Surg, 1998. **8**(4): p. 251-5.
24. Li, L., et al., *Controlled dual delivery of BMP-2 and dexamethasone by nanoparticle-embedded electrospun nanofibers for the efficient repair of critical-sized rat calvarial defect.* Biomaterials, 2015. **37**: p. 218-29.
25. Han, X., et al., *Accelerated postero-lateral spinal fusion by collagen scaffolds modified with engineered collagen-binding human bone morphogenetic protein-2 in rats.* PLoS One, 2014. **9**(5): p. e98480.
26. Street, J., et al., *Vascular endothelial growth factor stimulates bone repair by promoting angiogenesis and bone turnover.* Proc Natl Acad Sci U S A, 2002. **99**(15): p. 9656-61.
27. Yang, Y.Q., et al., *The role of vascular endothelial growth factor in ossification.* Int J Oral Sci, 2012. **4**(2): p. 64-8.
28. DeLong, J.M., R.P. Russell, and A.D. Mazzocca, *Platelet-rich plasma: the PAW classification system.* Arthroscopy, 2012. **28**(7): p. 998-1009.
29. Marques, L.F., et al., *Platelet-rich plasma (PRP): methodological aspects and clinical applications.* Platelets, 2015. **26**(2): p. 101-13.
30. Alsousou, J., et al., *The biology of platelet-rich plasma and its application in trauma and orthopaedic surgery: a review of the literature.* J Bone Joint Surg Br, 2009. **91**(8): p. 987-96.
31. Marx, R.E., et al., *Platelet-rich plasma: Growth factor enhancement for bone grafts.* Oral Surg Oral Med Oral Pathol Oral Radiol Endod, 1998. **85**(6): p. 638-46.
32. Marx, R.E., *Platelet-rich plasma (PRP): what is PRP and what is not PRP?* Implant Dent, 2001. **10**(4): p. 225-8.
33. Tilkeridis, K., et al., *Use of demineralized bone matrix in spinal fusion.* World J Orthop, 2014. **5**(1): p. 30-7.
34. Peterson, B., et al., *Osteoinductivity of commercially available demineralized bone matrix. Preparations in a spine fusion model.* J Bone Joint Surg Am, 2004. **86**(10): p. 2243-50.
35. Aghdasi, B., et al., *A review of demineralized bone matrices for spinal fusion: the evidence for efficacy.* Surgeon, 2013. **11**(1): p. 39-48.

36. Buser, Z., et al., *Allograft Versus Demineralized Bone Matrix in Instrumented and Noninstrumented Lumbar Fusion: A Systematic Review.* Global Spine Journal, 2018. **8**(4): p. 396-412.
37. Campana, V., et al., *Bone substitutes in orthopaedic surgery: from basic science to clinical practice.* J Mater Sci Mater Med, 2014. **25**(10): p. 2445-61.
38. Basha, R.Y., T.S.S. Kumar, and M. Doble, *Design of biocomposite materials for bone tissue regeneration.* Materials Science & Engineering C-Materials for Biological Applications, 2015. **57**: p. 452-463.
39. Sell, S.A., et al., *The Use of Natural Polymers in Tissue Engineering: A Focus on Electrospun Extracellular Matrix Analogues.* Polymers, 2010. **2**(4): p. 522-553.
40. Pannone, P.J., *Trends in biomaterials research*. 2007, New York: Nova Science Publishers. x, 244 p.
41. Miyata, T., T. Taira, and Y. Noishiki, *Collagen engineering for biomaterial use.* Clin Mater, 1992. **9**(3-4): p. 139-48.
42. Saito, W., et al., *Acceleration of bone formation during fracture healing by injectable collagen powder and human basic fibroblast growth factor containing a collagen-binding domain from Clostridium histolyticum collagenase.* J Biomed Mater Res A, 2014. **102**(9): p. 3049-55.
43. Nashchekina, Y.A., et al., *Effect of Concentration of Collagen Gel on Functional Activity of Bone Marrow Mesenchymal Stromal Cells.* Bull Exp Biol Med, 2017. **163**(1): p. 123-128.
44. Chamieh, F., et al., *Accelerated craniofacial bone regeneration through dense collagen gel scaffolds seeded with dental pulp stem cells.* Sci Rep, 2016. **6**: p. 38814.
45. Jianqi, H., et al., *Comparison of calcium alginate film with collagen membrane for guided bone regeneration in mandibular defects in rabbits.* J Oral Maxillofac Surg, 2002. **60**(12): p. 1449-54.
46. Abid, W.K. and Y.H. Al Mukhtar, *Repair of surgical bone defects grafted with hydroxylapatite + beta-TCP combined with hyaluronic acid and collagen membrane in rabbits: A histological study.* J Taibah Univ Med Sci, 2019. **14**(1): p. 14-24.
47. Toosi, S., et al., *Bone defect healing is induced by collagen sponge/polyglycolic acid.* J Mater Sci Mater Med, 2019. **30**(3): p. 33.
48. Durham, E.L., et al., *Optimizing bone wound healing using BMP2 with absorbable collagen sponge and Talymed nanofiber scaffold.* J Transl Med, 2018. **16**(1): p. 321.
49. Hosseinkhani, H., et al., *Bone regeneration on a collagen sponge self-assembled peptide-amphiphile nanofiber hybrid scaffold.* Tissue Eng, 2007. **13**(1): p. 11-9.
50. Shen, X., et al., *A novel method for the fabrication of homogeneous hydroxyapatite/collagen nanocomposite and nanocomposite scaffold with hierarchical porosity.* Journal of Materials Science-Materials in Medicine, 2011. **22**(2): p. 299-305.
51. Sotome, S., et al., *Synthesis and in vivo evaluation of a novel hydroxyapatite/collagen-alginate as a bone filler and a drug delivery carrier of bone morphogenetic protein.* Materials Science & Engineering C-Biomimetic and Supramolecular Systems, 2004. **24**(3): p. 341-347.
52. Gentile, P., et al., *Polymeric membranes for guided bone regeneration.* Biotechnol J, 2011. **6**(10): p. 1187-97.

53. Lee, E.J., et al., *Collagen-silica xerogel nanohybrid membrane for guided bone regeneration.* Journal of Biomedical Materials Research Part A, 2012. **100A**(4): p. 841-847.
54. Ferreira, A.M., et al., *Collagen for bone tissue regeneration.* Acta Biomaterialia, 2012. **8**(9): p. 3191-3200.
55. Pohunkova, H. and M. Adam, *Reactivity and the fate of some composite bioimplants based on collagen in connective tissue.* Biomaterials, 1995. **16**(1): p. 67-71.
56. Kane, R.J., et al., *Hydroxyapatite reinforced collagen scaffolds with improved architecture and mechanical properties.* Acta Biomater, 2015. **17**: p. 16-25.
57. Vats, A., et al., *Scaffolds and biomaterials for tissue engineering: a review of clinical applications.* Clin Otolaryngol Allied Sci, 2003. **28**(3): p. 165-72.
58. Francis, L., et al., *Simultaneous electrospin-electrosprayed biocomposite nanofibrous scaffolds for bone tissue regeneration.* Acta Biomaterialia, 2010. **6**(10): p. 4100-4109.
59. Barbani, N., et al., *Hydroxyapatite/gelatin/gellan sponges as nanocomposite scaffolds for bone reconstruction.* Journal of Materials Science-Materials in Medicine, 2012. **23**(1): p. 51-61.
60. Hamlekhan, A., et al., *Preparation of laminated poly(epsilon-caprolactone)-gelatin-hydroxyapatite nanocomposite scaffold bioengineered via compound techniques for bone substitution.* Biomatter, 2011. **1**(1): p. 91-101.
61. Liu, X., et al., *Biomimetic nanofibrous gelatin/apatite composite scaffolds for bone tissue engineering.* Biomaterials, 2009. **30**(12): p. 2252-2258.
62. Leeuwenburgh, S.C., et al., *Mineralization, biodegradation, and drug release behavior of gelatin/apatite composite microspheres for bone regeneration.* Biomacromolecules, 2010. **11**(10): p. 2653-9.
63. Yunos, D.M., O. Bretcanu, and A.R. Boccaccini, *Polymer-bioceramic composites for tissue engineering scaffolds.* Journal of Materials Science, 2008. **43**(13): p. 4433-4442.
64. Chen, G.Q. and Q. Wu, *The application of polyhydroxyalkanoates as tissue engineering materials.* Biomaterials, 2005. **26**(33): p. 6565-6578.
65. Sadat-Shojai, M., et al., *Nano-hydroxyapatite reinforced polyhydroxybutyrate composites: A comprehensive study on the structural and in vitro biological properties.* Materials Science & Engineering C-Materials for Biological Applications, 2013. **33**(5): p. 2776-2787.
66. Saadat, A., et al., *Comparison of acellular and cellular bioactivity of poly 3-hydroxybutyrate/hydroxyapatite nanocomposite and poly 3-hydroxybutyrate scaffolds.* Biotechnology and Bioprocess Engineering, 2013. **18**(3): p. 587-593.
67. Saska, S., et al., *Bacterial Cellulose-Hydroxyapatite Nanocomposites for Bone Regeneration.* International Journal of Biomaterials, 2011.
68. Bhumiratana, S., et al., *Nucleation and growth of mineralized bone matrix on silk-hydroxyapatite composite scaffolds.* Biomaterials, 2011. **32**(11): p. 2812-2820.
69. Madihally, S.V. and H.W.T. Matthew, *Porous chitosan scaffolds for tissue engineering.* Biomaterials, 1999. **20**(12): p. 1133-1142.
70. Di Martino, A., M. Sittinger, and M.V. Risbud, *Chitosan: A versatile biopolymer for orthopaedic tissue-engineering.* Biomaterials, 2005. **26**(30): p. 5983-5990.
71. Rubert, M., et al., *Effect of alginate hydrogel containing polyproline-rich peptides on osteoblast differentiation.* Biomedical Materials, 2012. **7**(5): p. 055003.

72. Stevens, L.R., et al., *Tissue engineering with gellan gum.* Biomaterials Science, 2016. **4**(9): p. 1276-1290.
73. Douglas, T.E.L., et al., *Injectable self-gelling composites for bone tissue engineering based on gellan gum hydrogel enriched with different bioglasses.* Biomed Mater, 2014. **9**(4): p. 045014.
74. Yegappan, R., et al., *Carrageenan based hydrogels for drug delivery, tissue engineering and wound healing.* Carbohydrate Polymers, 2018. **198**: p. 385-400.
75. Giuffre, A.J., et al., *Polysaccharide chemistry regulates kinetics of calcite nucleation through competition of interfacial energies.* Proc Natl Acad Sci U S A, 2013. **110**(23): p. 9261-6.
76. Dinoro, J., et al., *Sulfated polysaccharide-based scaffolds for orthopaedic tissue engineering.* Biomaterials, 2019. **214**.
77. Song, J.M., et al., *Comparative study of chitosan/fibroin-hydroxyapatite and collagen membranes for guided bone regeneration in rat calvarial defects: micro-computed tomography analysis.* International Journal of Oral Science, 2014. **6**(2): p. 87-93.
78. Fernandez, T., et al., *Effects of Calcium Phosphate/Chitosan Composite on Bone Healing in Rats: Calcium Phosphate Induces Osteon Formation.* Tissue Engineering Part A, 2014. **20**(13-14): p. 1948-1960.
79. Senni, K., et al., *Marine Polysaccharides: A Source of Bioactive Molecules for Cell Therapy and Tissue Engineering.* Marine Drugs, 2011. **9**(9): p. 1664-1681.
80. Dimassi, S., et al., *Sulfonated and sulfated chitosan derivatives for biomedical applications: A review.* Carbohydrate Polymers, 2018. **202**: p. 382-396.
81. Hintze, V., et al., *Sulfated Glycosaminoglycans Exploit the Conformational Plasticity of Bone Morphogenetic Protein-2 (BMP-2) and Alter the Interaction Profile with Its Receptor.* Biomacromolecules, 2014. **15**(8): p. 3083-3092.
82. Zhang, Y.S. and A. Khademhosseini, *Advances in engineering hydrogels.* Science, 2017. **356**(6337).
83. Djabourov, M., J. Leblond, and P. Papon, *GELATION OF AQUEOUS GELATIN SOLUTIONS .2. RHEOLOGY OF THE SOL-GEL TRANSITION.* Journal De Physique, 1988. **49**(2): p. 333-343.
84. Gasperini, L., J.F. Mano, and R.L. Reis, *Natural polymers for the microencapsulation of cells.* Journal of the Royal Society Interface, 2014. **11**(100).
85. Zhang, S.G., *Fabrication of novel biomaterials through molecular self-assembly.* Nature Biotechnology, 2003. **21**(10): p. 1171-1178.
86. Rich, A. and F.H.C. Crick, *STRUCTURE OF COLLAGEN.* Nature, 1955. **176**(4489): p. 915-916.
87. O'Leary, L.E.R., et al., *Multi-hierarchical self-assembly of a collagen mimetic peptide from triple helix to nanofibre and hydrogel.* Nature Chemistry, 2011. **3**(10): p. 821-828.
88. Hartgerink, J.D., E. Beniash, and S.I. Stupp, *Self-assembly and mineralization of peptide-amphiphile nanofibers.* Science, 2001. **294**(5547): p. 1684-8.
89. Braccini, I. and S. Perez, *Molecular basis of Ca2+-induced gelation in alginates and pectins: The egg-box model revisited.* Biomacromolecules, 2001. **2**(4): p. 1089-1096.
90. Morton, S.W., et al., *Scalable Manufacture of Built-to-Order Nanomedicine: Spray-Assisted Layer-by-Layer Functionalization of PRINT Nanoparticles.* Advanced Materials, 2013. **25**(34): p. 4707-4713.

91. Patel, A., et al., *Hierarchically aligned fibrous hydrogel films through microfluidic self-assembly of graphene and polysaccharides.* Biotechnology and Bioengineering, 2018. **115**(10): p. 2654-2667.
92. Hennink, W.E. and C.F. van Nostrum, *Novel crosslinking methods to design hydrogels.* Advanced Drug Delivery Reviews, 2002. **54**(1): p. 13-36.
93. Azagarsamy, M.A. and K.S. Anseth, *Bioorthogonal Click Chemistry: An Indispensable Tool to Create Multifaceted Cell Culture Scaffolds.* Acs Macro Letters, 2013. **2**(1): p. 5-9.
94. Annabi, N., et al., *Highly Elastic and Conductive Human-Based Protein Hybrid Hydrogels.* Advanced Materials, 2016. **28**(1): p. 40-+.
95. Bai, X., et al., *Bioactive hydrogels for bone regeneration.* Bioactive Materials, 2018. **3**(4): p. 401-417.
96. Moshaverinia, A., et al., *Encapsulated dental-derived mesenchymal stem cells in an injectable and biodegradable scaffold for applications in bone tissue engineering.* Journal of Biomedical Materials Research Part A, 2013. **101**(11): p. 3285-3294.
97. Sugaya, S., et al., *Microfluidic production of single micrometer-sized hydrogel beads utilizing droplet dissolution in a polar solvent.* Biomicrofluidics, 2013. **7**(5).
98. Yamada, M., et al., *Microfluidic synthesis of chemically and physically anisotropic hydrogel microfibers for guided cell growth and networking.* Soft Matter, 2012. **8**(11): p. 3122-3130.
99. Vinogradov, S.V., T.K. Bronich, and A.V. Kabanov, *Nanosized cationic hydrogels for drug delivery: preparation, properties and interactions with cells.* Advanced Drug Delivery Reviews, 2002. **54**(1): p. 135-147.
100. Fujioka-Kobayashi, M., et al., *Cholesteryl group- and acryloyl group-bearing pullulan nanogel to deliver BMP2 and FGF18 for bone tissue engineering.* Biomaterials, 2012. **33**(30): p. 7613-7620.
101. Themistocleous, G.S., et al., *Implants of type I collagen gel containing MG-63 osteoblast-like cells can act as stable scaffolds stimulating the bone healing process at the sites of the surgically-produced segmental diaphyseal defects in male rabbits.* In Vivo, 2007. **21**(1): p. 69-76.
102. Zara, J.N., et al., *High Doses of Bone Morphogenetic Protein 2 Induce Structurally Abnormal Bone and Inflammation In Vivo.* Tissue Engineering Part A, 2011. **17**(9-10): p. 1389-1399.
103. Shekaran, A., et al., *Bone regeneration using an alpha 2 beta 1 integrin-specific hydrogel as a BMP-2 delivery vehicle.* Biomaterials, 2014. **35**(21): p. 5453-5461.
104. Shirakura, T., et al., *Matrix Density Engineering of Hydrogel Nanoparticles with Simulation-Guided Synthesis for Tuning Drug Release and Cellular Uptake.* Acs Omega, 2017. **2**(7): p. 3380-3389.
105. Wang, Z.M., et al., *Novel biomaterial strategies for controlled growth factor delivery for biomedical applications.* Npg Asia Materials, 2017. **9**.
106. Barati, D., et al., *Spatiotemporal release of BMP-2 and VEGF enhances osteogenic and vasculogenic differentiation of human mesenchymal stem cells and endothelial colony-forming cells co-encapsulated in a patterned hydrogel.* J Control Release, 2016. **223**: p. 126-136.
107. Guvendiren, M. and J.A. Burdick, *Engineering synthetic hydrogel microenvironments to instruct stem cells.* Current Opinion in Biotechnology, 2013. **24**(5): p. 841-846.

108. Sant, S., et al., *Self-Assembled Hydrogel Fiber Bundles from Oppositely Charged Polyelectrolytes Mimic Micro-/Nanoscale Hierarchy of Collagen.* Advanced Functional Materials, 2017.
109. Ignatova, M., et al., *Electrospun Non-Woven Nanofibrous Hybrid Mats Based on Chitosan and PLA for Wound-Dressing Applications.* Macromolecular Bioscience, 2009. **9**(1): p. 102-111.
110. Wan, A.C.A., et al., *Fibers by interfacial polyelectrolyte complexation - processes, materials and applications.* Materials Today, 2016. **19**(8): p. 437-450.
111. Hu, M., et al., *Hydrodynamic spinning of hydrogel fibers.* Biomaterials, 2010. **31**(5): p. 863-869.
112. Lin, H.Y., C.W. Peng, and W.W. Wu, *Fibrous hydrogel scaffolds with cells embedded in the fibers as a potential tissue scaffold for skin repair.* Journal of Materials Science-Materials in Medicine, 2014. **25**(1): p. 259-269.
113. Cheng, J., et al., *Electrospinning versus microfluidic spinning of functional fibers for biomedical applications.* Biomaterials, 2017. **114**: p. 121-143.
114. Yao, C.H., et al., *Electrospun Poly(gamma(-)glutamic acid)/beta(-)Tricalcium Phosphate Composite Fibrous Mats for Bone Regeneration.* Polymers (Basel), 2019. **11**(2).
115. Lee, K., et al., *Bone regeneration via novel macroporous CPC scaffolds in critical-sized cranial defects in rats.* Dent Mater, 2014. **30**(7): p. e199-207.
116. Amaike, M., Y. Senoo, and H. Yamamoto, *Sphere, honeycomb, regularly spaced droplet and fiber structures of polyion complexes of chitosan and gellan.* Macromolecular Rapid Communications, 1998. **19**(6): p. 287-289.
117. Yamamoto, H., et al., *Polyion complex fiber and capsule formed by self-assembly of poly-L-lysine and gellan at solution interfaces.* Journal of Applied Polymer Science, 2001. **79**(3): p. 437-446.
118. Wan, A.C.A., et al., *Mechanism of fiber formation by interfacial polyelectrolyte complexation.* Macromolecules, 2004. **37**(18): p. 7019-7025.
119. McNamara, M.C., et al., *Microfibers as Physiologically Relevant Platforms for Creation of 3D Cell Cultures.* Macromolecular Bioscience, 2017. **17**(12).
120. Wan, A.C.A., et al., *Encapsulation of biologics in self-assembled fibers as biostructural units for tissue engineering.* Journal of Biomedical Materials Research Part A, 2004. **71A**(4): p. 586-595.
121. Wang, F., et al., *Multi-Colored Fibers by Self-Assembly of DNA, Histone Proteins, and Cationic Conjugated Polymers.* Angewandte Chemie-International Edition, 2014. **53**(2): p. 424-428.
122. Ohkawa, K., et al., *Polyion complex fiber and capsule formed by self-assembly of chitosan and poly(alpha,L-glutamic acid) at solution interfaces.* Macromolecular Materials and Engineering, 2001. **286**(3): p. 168-175.
123. Granero, A.J., et al., *Spinning Carbon Nanotube-Gel Fibers Using Polyelectrolyte Complexation.* Advanced Functional Materials, 2008. **18**(23): p. 3759-3764.
124. Rui, J., et al., *Controlled release of vascular endothelial growth factor using poly-lactic-co-glycolic acid microspheres: In vitro characterization and application in polycaprolactone fumarate nerve conduits.* Acta Biomaterialia, 2012. **8**(2): p. 511-518.

125. King, T.W. and C.W. Patrick, *Development and in vitro characterization of vascular endothelial growth factor (VEGF)-loaded poly(DL-lactic-co-glycolic acid)/poly(ethylene glycol) microspheres using a solid encapsulation/single emulsion/solvent extraction technique.* Journal of Biomedical Materials Research, 2000. **51**(3): p. 383-390.
126. Sun, Q.H., et al., *Sustained vascular endothelial growth factor delivery enhances angiogenesis and perfusion in ischemic hind limb.* Pharmaceutical Research, 2005. **22**(7): p. 1110-1116.
127. Murua, A., et al., *Cell microencapsulation technology: Towards clinical application.* Journal of Controlled Release, 2008. **132**(2): p. 76-83.
128. Liao, I.C., et al., *Controlled release from fibers of polyelectrolyte complexes.* Journal of Controlled Release, 2005. **104**(2): p. 347-358.
129. Wan, A.C.A., et al., *Multicomponent Fibers by Multi-interfacial Polyelectrolyte Complexation.* Advanced Healthcare Materials, 2012. **1**(1): p. 101-105.
130. Yim, E.K., et al., *Proliferation and differentiation of human mesenchymal stem cell encapsulated in polyelectrolyte complexation fibrous scaffold.* Biomaterials, 2006. **27**(36): p. 6111-22.
131. Sant, S., et al., *Self-Assembled Hydrogel Fiber Bundles from Oppositely Charged Polyelectrolytes Mimic Micro-/Nanoscale Hierarchy of Collagen.* Advanced Functional Materials, 2017: p. 1606273 (1-10).
132. Brett, E., et al., *Biomimetics of Bone Implants: The Regenerative Road.* Bioresearch Open Access, 2017. **6**(1): p. 1-6.
133. Landis, W.J., *An overview of vertebrate mineralization with emphasis on collagen-mineral interaction.* Gravit Space Biol Bull, 1999. **12**(2): p. 15-26.
134. Beniash, E., *Biominerals—hierarchical nanocomposites: the example of bone.* Wiley Interdisciplinary Reviews: Nanomedicine and Nanobiotechnology, 2011. **3**(1): p. 47-69.
135. Ottani, V., M. Raspanti, and A. Ruggeri, *Collagen structure and functional implications.* Micron, 2001. **32**(3): p. 251-260.
136. Tzaphlidou, M., *The role of collagen in bone structure: An image processing approach.* Micron, 2005. **36**(7–8): p. 593-601.
137. Olszta, M.J., et al., *Bone structure and formation: A new perspective.* Materials Science and Engineering: R: Reports, 2007. **58**(3–5): p. 77-116.
138. Rho, J.Y., L. Kuhn-Spearing, and P. Zioupos, *Mechanical properties and the hierarchical structure of bone.* Med Eng Phys, 1998. **20**(2): p. 92-102.
139. Wopenka, B. and J.D. Pasteris, *A mineralogical perspective on the apatite in bone.* Materials Science & Engineering C-Biomimetic and Supramolecular Systems, 2005. **25**(2): p. 131-143.
140. Kuhn, L.T., *Bone Mineralization*, in *Encyclopedia of Materials: Science and Technology*, K.H.J. Buschow, et al., Editors. 2001, Elsevier: Oxford. p. 787-794.
141. Berendsen, A.D. and B.R. Olsen, *Bone development.* Bone, 2015. **80**: p. 14-18.
142. Einhorn, T.A. and L.C. Gerstenfeld, *Fracture healing: mechanisms and interventions.* Nat Rev Rheumatol, 2015. **11**(1): p. 45-54.
143. Deschaseaux, F., L. Sensebe, and D. Heymann, *Mechanisms of bone repair and regeneration.* Trends in Molecular Medicine, 2009. **15**(9): p. 417-429.

144. Lee, F.Y., et al., *Programmed removal of chondrocytes during endochondral fracture healing.* J Orthop Res, 1998. **16**(1): p. 144-50.
145. Gerstenfeld, L.C., et al., *Impaired fracture healing in the absence of TNF-alpha signaling: the role of TNF-alpha in endochondral cartilage resorption.* J Bone Miner Res, 2003. **18**(9): p. 1584-92.
146. Bueno, E.M. and J. Glowacki, *Cell-free and cell-based approaches for bone regeneration.* Nature Reviews Rheumatology, 2009. **5**(12): p. 685-697.
147. C. Duarte, A.R., et al., *Recent Developments on Chitosan Applications in Regenerative Medicine*, in *Biomaterials from Nature for Advanced Devices and Therapies*. 2016, John Wiley & Sons, Inc. p. 221-243.
148. Voron'ko, N.G., et al., *Formation of kappa-carrageenan-gelatin polyelectrolyte complexes studied by H-1 NMR, UV spectroscopy and kinematic viscosity measurements.* Carbohydrate Polymers, 2016. **151**: p. 1152-1161.
149. Bidarra, S.J., C.C. Barrias, and P.L. Granja, *Injectable alginate hydrogels for cell delivery in tissue engineering.* Acta Biomater, 2014. **10**.
150. Yamanlar, S., et al., *Surface functionalization of hyaluronic acid hydrogels by polyelectrolyte multilayer films.* Biomaterials, 2011. **32**(24): p. 5590-9.
151. Rabanel, J.M., et al., *Polysaccharide hydrogels for the preparation of immunoisolated cell delivery systems.* Polysaccharides for Drug Delivery and Pharmaceutical Applications, 2006. **934**: p. 305-339.
152. Jin, S.C., et al., *Sodium alginate-assisted route to antimicrobial biopolymer film combined with aminoclay for enhanced mechanical behaviors.* Industrial Crops and Products, 2019. **135**: p. 271-282.
153. Arenales-Sierra, I.M., et al., *Calcium alginate beads loaded with Mg(OH)(2) improve L. casei viability under simulated gastric condition.* Lwt-Food Science and Technology, 2019. **112**.
154. Lin, Z., et al., *Precisely controlled delivery of magnesium ions thru sponge-like monodisperse PLGA/nano-MgO-alginate core-shell microsphere device to enable in-situ bone regeneration.* Biomaterials, 2018. **174**: p. 1-16.
155. Annabi, N., et al., *Highly Elastic and Conductive Human-Based Protein Hybrid Hydrogels.* Adv Mater, 2016. **28**(1): p. 40-9.
156. Bryant, S.J., C.R. Nuttelman, and K.S. Anseth, *Cytocompatibility of UV and visible light photoinitiating systems on cultured NIH/3T3 fibroblasts in vitro.* Journal of Biomaterials Science-Polymer Edition, 2000. **11**(5): p. 439-457.
157. Coutinho, D.F., et al., *Microfabricated photocrosslinkable polyelectrolyte-complex of chitosan and methacrylated gellan gum.* J Mater Chem, 2012. **22**(33): p. 17262-17271.
158. Meier, C. and M.E. Welland, *Wet-spinning of amyloid protein nanofibers into multifunctional high-performance biofibers.* Biomacromolecules, 2011. **12**(10): p. 3453-9.
159. Verma, D., K.S. Katti, and D.R. Katti, *Polyelectrolyte-complex nanostructured fibrous scaffolds for tissue engineering.* Materials Science and Engineering: C, 2009. **29**(7): p. 2079-2084.
160. Yamamoto, H., et al., *Preparation of polyion complex capsule and fiber of chitosan and gellan-sulfate at aqueous interface.* Bulletin of the Chemical Society of Japan, 2003. **76**(10): p. 2053-2057.

161. Narayanan, K., et al., *Three-dimensional reconstituted extracellular matrix scaffolds for tissue engineering.* Biomaterials, 2009. **30**(26): p. 4309-4317.
162. Wan, A.C., et al., *Multicomponent fibers by multi-interfacial polyelectrolyte complexation.* Adv Healthc Mater, 2012. **1**(1): p. 101-5.
163. Costa-Almeida, R., et al., *Microengineered Multicomponent Hydrogel Fibers: Combining Polyelectrolyte Complexation and Microfluidics.* Acs Biomaterials Science & Engineering, 2017. **3**(7): p. 1322-1331.
164. Leong, M.F., et al., *Patterned prevascularised tissue constructs by assembly of polyelectrolyte hydrogel fibres.* Nat Commun, 2013. **4**: p. 2353.
165. Onoe, H. and S. Takeuchi, *Cell-laden microfibers for bottom-up tissue engineering.* Drug Discovery Today, 2015. **20**(2): p. 236-246.
166. Puspoki, Z., et al., *Transforms and Operators for Directional Bioimage Analysis: A Survey.* Adv Anat Embryol Cell Biol, 2016. **219**: p. 69-93.
167. Xue, Y., et al., *Synthesis, physico-chemical characterization, and antioxidant effect of PEGylated cerium oxide nanoparticles.* Drug Deliv Transl Res, 2018. **8**(2): p. 357-367.
168. Mendes, A.C., et al., *Electrostatic self-assembly of polysaccharides into nanofibers.* Colloids and Surfaces a-Physicochemical and Engineering Aspects, 2017. **531**: p. 182-188.
169. Yamamoto, H. and Y. Senoo, *Polyion complex fiber and capsule formed by self-assembly of chitosan and gellan at solution interfaces.* Macromolecular Chemistry and Physics, 2000. **201**(1): p. 84-92.
170. Zhu, F.B., et al., *3D Printing of Ultratough Polyion Complex Hydrogels.* Acs Applied Materials & Interfaces, 2016. **8**(45): p. 31304-31310.
171. Lu, H.F., et al., *A 3D microfibrous scaffold for long-term human pluripotent stem cell self-renewal under chemically defined conditions.* Biomaterials, 2012. **33**(8): p. 2419-30.
172. Cutiongco, M.F., B.K. Teo, and E.K. Yim, *Composite Scaffolds of Interfacial Polyelectrolyte Fibers for Temporally Controlled Release of Biomolecules.* J Vis Exp, 2015(102): p. e53079.
173. Cutiongco, M.F., et al., *Composite scaffold of poly(vinyl alcohol) and interfacial polyelectrolyte complexation fibers for controlled biomolecule delivery.* Front Bioeng Biotechnol, 2015. **3**: p. 3.
174. Xue, Y., et al., *Shape-Specific Nanoceria Mitigate Oxidative Stress-Induced Calcification in Primary Human Valvular Interstitial Cell Culture.* Cell Mol Bioeng, 2017. **10**(5): p. 483-500.
175. Zou, J. and F. Kim, *Self-Assembly of Two-Dimensional Nanosheets Induced by Interfacial Polyionic Complexation.* ACS Nano, 2012. **6**(12): p. 10606-10613.
176. Razdan, S., et al., *Ionically Self-Assembled Polyelectrolyte-Based Carbon Nanotube Fibers.* Chemistry of Materials, 2009. **21**(14): p. 3062-3071.
177. Watts, C., *Off-label use of rhBMP-2.* Surgical neurology international, 2011. **2**: p. 40-40.
178. David, S.M., et al., *Lumbar spinal fusion using recombinant human bone morphogenetic protein in the canine. A comparison of three dosages and two carriers.* Spine (Phila Pa 1976), 1999. **24**(19): p. 1973-9.
179. Terrell, T.G., et al., *Pathology of recombinant human transforming growth factor-beta 1 in rats and rabbits.* Int Rev Exp Pathol, 1993. **34 Pt B**: p. 43-67.
180. Fujimoto, R., et al., *Local effects of transforming growth factor-beta1 on rat calvaria: changes depending on the dose and the injection site.* J Bone Miner Metab, 1999. **17**(1): p. 11-7.

181. Zhang, N.L., et al., *In vitro and in vivo evaluation of xenogeneic bone putty with the carrier of hydrogel derived from demineralized bone matrix.* Cell and Tissue Banking, 2018. **19**(4): p. 591-601.
182. Huber, E., et al., *Demineralized Bone Matrix as a Carrier for Bone Morphogenetic Protein-2: Burst Release Combined with Long-Term Binding and Osteoinductive Activity Evaluated In Vitro and In Vivo.* Tissue Engineering Part A, 2017. **23**(23-24): p. 1321-1330.
183. Hsu, W.K., et al., *Platelet-rich plasma in orthopaedic applications: evidence-based recommendations for treatment.* J Am Acad Orthop Surg, 2013. **21**(12): p. 739-48.
184. Urist, M.R., *Bone: formation by autoinduction.* Science, 1965. **150**(3698): p. 893-9.
185. Martin, G.J., Jr., et al., *Posterolateral intertransverse process spinal arthrodesis with rhBMP-2 in a nonhuman primate: important lessons learned regarding dose, carrier, and safety.* J Spinal Disord, 1999. **12**(3): p. 179-86.
186. Lee, J.H., et al., *The Efficacy of Porous Hydroxyapatite Granule as a Carrier of E.coli-derived Recombinant Human Bone Morphogenetic Protein-2.* Tissue Engineering and Regenerative Medicine, 2013. **10**(5): p. 279-285.
187. Abbah, S.A., et al., *Biological performance of a polycaprolactone-based scaffold used as fusion cage device in a large animal model of spinal reconstructive surgery.* Biomaterials, 2009. **30**(28): p. 5086-93.
188. Gaharwar, A.K., et al., *Bioactive Silicate Nanoplatelets for Osteogenic Differentiation of Human Mesenchymal Stem Cells.* Advanced Materials, 2013. **25**(24): p. 3329-3336.
189. Koike, T., et al., *Efficacy of Bacterial Cellulose as a Carrier of BMP-2 for Bone Regeneration in a Rabbit Frontal Sinus Model.* Materials, 2019. **12**(15).
190. Lobo, S.E. and T.L. Arinzeh, *Biphasic Calcium Phosphate Ceramics for Bone Regeneration and Tissue Engineering Applications.* Materials, 2010. **3**(2): p. 815-826.
191. Xavier, J.R., et al., *Bioactive nanoengineered hydrogels for bone tissue engineering: a growth-factor-free approach.* ACS Nano, 2015. **9**(3): p. 3109-18.
192. Nudelman, F., et al., *The role of collagen in bone apatite formation in the presence of hydroxyapatite nucleation inhibitors.* Nat Mater, 2010. **9**(12): p. 1004-9.
193. Viebke, C., J. Borgstrom, and L. Piculell, *Characterization of Kappa-Carrageenan and Iota-Carrageenan Coils and Helices by Malls/Gpc.* Carbohydrate Polymers, 1995. **27**(2): p. 145-154.
194. Yang, B., et al., *Exposure to common food additive carrageenan leads to reduced sulfatase activity and increase in sulfated glycosaminoglycans in human epithelial cells.* Biochimie, 2012. **94**(6): p. 1309-16.
195. Xue, Y.F., et al., *Semiquantitative FTIR Analysis of the Crosslinking Density of Poly(ester amide)-Based Thermoset Elastomers.* Macromolecular Materials and Engineering, 2016. **301**(3): p. 296-305.
196. Vo, T.N., et al., *In vitro and in vivo evaluation of self-mineralization and biocompatibility of injectable, dual-gelling hydrogels for bone tissue engineering.* Journal of Controlled Release, 2015. **205**: p. 25-34.
197. Kokubo, T. and H. Takadama, *How useful is SBF in predicting in vivo bone bioactivity?* Biomaterials, 2006. **27**(15): p. 2907-15.

198. Tanahashi, M. and T. Matsuda, *Surface functional group dependence on apatite formation on self-assembled monolayers in a simulated body fluid.* Journal of Biomedical Materials Research, 1997. **34**(3): p. 305-315.
199. Koutsopoulos, S., *Synthesis and characterization of hydroxyapatite crystals: a review study on the analytical methods.* J Biomed Mater Res, 2002. **62**(4): p. 600-12.
200. Zhang, X., et al., *Biomimetic remineralization of demineralized enamel with nano-complexes of phosphorylated chitosan and amorphous calcium phosphate.* J Mater Sci Mater Med, 2014.
201. Pishbin, F., et al., *Electrophoretic deposition of gentamicin-loaded bioactive glass/chitosan composite coatings for orthopaedic implants.* ACS Appl Mater Interfaces, 2014. **6**(11): p. 8796-806.
202. Lala, S., et al., *Biocompatible nanocrystalline natural bonelike carbonated hydroxyapatite synthesized by mechanical alloying in a record minimum time.* Mater Sci Eng C Mater Biol Appl, 2014. **42**: p. 647-56.
203. Boskey, A.L., *Mineral analysis provides insights into the mechanism of biomineralization.* Calcif Tissue Int, 2003. **72**(5): p. 533-6.
204. Chen, L., et al., *Refinement of collagen-mineral interaction: A possible role for osteocalcin in apatite crystal nucleation, growth and development.* Bone, 2014.
205. Yamada, N., et al., *Effect of Gelatin beta-tricalcium Phosphate Sponge with Platelet-rich Plasma on Bone Regeneration in Massive Ulna Defects.* Journal of Medical and Biological Engineering, 2013. **33**(6): p. 545-551.
206. Takada, T., et al., *Sulfated polysaccharides enhance the biological activities of bone morphogenetic proteins.* Journal of Biological Chemistry, 2003. **278**(44): p. 43229-43235.
207. Zhou, H.J., et al., *Enhanced bioactivity of bone morphogenetic protein-2 with low dose of 2-N, 6-O-sulfated chitosan in vitro and in vivo.* Biomaterials, 2009. **30**(9): p. 1715-1724.
208. Rai, B., et al., *Repair of segmental ulna defects using a beta-TCP implant in combination with a heparan sulfate glycosaminoglycan variant.* Acta Biomaterialia, 2015. **28**: p. 193-204.
209. Baeza, R.I., et al., *kappa-carrageenan - Protein interactions: Effect of proteins on polysaccharide gelling and textural properties.* Lebensmittel-Wissenschaft Und-Technologie-Food Science and Technology, 2002. **35**(8): p. 741-747.
210. Sun, C.Y., et al., *Sulfated polysaccharides interact with fibroblast growth factors and protect from denaturation.* Febs Open Bio, 2019. **9**(8): p. 1477-1487.
211. Jeong, J., et al., *Bioactive calcium phosphate materials and applications in bone regeneration.* Biomater Res, 2019. **23**: p. 4.
212. Ogata, K., et al., *Comparison of osteoblast responses to hydroxyapatite and hydroxyapatite/soluble calcium phosphate composites.* J Biomed Mater Res A, 2005. **72**(2): p. 127-35.
213. Ramay, H.R. and M. Zhang, *Biphasic calcium phosphate nanocomposite porous scaffolds for load-bearing bone tissue engineering.* Biomaterials, 2004. **25**(21): p. 5171-80.
214. Shao, N., et al., *Development of Organic/Inorganic Compatible and Sustainably Bioactive Composites for Effective Bone Regeneration.* Biomacromolecules, 2018. **19**(9): p. 3637-3648.

215. dos Santos, E.A., et al., *Surface energy of hydroxyapatite and beta-tricalcium phosphate ceramics driving serum protein adsorption and osteoblast adhesion.* J Mater Sci Mater Med, 2008. **19**(6): p. 2307-16.
216. Tsapikouni, T.S., S. Allen, and Y.F. Missirlis, *Measurement of interaction forces between fibrinogen coated probes and mica surface with the atomic force microscope: The pH and ionic strength effect.* Biointerphases, 2008. **3**(1): p. 1-8.
217. Liu, F., et al., *Osteogenesis of 3D printed macro-pore size biphasic calcium phosphate scaffold in rabbit calvaria.* J Biomater Appl, 2019. **33**(9): p. 1168-1177.
218. Amirian, J., et al., *Bone formation of a porous Gelatin-Pectin-biphasic calcium phosphate composite in presence of BMP-2 and VEGF.* Int J Biol Macromol, 2015. **76**: p. 10-24.
219. Riddle, R.C., et al., *MAP kinase and calcium signaling mediate fluid flow-induced human mesenchymal stem cell proliferation.* Am J Physiol Cell Physiol, 2006. **290**(3): p. C776-84.
220. Foreman, M.A., et al., *Group III metabotropic glutamate receptor activation inhibits Ca2+ influx and nitric oxide synthase activity in bone marrow stromal cells.* J Cell Physiol, 2005. **204**(2): p. 704-13.
221. Tada, H., et al., *Phosphate increases bone morphogenetic protein-2 expression through cAMP-dependent protein kinase and ERK1/2 pathways in human dental pulp cells.* Bone, 2011. **48**(6): p. 1409-16.
222. Julien, M., et al., *Phosphate-dependent regulation of MGP in osteoblasts: role of ERK1/2 and Fra-1.* J Bone Miner Res, 2009. **24**(11): p. 1856-68.
223. Khoshniat, S., et al., *The emergence of phosphate as a specific signaling molecule in bone and other cell types in mammals.* Cell Mol Life Sci, 2011. **68**(2): p. 205-18.
224. Xia, H., et al., *Lyophilized Scaffolds Fabricated from 3D-Printed Photocurable Natural Hydrogel for Cartilage Regeneration.* ACS Appl Mater Interfaces, 2018. **10**(37): p. 31704-31715.
225. Montufar-Solis, D., et al., *Using cartilage to repair bone: an alternative approach in tissue engineering.* Ann Biomed Eng, 2004. **32**(3): p. 504-9.
226. Dennis, S.C., et al., *Endochondral ossification for enhancing bone regeneration: converging native extracellular matrix biomaterials and developmental engineering in vivo.* Tissue Eng Part B Rev, 2015. **21**(3): p. 247-66.
227. Bullough, P.G., *Orthopaedic pathology*, in *Expert consult Online and print*. 2009, Mosby/Elsevier,: Philadelphia, PA. p. 1 online resource.
228. Phadke, A., Y.R. Shih, and S. Varghese, *Mineralized synthetic matrices as an instructive microenvironment for osteogenic differentiation of human mesenchymal stem cells.* Macromol Biosci, 2012. **12**(8): p. 1022-32.
229. de Grado, G.F., et al., *Bone substitutes: a review of their characteristics, clinical use, and perspectives for large bone defects management.* Journal of Tissue Engineering, 2018. **9**: p. 1-18.
230. Kinaci, A., V. Neuhaus, and D.C. Ring, *Trends in Bone Graft Use in the United States.* Orthopedics, 2014. **37**(9).
231. Kowalczewski, C.J. and J.M. Saul, *Biomaterials for the Delivery of Growth Factors and Other Therapeutic Agents in Tissue Engineering Approaches to Bone Regeneration.* Front Pharmacol, 2018. **9**: p. 513.

232. Tannoury, C.A. and H.S. An, *Complications with the use of bone morphogenetic protein 2 (BMP-2) in spine surgery.* Spine J, 2014. **14**(3): p. 552-9.
233. Lee, S.S., et al., *Bone regeneration with low dose BMP-2 amplified by biomimetic supramolecular nanofibers within collagen scaffolds.* Biomaterials, 2013. **34**(2): p. 452-459.
234. James, A.W., et al., *A Review of the Clinical Side Effects of Bone Morphogenetic Protein-2.* Tissue Eng Part B Rev, 2016. **22**(4): p. 284-97.
235. Koempel, J.A., et al., *The effect of recombinant human bone morphogenetic protein-2 on the integration of porous hydroxyapatite implants with bone.* J Biomed Mater Res, 1998. **41**(3): p. 359-63.
236. Sant, S., et al., *Biomimetic gradient hydrogels for tissue engineering.* Can J Chem Eng, 2010. **88**(6): p. 899-911.
237. Cai, S.S., et al., *Injectable glycosaminoglycan hydrogels for controlled release of human basic fibroblast growth factor.* Biomaterials, 2005. **26**(30): p. 6054-6067.
238. Hokugo, A., et al., *Stimulation of bone regeneration following the controlled release of water-insoluble oxysterol from biodegradable hydrogel.* Biomaterials, 2014. **35**(21): p. 5565-71.
239. Segovia, N., et al., *Hydrogel Doped with Nanoparticles for Local Sustained Release of siRNA in Breast Cancer.* Adv Healthc Mater, 2015. **4**(2): p. 271-80.
240. Hwang, C.M., et al., *Fabrication of three-dimensional porous cell-laden hydrogel for tissue engineering.* Biofabrication, 2010. **2**(3): p. 035003.
241. Pina, S., J.M. Oliveira, and R.L. Reis, *Natural-Based Nanocomposites for Bone Tissue Engineering and Regenerative Medicine: A Review.* Advanced Materials, 2015. **27**(7): p. 1143-1169.
242. Coutinho, D.F., et al., *Microfabricated photocrosslinkable polyelectrolyte-complex of chitosan and methacrylated gellan gum.* Journal of Materials Chemistry, 2012. **22**(33): p. 17262.
243. Abbah, S.A., et al., *In vivo bioactivity of rhBMP-2 delivered with novel polyelectrolyte complexation shells assembled on an alginate microbead core template.* Journal of Controlled Release, 2012. **162**(2): p. 364-372.
244. Fernandes, G., et al., *Combination of Controlled Release Platelet-Rich Plasma Alginate Beads and Bone Morphogenetic Protein-2 Genetically Modified Mesenchymal Stem Cells for Bone Regeneration.* Journal of Periodontology, 2016. **87**(4): p. 470-480.
245. Silva, J.M., et al., *Chitosan - Alginate Multilayered Films with gradients of physicochemical cues.* Journal of Materials Chemistry B, 2015.
246. Administration, U.S.F.a.D., *US FDA approval.* 2015.
247. Visser, J., et al., *Reinforcement of hydrogels using three-dimensionally printed microfibres.* Nature Communications, 2015. **6**: p. 10.
248. Lee, H.J., et al., *Incorporation of chitosan-alginate complex into injectable calcium phosphate cement system as a bone graft material.* Materials Science & Engineering C-Materials for Biological Applications, 2019. **94**: p. 385-392.
249. Sant, S., *Biomimetic Hydrogel Scaffolds and Related Methods*, U.P. App, Editor. 2016: US.

250. Rhee, S.-H., J.D. Lee, and J. Tanaka, *Nucleation of Hydroxyapatite Crystal through Chemical Interaction with Collagen.* Journal of the American Ceramic Society, 2000. **83**(11): p. 2890-2892.
251. Hintze, V., et al., *Artificial extracellular matrices of collagen and sulphated hyaluronan enhance the differentiation of human mesenchymal stem cells in the presence of dexamethasone.* J Tissue Eng Regen Med, 2014. **8**(4): p. 314-24.
252. Silva, T.H., et al., *Marine algae sulfated polysaccharides for tissue engineering and drug delivery approaches.* Biomatter, 2012. **2**(4): p. 278-89.
253. Nerdal, W., et al., *Evidence for Double-Helical Kappa-Carrageenan in Aqueous Lii-Solution and Model for Iodide Binding.* Journal of Biomolecular Structure & Dynamics, 1993. **10**(5): p. 785-&.
254. Kokubo, T. and H. Takadama, *How useful is SBF in predicting in vivo bone bioactivity?* Biomaterials, 2006. **27**(15): p. 2907-2915.
255. Zaky, S.H., et al., *Poly (glycerol sebacate) elastomer supports bone regeneration by its mechanical properties being closer to osteoid tissue rather than to mature bone.* Acta Biomaterialia, 2017. **54**: p. 95-106.
256. Chaya, A., et al., *In vivo study of magnesium plate and screw degradation and bone fracture healing.* Acta Biomaterialia, 2015. **18**: p. 262-269.
257. Zaky, S.H., et al., *Poly(glycerol sebacate) elastomer: a novel material for mechanically loaded bone regeneration.* Tissue Eng Part A, 2014. **20**(1-2): p. 45-53.
258. Seeherman, H., et al., *rhBMP-2/calcium phosphate matrix accelerates osteotomy-site healing in a nonhuman primate model at multiple treatment times and concentrations.* Journal of Bone and Joint Surgery-American Volume, 2006. **88a**(1): p. 144-160.
259. Li, L., et al., *Recent advances of biomaterials in biotherapy.* Regen Biomater, 2016. **3**(2): p. 99-105.
260. Damiati, L., et al., *Impact of surface topography and coating on osteogenesis and bacterial attachment on titanium implants.* Journal of Tissue Engineering, 2018. **9**: p. 16.
261. Sant, S., et al., *Hybrid PGS–PCL microfibrous scaffolds with improved mechanical and biological properties.* Journal of tissue engineering and regenerative medicine, 2011. **5**(4): p. 283-291.
262. Sant, S., et al., *Effect of biodegradation and de novo matrix synthesis on the mechanical properties of valvular interstitial cell-seeded polyglycerol sebacate–polycaprolactone scaffolds.* Acta Biomaterialia, 2013. **9**(4): p. 5963-5973.
263. Bodde, E.W., et al., *Closing capacity of segmental radius defects in rabbits.* J Biomed Mater Res A, 2008. **85**(1): p. 206-17.
264. Yu, W., et al., *Use of a three-dimensional printed polylactide-coglycolide/tricalcium phosphate composite scaffold incorporating magnesium powder to enhance bone defect repair in rabbits.* Journal of Orthopaedic Translation, 2019. **16**: p. 62-70.
265. Whited, B.M., et al., *Osteoblast response to zirconia-hybridized pyrophosphate-stabilized amorphous calcium phosphate.* J Biomed Mater Res A, 2006. **76**(3): p. 596-604.
266. Cao, L., et al., *Bone regeneration using photocrosslinked hydrogel incorporating rhBMP-2 loaded 2-N, 6-O-sulfated chitosan nanoparticles.* Biomaterials, 2014. **35**(9): p. 2730-2742.
267. Albrektsson, T. and C. Johansson, *Osteoinduction, osteoconduction and osseointegration.* Eur Spine J, 2001. **10 Suppl 2**: p. S96-101.

268. Wang, W. and K.W.K. Yeung, *Bone grafts and biomaterials substitutes for bone defect repair: A review.* Bioact Mater, 2017. **2**(4): p. 224-247.
269. Zaky, S.H., et al., *Poly (glycerol sebacate) elastomer supports bone regeneration by its mechanical properties being closer to osteoid tissue rather than to mature bone.* Acta Biomater, 2017. **54**: p. 95-106.